UNIVERSITY OF CAPE TOWN

DEPARTMENT OF CHEMICAL ENGINEERING

HYSA CATALYSIS CENTRE OF COMPETENCE, CATALYSIS INSTITUTE

IN COLLABORATION WITH HYPLAT (PTY) LTD

IMPROVING ON QUALITY CONTROL METHODS USED IN COMMERCIAL MEA MANUFACTURING

SUBMITTED FOR MASTER OF SCIENCE IN ENGINEERING IN CHEMICAL ENGINEERING DEGREE

(MScEng CHEM ENG)

AUTHOR: RAEESAH GANI

SUPERVISORS: DR. PIETER LEVECQUE AND DR. DARIJA SUSAC

CO-SUPERVISOR: FRANCOIS VAN SCHALKWYK

FEBRUARY 2023

"If we knew what it was we were doing,
it would not be called research,
would it?"

- **Albert Einstein**

Dedicated to my late parents, Rashaad & Tasneem, who taught me to always pursue my passions and that there is no time like the present to do so – I hope this achievement will fulfil the dream they envisioned for me.

Dedicated to my husband, Mohamed, for his endless love, support and encouragement throughout my pursuits.

PLAGIARISM DECLARATION

I know the meaning of plagiarism and declare that all the work in the document, save for that which is properly acknowledged, is my own. This thesis/dissertation has been submitted to the Turnitin module (or equivalent similarity and originality checking software) and I confirm that my supervisors have seen my report and any concerns revealed by such have been resolved with my supervisors.

Name: Raeesah Gani

Date: 11/02/2023

Signature: Signed by candidate

ABSTRACT

With the current rate of global warming, temperatures are continuously increasing and could have severe impacts on natural and human systems. The transport sector has the largest potential for short term reduction of emissions and the fuel cell industry could be a viable replacement for fossil fuel consumption. The hydrogen economy, alongside the fuel cell industry, can target decarbonisation of long-haul and heavy-duty transport by pursuing a green hydrogen mobility ecosystem. One of the key barriers hindering fuel cell commercialisation is the lack of standard methods for quality control in membrane electrode assembly (MEA) manufacturing, specifically the lack of in-line, non-destructive and roll-to-roll quality control methods. There are currently 5 typical methods for assessing the quality of an MEA, which are gravimetric and thickness analysis, visual and optical microscopy inspection and single cell characterisation. The development of efficient, contactless and non-destructive techniques for in-line quality control testing is a critical enabler in alleviating manufacturing costs by detecting and flagging manufacturing defects thus ensuring a desired quality standard is met at each step in the process. Nonconforming products are detected early and removed at different stages in the process, reducing manufacturing costs that would have otherwise been wasted on defective products. (Yuan, et al., 2021; Phillips, Ulsh , Neyerlin, Porter, & Bender, 2018)

In this work, three techniques have been proposed and developed for improving quality control. They are automated visual inspection, infrared thermography (IRT) and x-ray fluorescence (XRF). A rig was successfully designed and built for the automated visual inspection and IRT and methods were successfully developed for the use of the 3 techniques in MEA fabrication.

The results from the thickness and gravimetric analysis yielded values that were on par with the experimental targets and commercial standards. A linear relationship was also demonstrated, showing the link between thickness and gravimetric loading. If the relative humidity is well controlled, one of the two quality control methods could be omitted during manufacturing to decrease manufacturing time. To overcome the downfall associated with relative humidity for both these test methods, a newer technology, XRF spectrometry, was investigated which determines the PGM loading and is independent of changes in the relative humidity. The PGM loading can then be used to calculate the approximate thickness of the electrode layers if needed and is less labour intensive and time consuming. It was discovered that the XRF needs to be specifically programmed for each matrix that it is to be used on – where the matrix includes the substrate thickness, type of substrate, type of catalyst in the ink, ionomer content and sample orientation (cathode or anode facing XRF eye). It is assumed that the matrix expands to other parameter changes as well, such as type of ionomer, ink solids content and presence of backers or covers film. However, these parameters were not tested within this study due to time and resource constraints.

To assess the aesthetic and physical quality of the CLs produced, visual and optical microscopy inspection were done. Visual inspection involves human observation of the layer under light, therefore, methods were developed in this study to improve the test procedure and omit human error by digitising the test procedure. The results yielded from the visual and optical microscopy inspection were compared and were found to be almost identical. For the purpose of commercial manufacturing to identify light translucency above 10%, it would be less labour intensive and time consuming to use the automated visual inspection method developed. The downfall of either method arises when coating the anode layer (in this study) or when coating the second electrode (in general) due to the

masking effect of first layer on the second, which prevents inconsistencies in the second layer being identified. The other downfall of either method is the inability to determine if a defect is a light spot or if it is a pinhole through the MEA. This is where IRT comes in as it was successful in identify pinholes.

SEM and single cell performance characterisation were used to test whether the methods developed for automated visual inspection, XRF analysis and/or IR thermography had a negative or destructive effect on the MEAs – the results proved that there was no negative effect from any of the 3 methods.

All three techniques were successfully developed for local use in laboratory and small-medium scale manufacturing. The automated visual inspection technique proved to be a key quality control technique and further work into its next generation and incorporation into a high-volume manufacturing line is needed as this could not be investigated due to time and budget constraints. The study was successful in developing a method for the use of XRF to determine PGM loadings and in investigating key parameters associated with its calibration procedures. The value of XRF over gravimetric analysis was shown and the XRF was successfully incorporated into a simulated high-volume line, however, further work is needed for its next generation in a high-volume line. A method for the use of IRT for defect detection was also successfully developed and an attempt to create a defect catalogue was started, however, cataloguing the appearance of defects in IRT still requires more work.

ACKNOWLEDGEMENTS

I would like to express my gratitude to the HySA catalysis department for the opportunity and funding to undertake my masters.

I would like to thank my supervisor, Pieter Levecque, for encouraging me and easing my concerns of working and undertaking my masters part time. I would like to thank my supervisor, Darija Susac, for stepping in as a second supervisor to guide and assist me in my second year of my MSc and for assisting me with all my needs in the lab and my experimental work. I would like to thank my co-supervisor, Francois Van Schalkwyk, for allowing me to pursue my masters part time and for the guidance and assistance throughout it. I would like to thank my colleagues, Ursula Nyambi, Jessica Chamier and Omishka Ranganthan for their support, contributions and insight during my experiments. I would like to thank the UCT' electron microscopy unit, specifically Miranda Waldron, for her assistance with analysing scanning electron microscopy samples. I would like to thank HyPlat for their contributions with regards to commercial manufacturing.

I would like to express my gratitude and thank my husband for his continued support and encouragement, as well as for the sacrifices he made to accommodate my studies, without him my MSc would not have been possible.

To my family, friends and those who have become family along the way, I am grateful for your faith in me and liberating me to achieve my dreams. Thank you for the sacrifices you made that allowed me to be where I am today. To my grandmother and aunt, none of my accomplishments would have been possible without the sacrifice you made to bring me up, encourage me, push me, teach me and help me grow into the person I am today – I will forever be indebted for the struggles and sacrifices you made to play the role of a mother and a father to 3 little kids who were left on your doorstep after we lost our parents.

I would like to thank The God, Almighty for everything that has been granted to me in life.

CONFERENCE CONTRIBUTIONS

2022

R. Gani, P. Levecque and D. Susac

"Improving on Quality Control Methods Used in MEA Manufacturing"

Poster presentation at the 32nd Annual Meeting of the Catalysis Society of South Africa, Drakensburg, South Africa.

TABLE OF CONTENTS

LIST OF FIGURES

LIST OF TABLES

LIST OF ABBREVIATIONS AND NOMENCLATURE

°C	Degrees Celsius
AFC	Alkaline Fuel Cell
APU	Auxiliary Power Unit
BoL	Beginning Of Life
C	Carbon
CCM	Catalyst Coated Membrane
CCS	Catalyst Coated Substrate
CHP	Combined Heat and Power
CL	Catalyst Layer
CO	Carbon Monoxide
CO_2	Carbon Dioxide
DMFC	Direct Methanol Fuel Cell
DOE	Design Of Experiments
DP	Dew Point
DSLR	Digital Signal Lens Reflex
ECD	Low-Voltage High-Contrast Detector
ECSA	Electrochemically Active Surface Area
g	Gram(S)
GDE	Gas Diffusion Electrode
GDL	Gas Diffusion Layer
H	Hydrogen
H_2O	Water
HFR	High Frequency Resistance

HOR	Hydrogen Oxidation Reaction
HySA	Hydrogen South Africa
I	Current
IRT	Infrared Thermography
MCFC	Molten Carbonate Fuel Cell
mg	Milligram(S)
mm	Millimetre
mol	Mole(S)
MPL	Microporous Layer
N	Molar Flow of Hydrogen
NASA	National Aeronautics and Space Administration
nm	Nanometre
O	Oxygen
OCV	Open Circuit Voltage
ORR	Oxygen Reduction Reaction
PAFC	Phosphoric Acid Fuel Cell
PEM	Polymer Electrolyte Membrane / Proton Exchange Membrane
PEMFC	Polymer Electrolyte Membrane Fuel Cell
PET	Polyethylene Terephthalate
PPM	Parts Per Million
Pt	Platinum
PTFE	Polytetrafluoroethylene
RH	Relative Humidity
SEM	Scanning Electron Microscopy
SOFC	Solid Oxide Fuel Cell
T	Temperature

TEM	Transmission Electron Microscopy
TOCs	Test Operating Conditions
USI	Ultrasonic Systems Inc
V	Volt(S), Voltage
VCD	Everhart Thornley Detector
XRD	X-Ray Diffraction
XRF	X-Ray Fluorescence
z	Real Impedance
z'	Imaginary Impedance
λ	Stoichiometric Ratios
ρ	Absolute Pressures

CHAPTER I: INTRODUCTION

The purpose of this thesis is to explore improvements in the quality control techniques used in commercial MEA manufacturing. This chapter provides an overview and outline of the work done in this study.

1.1. Overview

Nature has maintained balance in the carbon cycle for millions of years, however, this cycle has been offset with the rapid evolution of technology driving fossil fuel consumption and resulting in a high carbonaceous emission. This offset has increased the rate of global warming. Although, carbon capture technology and other measures exist to address the rate of global warming, these have either been challenged with commercial and political barriers or have not been deployed at large enough scales (Peter, 2018). At the current rate of global warming, temperatures are continuously increasing and could have severe impacts on natural and human systems in the near future.

The transport sector was accountable for around 16.2% of Carbon Dioxide (CO_2) emissions in 2016 (as depicted in Figure 1) (Ritchie, 2020). However, this sector has the largest potential for short term reduction of emissions. The fuel cell industry could be a viable replacement for fossil fuel consumption in the transport sector. Proton Exchange Membrane Fuel Cells (PEMFCs) are the most promising but their commercial viability is negatively affected by the high manufacturing costs, durability and the lack of fuel delivery infrastructure. For PEMFCs to be a viable replacement, technological and commercial manufacturing improvements are required. These improvements should be focused on Membrane Electrode Assembly (MEA) manufacturing, as MEAs are the vital component of PEMFCs. Manufacturing processes need to be improved to enable higher production volumes, increased reliability and lower costs (Ulsh, n.d.).

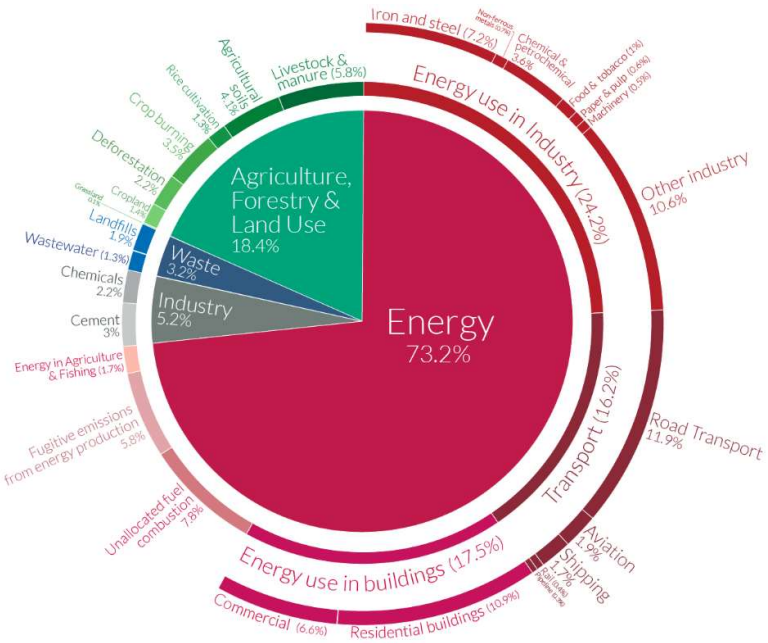

Figure 1: Global CO_2 emissions in transport 2016 (Ritchie, 2020)

In this study, defect development and detection during manufacturing will be targeted by means of improved quality control. The work done focuses on improvements for the quality control techniques used in MEA manufacturing and on developing and documenting methodology for how to conduct these quality control techniques.

1.2. Thesis Outline

The chapters of this thesis are organised as follows:

- Chapter 2: Literature Review
  This chapter provides relevant background information on the main research topics covered in this thesis. The chapter focuses on the hydrogen (H_2) economy, the fuel cell industry and PEMFCs, the structure and fabrication of MEAs, defects associated with manufacturing of MEAs and quality control techniques for manufacturing.
- Chapter 3: Research Approach
  The scope, objectives and limitations are presented in this chapter to guide the overall approach taken in the thesis based on the literature review in the Chapter 2.
- Chapter 4: Experimental
  This chapter details the materials used and experimental methods which were undertaken to fabricate the MEAs, set up the quality control methods, develop the methods for some of the quality control techniques and analyse the MEAs produced.
- Chapter 5: Method Development
  This chapter covers the method development that was done for several quality control methods.
- Chapter 6: Results and Discussion
  This chapter tabulates and depicts the results obtained for a batch of test MEAs that were run through the various quality control analysis to investigate each technique. The chapter ends with a summary discussing the relation between each quality control method analysed, how they relate to or impact one another and which techniques would have the best outcome for application in commercial manufacturing of MEAs. The MEA sample sets referred to in this chapter were described in detail in Table 6 Section 4.1.3. Some of data for the work done in this section can be found in APPENDIX A: Thickness Analysis, APPENDIX B: Gravimetric Analysis, Inspection, APPENDIX, APPENDIX G: Single Cell Performance Testing and APPENDIX H: SEM. All other data can be seen upon request.
- Chapter 7: Conclusion and Future Work
  This chapter includes a summary of the main conclusions of this study and contributions to research for PEMFC literature The chapter further discusses the possible directions for future research associated with the work done in this thesis.

CHAPTER II: LITERATURE REVIEW

This chapter provides relevant background information on the main research topics covered in this thesis. The chapter focuses on the hydrogen (H_2) economy, the fuel cell industry and PEMFCs, the structure and fabrication of MEAs, defects associated with manufacturing of MEAs and quality control techniques for manufacturing.

2.1. The Hydrogen Economy

H_2 is a versatile feedstock used in several industrial processes, such as; in the production of ammonia, polymer and resin, in refining for hydrocracking and hydrotreating and in iron and steel production (Nicita, Maggio, Andaloro, & Squadrito, 2020). The future envisioned for the hydrogen economy is one where H_2 is used as a fuel for heat and transport. H_2 can be used as a final energy carrier or converted into methane (CH_4), synthesis gas, liquid fuels, electricity or chemicals. 96% of global H_2 production is made up of reforming, gasification and processing of natural gas, coal and oil and the balance of the 4% is made up of water electrolysis (Nicita, Maggio, Andaloro, & Squadrito, 2020). To phase out the use of fossil fuels and limit global warming, H_2 can be created and used as a fuel, as the combustion of H_2 releases only water vapor as a by-product. In addition, the conversion of H_2 into other energy carriers or products such as CH_4 or chemicals requires CO_2 as a feedstock thus further limiting global warming and its effects by consuming the CO_2 produced in H_2 manufacturing. (Kalamaras & Efstathiou, 2013; Wulf, Zapp, & Schreiber, 2020)

In South Africa, Sasol is pursuing the development of a green H_2 mobility ecosystem in collaboration with Toyota, who is currently a leading supplier in zero-emission H_2 fuel cell vehicles . The collaboration will target heavy-duty long-haul trucks in South Africa mainly (SASOL, 2021). The hydrogen economy, alongside the fuel cell industry, can target decarbonisation of long-haul and heavy-duty transport by pursuing a green H_2 mobility ecosystem. Furthermore, green H_2 can decarbonise the mining, chemicals, iron and steel sectors. Thus, the demand for H_2 has tripled since 1975 and is continuously increasing (Birol, 2019). The hydrogen economy and its upscaling does however face certain limitations, which include; poor long-term storage solutions, safety concerns associated with its high reactivity and the expense of producing H_2 via electrolysis. However, development of the hydrogen economy has been accelerated by recent advancements in the fields of electrolyses for H_2 production, H_2 liquefaction, compression and carriers for storage and H_2 fuel cells for power generation. (Kalamaras & Efstathiou, 2013; SASOL, 2021)

2.2. The Fuel Cell Industry and PEMFC

Fuel cells are electrochemical cells are electrochemical devices that produce electricity, water and heat using hydrogen and oxygen as fuels. They are a key element for building a competitive, secure and sustainable clean energy economy and they offer a broad range of benefits such as; reduced greenhouse gas emissions, reduced oil consumption, increased use of renewable power, high efficiency energy conversion, fuel flexibility and reduced air pollution (U.S. Department of Energy , 2011). Fuel cells were developed within the timeline depicted in Figure 2 below.

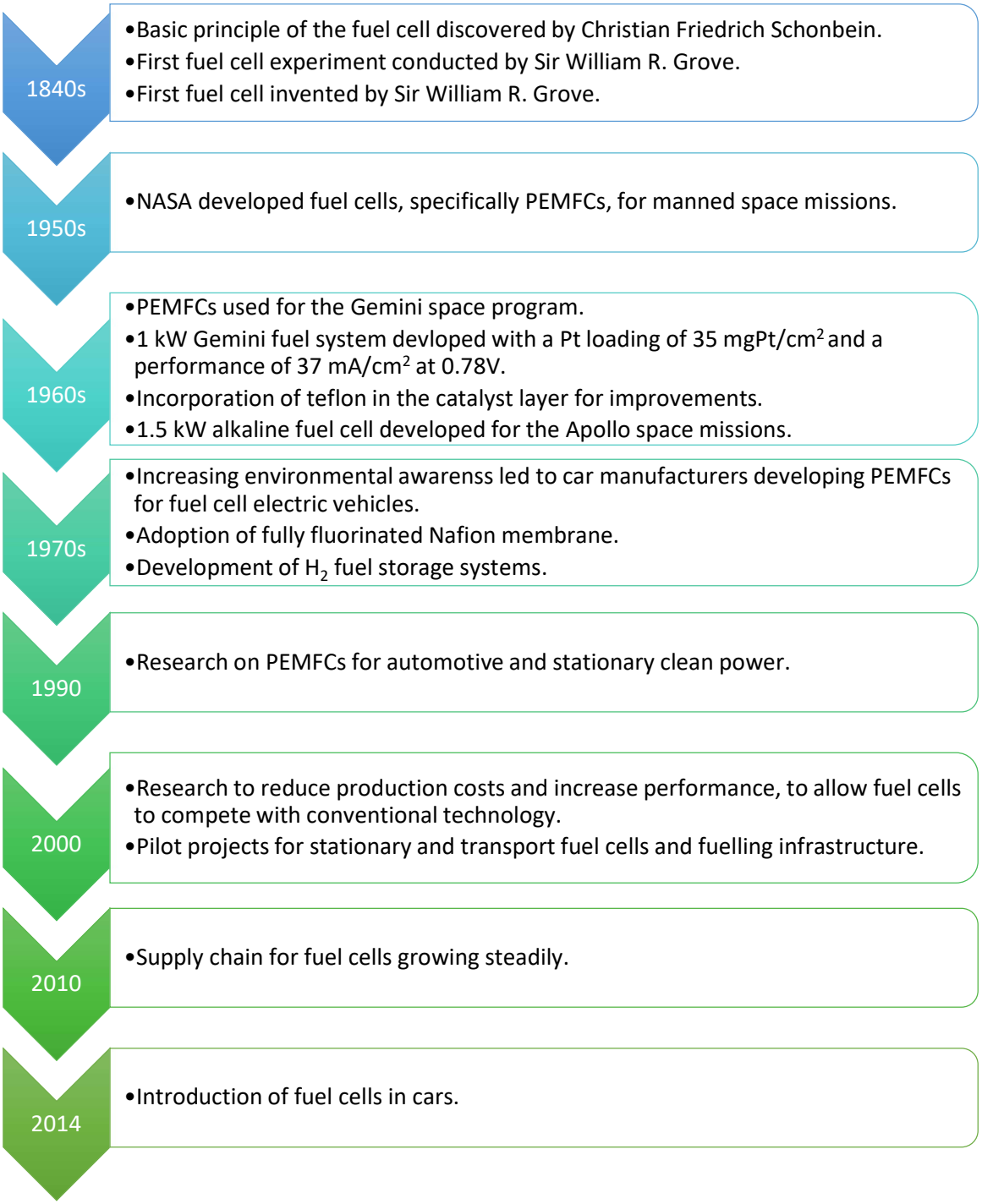

Figure 2: Timeline of the history of fuel cells (Laabidi, 2015; Wang , Chen, Mishler, Cho, & Adroher, 2011)

There are several types of fuel cells which have different applications, as depicted in Figure 3.

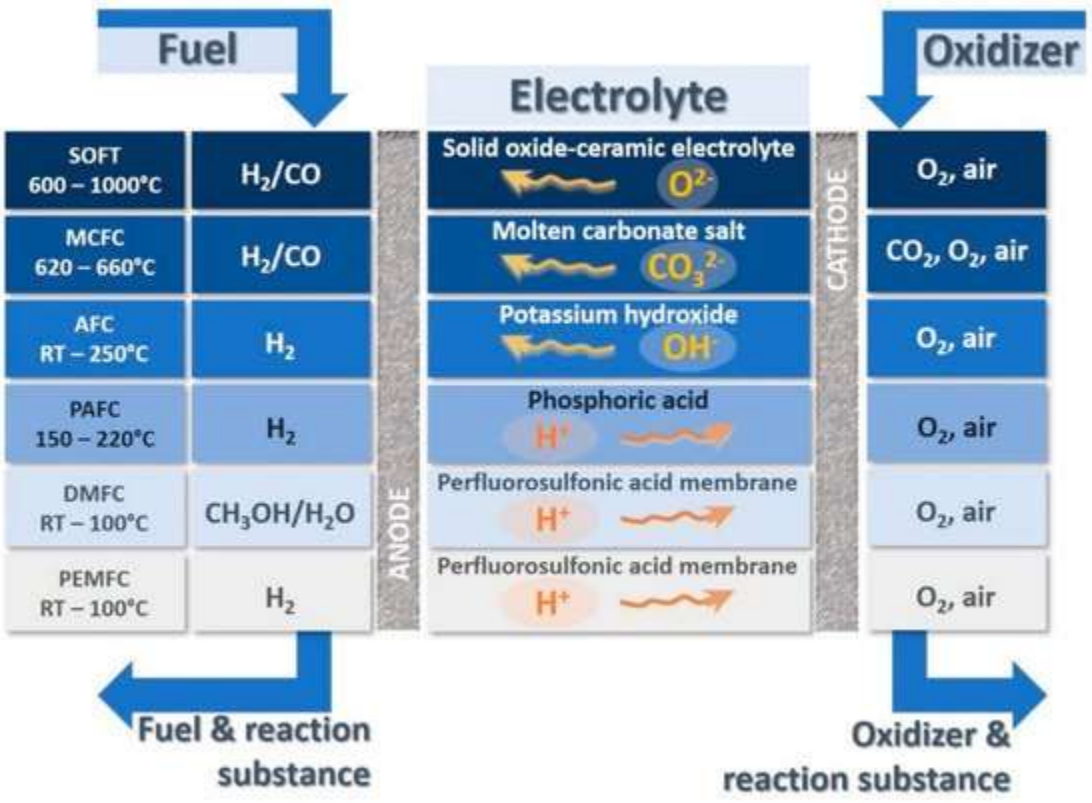

Figure 3: Summary of various types of fuel cells (Ebrahimi, Kujawski, Fatyeyeva, & Kujawa, 2021; U.S Department of Energy, 2016)

PEMFCs and Direct Methanol Fuel Cells (DMFCs) are used for backup and portable power, distributed power generation and speciality vehicle applications. Their advantages include; usage of a solid electrolyte, low temperature operation, quick start-up, high fuel efficiency and low to zero emissions for PEMFCs specifically. However, they have the disadvantage of having expensive catalysts and being sensitive to fuel impurities. Alkaline Fuel Cells (AFCs) are used for military and space applications and have the advantage of faster cathode reactions, high performance and low-cost components but are sensitive to CO_2 in the fuel and require electrolyte management. Phosphoric Acid Fuel Cells (PAFCs) are used in distributed power generation applications and have the advantage of combined heat and power (CHP) capabilities and increased tolerance to fuel impurities but are prone to high temperature corrosion, long start-ups and low power density. Molten Carbonate Fuel Cells (MCFCs) are used for electric utility and distributed power generation applications and have the advantage of high efficiencies, fuel flexibility, catalyst flexibility and CHP capabilities. However, they are also prone to high temperature corrosion, have long start-ups and have low power density. Solid Oxide Fuel Cells (SOFCs) are used for auxiliary power, electric utility and distributed power generation applications. They have the advantage of high efficiencies, fuel flexibility, catalyst flexibility, solid electrolytes, CHP capabilities and hybrid cycles. However, their drawbacks include high temperature corrosion, requirements for higher temperature operation and long start-ups.

PEMFCs have gained the most momentum recently and are being widely used and developed. This is because they have a high efficiency, fast start up, an ability to perform at low temperatures, an ability to be transportable, a long lifespan of 5000h and a high-power density of 0.3-0.8 W/cm^2 (Baricci, et al., 2019). A high efficiency DC electrical power is generated via an electrochemical conversion of high purity H_2 and atmospheric oxygen, whilst releasing no direct emission of pollutants. Therefore, peaking

the interest of the automotive industry in commercialising fuel cell electric vehicles. However, the cost of the fuel stacks needed for fuel cell electric vehicles is a major setback. Recently, a commercially viable target has been set to achieve 40$ per kWnet for mass production (more than 500 000 vehicles/year) by the year 2025. (Baricci, et al., 2019)

2.3. Membrane Electrode Assemblies

2.3.1. Structure and Electrochemical Reactions

PEMFCs are made from several layers (as depicted in Figure 4). The heart of a PEMFC is the MEA, which is made up of a membrane, catalyst layers (CL), gaskets and gas diffusion layers (GDLs). An MEA is manufactured as a 2-, 3-, 5- or 7-layer part and consists of the subcomponents listed in Table 1 below. Bipolar plates are then used to assemble individual PEMFCs into a fuel cell stack.

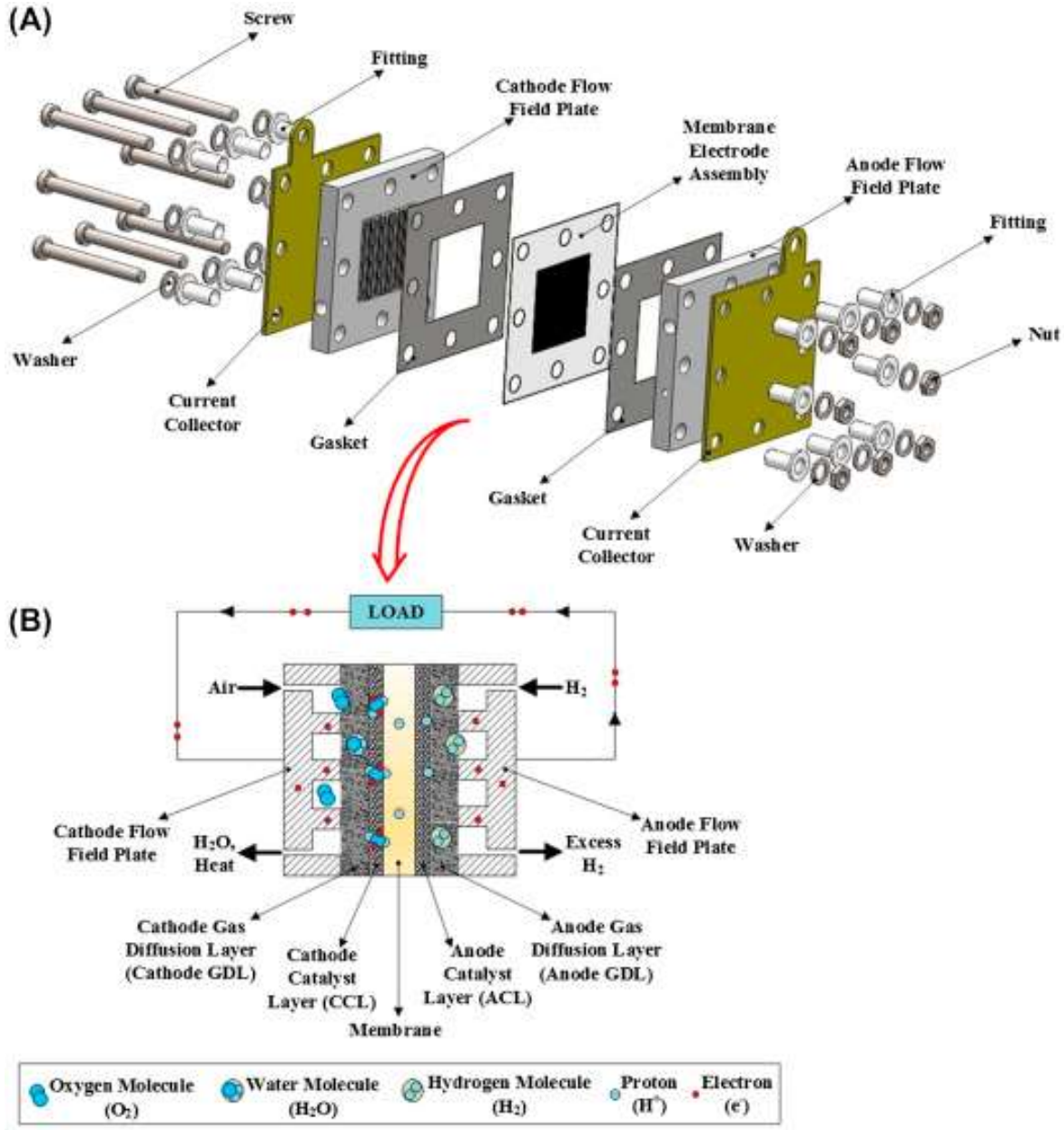

Figure 4: Structure and components of a PEMFC (Ozden, et al., 2018)

Table 1: Summary of MEA Types Manufactured

MEA Type	Commonly referred to as:	Consists Of:
2-layer	Gas Diffusion Electrode (GDE)	An anode or a cathode electrode coated onto a GDL.
3-layer	Catalyst Coated Membrane (CCM)	An anode and a cathode coated on either side of a membrane.
5-layer	Gasketed CCM	A CCM laminated between a pair of sub-gaskets.
7-layer	Complete MEA	A gasketed CCM with GDLs attached on either side.

The components of a PEMFC and their functions are illustrated and summarised in Figure 5 (Yuan, et al., 2021).

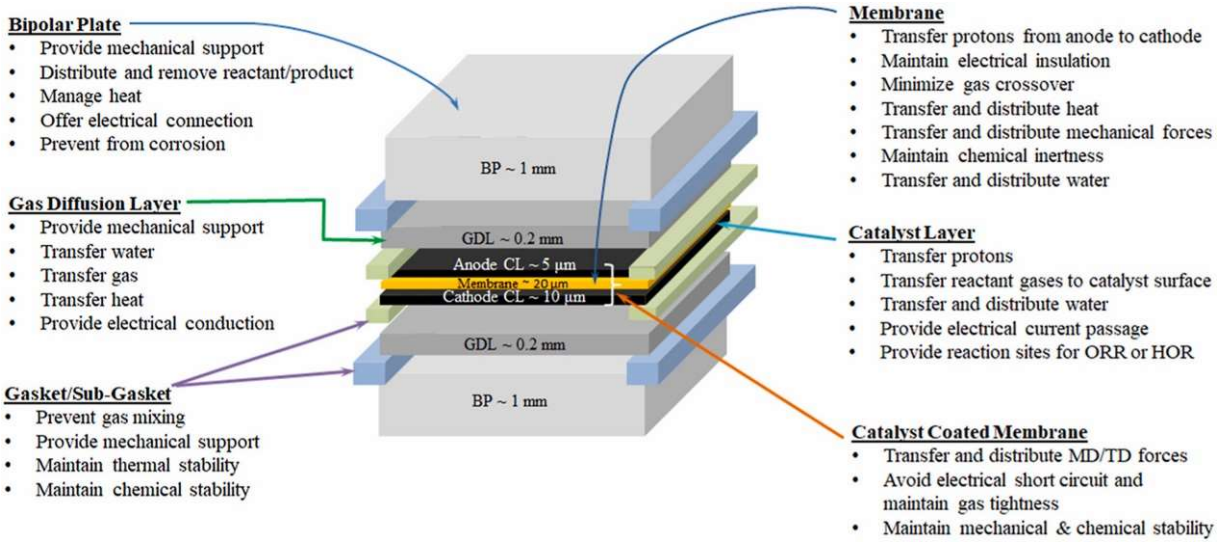

Figure 5: PEMFC components and their main functions (Yuan, et al., 2021)

The polymer electrolyte membrane allows positively charged ions to permeate through but blocks electrons thus forcing them to travel through an external circuit that then generates electrical energy. The cathode CL is coated on one side of the membrane and the anode CL is coated on the other side. The catalyst is applied in the form of an ink which consists of an ionomer (ion-conducting polymer) and a high-surface area carbon support with nano-meter sized particles of platinum. The anode CL enables the splitting of H_2 molecules into protons and electrons and the cathode CL enables the oxygen reduction reaction to occur and produce water. (US Department of Energy, n.d.)

Equation 1:

$$\text{Anode: } H_2 \rightarrow 2H^+ + 2e^-$$

Equation 2:

$$\text{Cathode: } O_2 + 4H^+ + 4e^- \rightarrow 2H_2O$$

The sub-gaskets are a polyethylene terephthalate (PET) based material and come in different thicknesses depending on the compression or application required. The sub-gaskets are used to create a gas-tight seal around the MEA to prevent gases from leaking or crossing over. The GDLs are sheets of carbon paper composed of carbon fibres connected via a polytetrafluoroethylene (PTFE) network.

The GDLs facilitate the transport of reactants and water by allowing gas to diffuse through the pores in the GDL. Hydrophobic PTFE enables the pores to stay open preventing excessive water build-up. Some GDLs are coated with an additional microporous layer (MPL) containing a mix of PTFE and carbon, which is needed to balance the amount of water retained and released to ensure that the conductivity of the membrane is maintained. The bipolar plates are made of metal, carbon or composites. They provide channels for the exchange of gases and allows for multiple MEAs to be connected in series, by acting as an electrical conductor between cells. It is necessary to connect multiple MEAs as each MEA generally produces just under 1 volt and in most applications much higher voltages are required. (US Department of Energy, n.d.)

Figure 6 depicts the cost contributions of the different components in an MEA and in a stack. The catalyst is the most expensive subcomponent in a fuel cell, contributing to nearly 50% of the overall stack cost and is a major factor affecting overall stack performance.

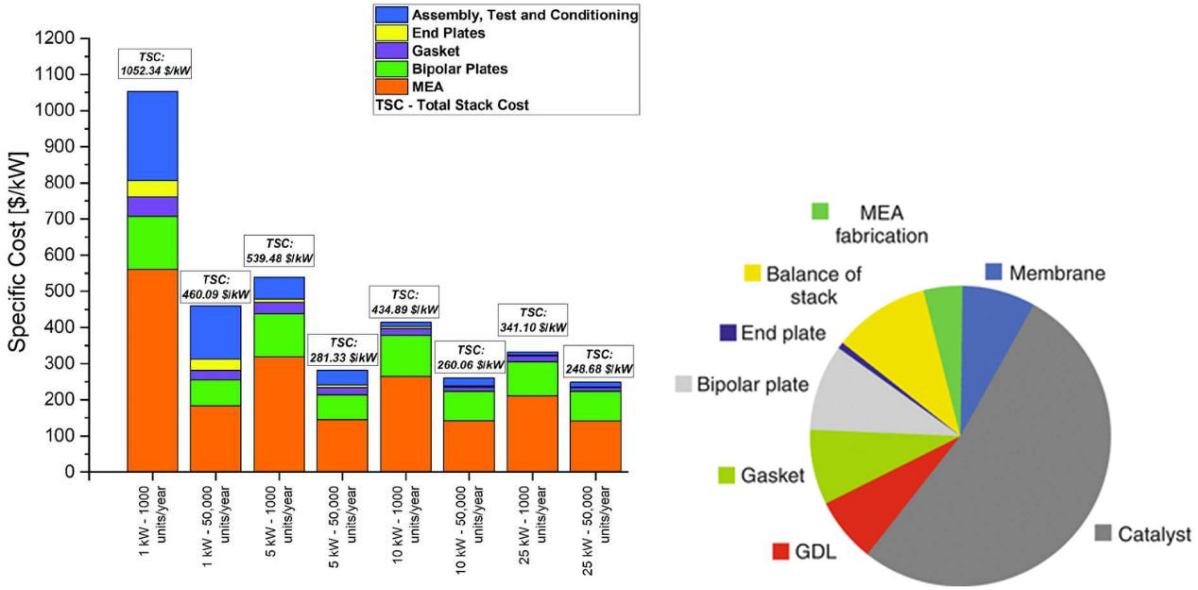

Figure 6: PEM Fuel Cell Stack Cost Breakdown (taken from Cigolotti , Genovese, & Fragiacomo (2021) (left) and Bruijn & Janssen (2012) (right))

2.3.2. MEA Production and Technology

MEAs are produced via 3 routes: 1) coating a CL onto a GDL to create a GDE and then laminating the GDE onto the membrane (Figure 7), 2) coating a decal substrate and then transferring it to the membrane (Figure 8) or 3)) direct coating onto the membrane to produce a CCM (Figure 9) (Prasad, 2019). There are several techniques used for coating, these include doctor blade, mayer rod, screen printing and spraying.

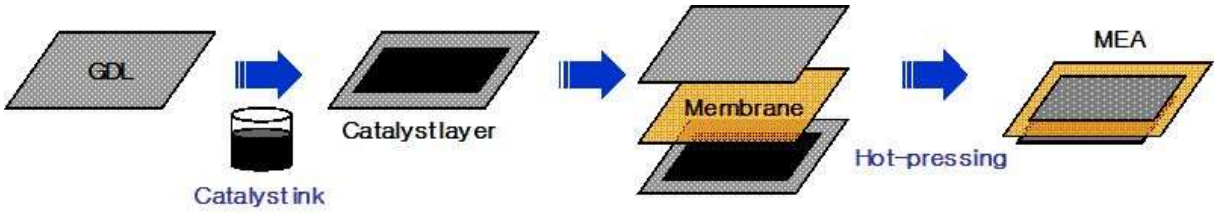

Figure 7: Schematic process of CL coating on a GDL (Pak , You , Choi, & Chang, 2012)

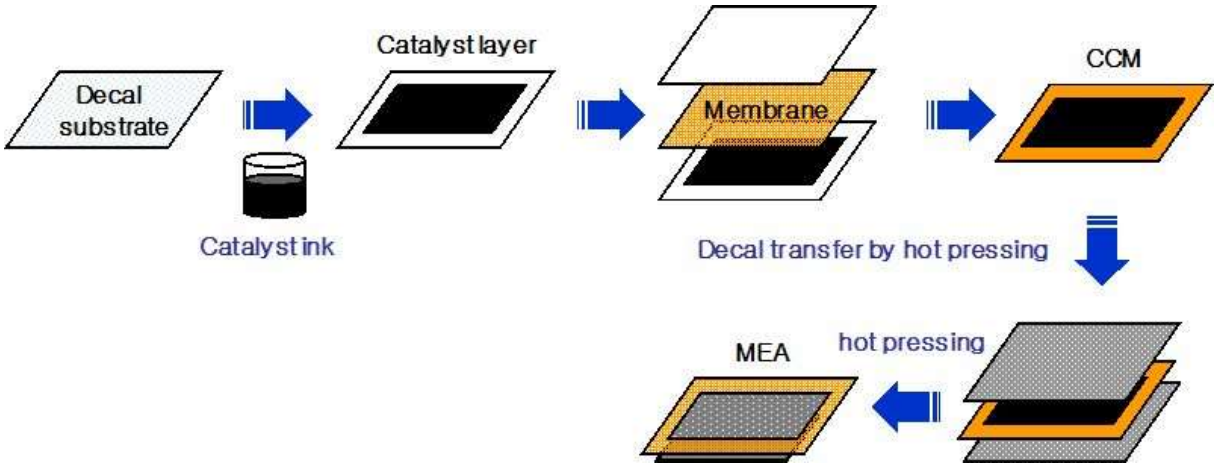

Figure 8: Schematic process of CL coated on a decal (Pak , You , Choi, & Chang, 2012)

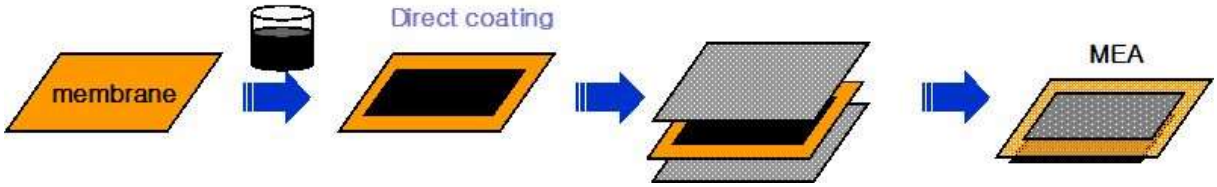

Figure 9: Schematic process of CL coated directly on membrane (Pak , You , Choi, & Chang, 2012)

2.3.3. Quality Control

Formation of defects during MEA fabrication leads to increased manufacturing costs and may affect performance and durability. The formation of defects includes; CL cracks, irregularities in the CL, CL voids, catalyst agglomerations, delamination of CLs, thickness variations, loading variations, scratches, sealant interface defects and membrane pinholes (Figure 10).

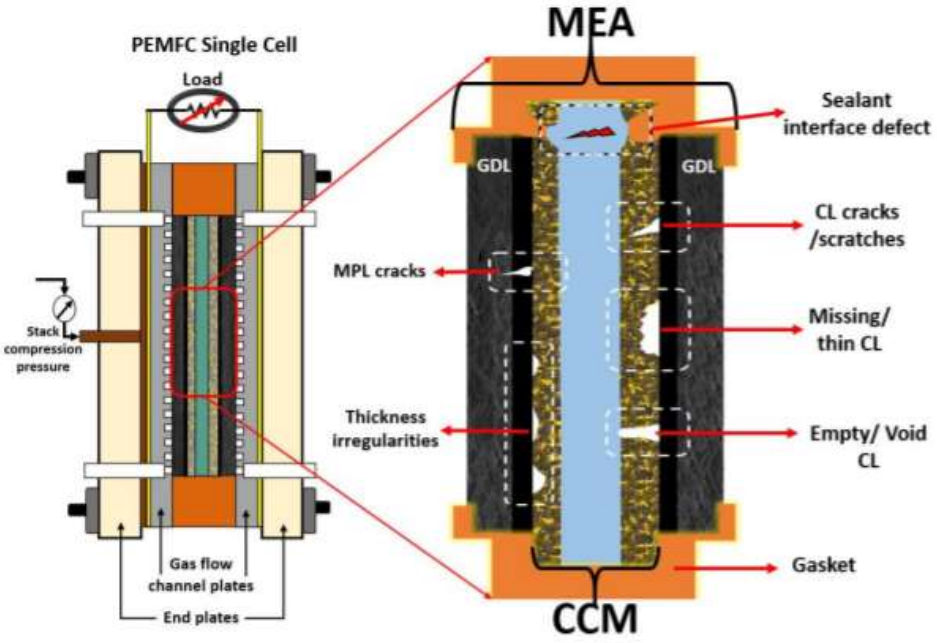

Figure 10: Defects observed in MEA components during fabrications (Prasad (2019))

Some defects, such as CL cracking, delamination of CLs and pinholes can also occur or be propagated during operation via chemical, mechanical and thermal degradation. As a result, they shorten the lifespan, reduce performance and potentially cause catastrophic failure of cells. Defects can be categorised based on severity and priority as summarised in Figure 11. Severity refers to impact on performance and functionality and priority refers to the attention which a defect requires based on their potential to affect performance and functionality.

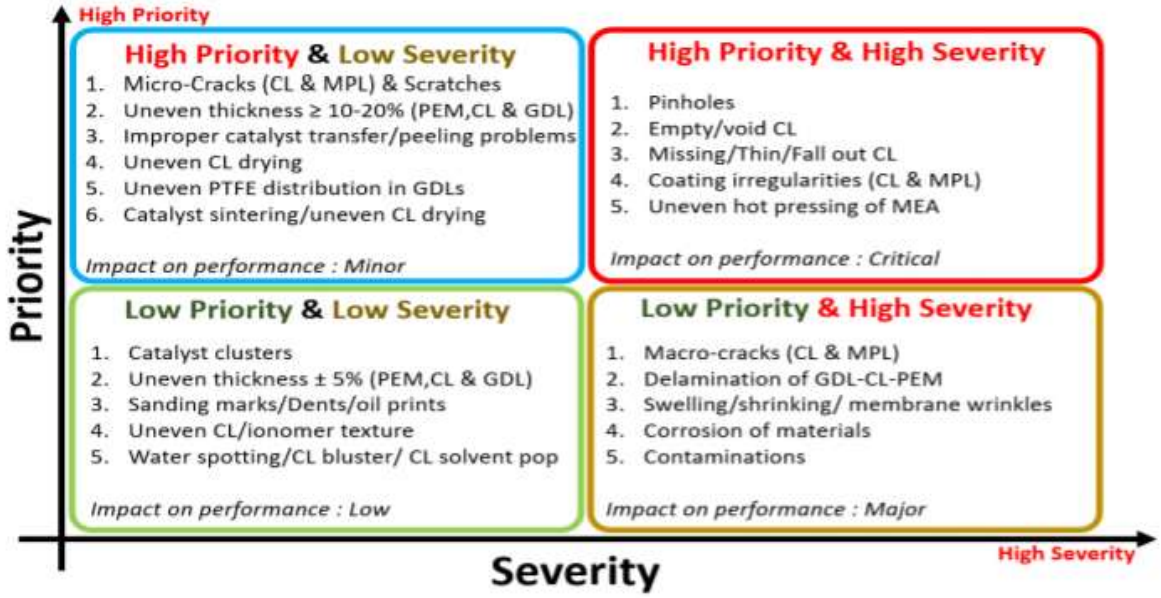

Figure 11: Categorisation of defects (taken from Prasad (2019))

To categorise the defects, the impacts of the most common defects first need to be understood. Table 2 summarises the impact on performance or durability from defects that can occur during fabrication.

Table 2: Types and impacts of defects formed in MEA components (Prasad (2019))

Defect Type	Material Affected	Impact of Defect
Cracks	➢ CL ➢ Membrane	➢ Breaking of CL ➢ Defect propagation ➢ Inhomogeneous current distribution ➢ Radical attack ➢ Increased resistance ➢ Pinhole growth
Voids	➢ CL	➢ Improper catalyst transfer onto membrane ➢ Increased surface resistance ➢ Increased probability of water flood
Delamination	➢ CL ➢ Membrane	➢ Separation of CL ➢ Increased probability of water flooding ➢ Partitioning of CL and membrane across micro-cracks and pinhole areas ➢ Increased activation loss
Pinholes >10µm	➢ Membrane	➢ Performance loss ➢ Combustion of H_2 ➢ Increased stresses ➢ Electrode short-circuiting

2.4. Techniques For Quality Control and Performance Evaluation

2.4.1. Typical Quality control techniques

One of the key barriers hindering fuel cell commercialisation is the lack of standard methods for quality control in MEA manufacturing, specifically the lack of in-line, non-destructive and roll-to-roll quality control methods. In-line quality control testing is a critical enabler in alleviating manufacturing costs by detecting and flagging manufacturing defects thus ensuring a desired quality standard is met at each step in the process. Nonconforming products are detected early and removed at different stages in the process, reducing manufacturing costs that would have otherwise been wasted on defective products. (Yuan, et al., 2021; Phillips, Ulsh , Neyerlin, Porter, & Bender, 2018)

There are currently 5 typical methods for assessing the quality of an MEA. These include gravimetric and thickness analyses which determine the platinum-group metals (PGM) loading versus set targets. These also include visual and optical microscopy inspection which determine the coating quality, CL quality and surface properties. Lastly, single cell performance characterisation is used to determine the performance and durability to detect defective MEAs that have been missed by or that could not be picked up by the other quality control methods. (Yuan, et al., 2021; Prasad, 2019)

Visual inspection involves placing the MEA on a backlit table. The opacity and light translucency seen by eye is then used to gauge the quality of the MEA. Uniform opacity across the MEA is linked to low PGM loading, whereas light translucency is linked to the quality of coating.

Optical microscopy inspection involves placing the MEA under a light microscope and evaluating the surface properties by illuminating the surface or evaluating the opacity and amount of light translucency by illuminating the MEA from below. The latter is similar to the visual inspection at a higher resolution. Whereas the surface properties can assist in identifying defects such as cracks in the CL, uncoated areas or uneven coating.

Gravimetric analysis involves taking an initial mass of the membrane prior to coating and a final mass after coating to calculate the PGM loading. Similarly, measuring the thickness involves taking an initial thickness of the membrane prior to coating and a final thickness after coating to calculate the PGM loading based on known thickness to loading ratios. In addition, the thickness can also assist in determining the distribution of the layer coated.

Single cell performance characterisation (Figure 12) is an electrochemical characterisation method, which uses cyclic voltammetry and current-voltage polarisation to provide the most reliable measure of quality control in the means of performance data. However, the MEA from testing cannot be recovered thus it is a destructive quality control measure. Due to the destructive nature of this method, only selected samples are tested and it must be assumed the other MEAs manufactured during the same run are all of the same standard. Furthermore, this method cannot be run in line with production and is time consuming compared to the other methods. As a result it is difficult to create a feedback loop using this method.

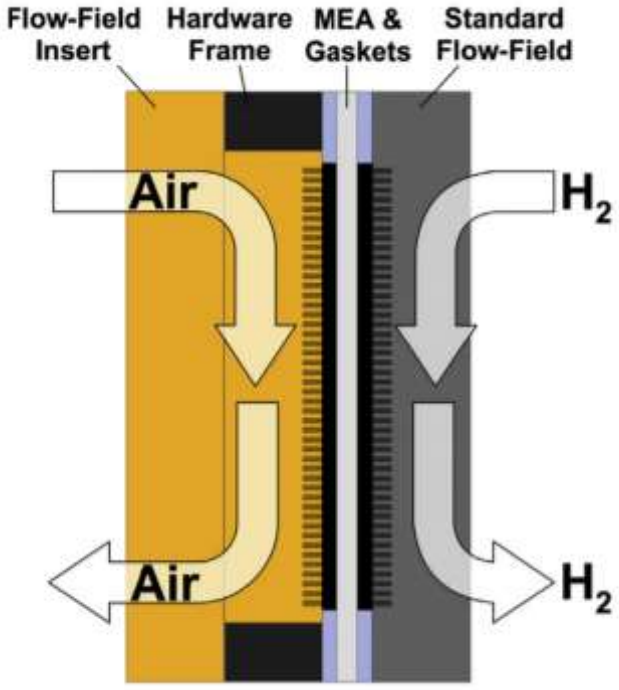

Figure 12: Schematic of single cell characterisation (Phillips, Ulsh , Neyerlin, Porter, & Bender, 2018)

Scanning Electron Microscopy (SEM) analysis and single cell performance characterisation, discussed further in Section 2.4.3.1 and 2.4.1.2, are destructive quality control methods. In addition, these methods are time consuming and cannot be run in line with manufacturing.

2.4.3.1. Scanning Electron Microscopy

SEM analysis uses a focused electron beam to obtain a high-resolution image a samples' topography. SEM analysis allows for information on the surface layer, up to 1 µm in depth, to be obtained. The high magnification and depth of field make it advantageous over other microscopy techniques. (Vernon-Parry, 2000)

An electron source in the microscope emits an electron beam on the surface of the sample and secondary or backscattered electrons, are measured relative to the position of the incident electron (Niemantsverdriet). This is further described in the Table 3 and shown in Figure 13 based on the sample response and its use.

Table 3: Resulting SEM electrons (Vernon-Parry, 2000)

Sample Response	Origin	Energies	Image Resolution	Use
Secondary electrons	Removed from their orbitals by incident electrons.	Low energies – > 50eV	Higher resolution as electrons are emitted from near the surface	Topographic information
Back-scattered electrons	Incident electrons scattered from the surface at a specific angle after approaching the nucleus	High energies	Lower resolution	Compositional and crystallographic information

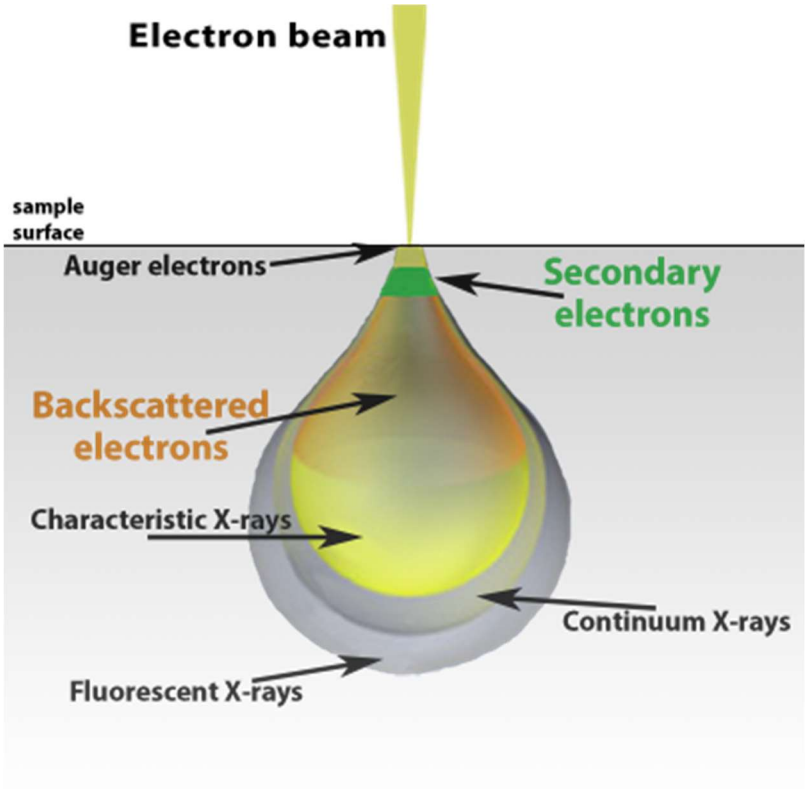

Figure 13: Schematic of electron beam interaction (NanoScience Instruments , n.d.)

The components of the SEM instrument include the electron column with an electron gun, the specimen chamber and the computer which controls the system. The electron gun is responsible for generating the electrons which travel down the column - the acceleration as well as the magnitude of the electrons can be controlled. The lens is responsible for producing the image by demagnification or focusing of the electron beam. The electrons are passed through the lens and the electron beam is rasterised to form the image. The specimen chamber primarily consists of a sample stage, a sample holder, a camera and detectors. The specimen can be mechanically moved in different directions. It is important for the microscope to be kept under vacuum to prevent contamination and interference with the electron beam. (Cheney , 2007; Nixon, 1971; Ul-Hamid, 2018)

2.4.1.2. Single Cell Performance Characterisation

Single cell performance characterisation is a vital quality control parameter that cannot be substituted for alternate methods as one of the main challenges for competitive fuel cell systems are stack performance and durability. The reliability of single cell performance characterisation and benchmark results is crucial, as many parameters can impact the results. This includes using different hardware and procedures for testing. An international standard (IEC/TS 62282-7-1) exists for single cell performance characterisation, which includes test hardware, cell assembly, test procedures and test reports. Furthermore, the SAE J2617 standard summarises test procedures for performance tests of PEMFC stacks for automotive applications. The procedures include OCV tests, polarisation curves, sensitivity sweeps and voltage response tests. (Mitzel, et al., 2016)

When setting up test conditions, it should be noted that an operating single cell PEMFC is not isothermal due to thermal power generation and finite thermal conductivities of components.

Therefore, the cell temperature will be an average of temperatures at various locations and the temperature profile cannot be measured or controlled. Single cell bipolar plates can also use a co-flow or a counter-flow configuration between the reactants and coolant. High reactant stoichiometry associated with high reactant flow are favoured as the water produced can be easily removed whereas low reactant ratios and flows result in water accumulation and cell flooding. The operating conditions for tests are application and design specific within certain parameters. The parameters often considered are; active area, bubbler temperatures, back pressure, cell temperature, cell design and manufacturer, cell compression and reactant feed temperatures, flowrates and stoichiometry. The electrochemical techniques used for quality control during testing are the polarisation curve, electrochemical impedance spectroscopy, cyclic voltammetry and current interruptions. (Mitzel, et al., 2016)

2.4.1.2.1. Polarisation Curves

A polarisation curve is an essential and powerful electrochemical technique used for performance characterisation. A pol curve is obtained by plotting the cell potential against the current density under a set of constant operating conditions, such as temperature, pressure, active area, reactant stoichiometry and reactant flowrate. The current density is obtained by dividing the current output by the geometric active area of the MEA, allowing for normalization. The polarisation curve can be converted to a power density versus current density plot by multiplying the cell potential by the current density at each point of the curve. There are three major regions in a polarisation curve (Figure 14), i.e. the activation polarisation region at low current densities, the ohmic polarisation region at intermediate current densities and the concentration polarisation region at high current densities. In the activation polarisation region, the cell potential experiences sharp drops mainly due to the sluggish kinetics of the ORR (equation 2, section 2.3.1). In the ohmic polarisation region, cell potential losses are mainly due to ohmic resistance which result from the resistance to the flow of ions in the membrane and resistance to flow of electrons through the electrode, bi-polar plate and current collector interfaces. In the concentration polarisation region, cell potential losses are mainly due to mass transport limitations of the reactant gas and product water through the pore structure of the GDLs and CLs. (Wu, et al., 2008)

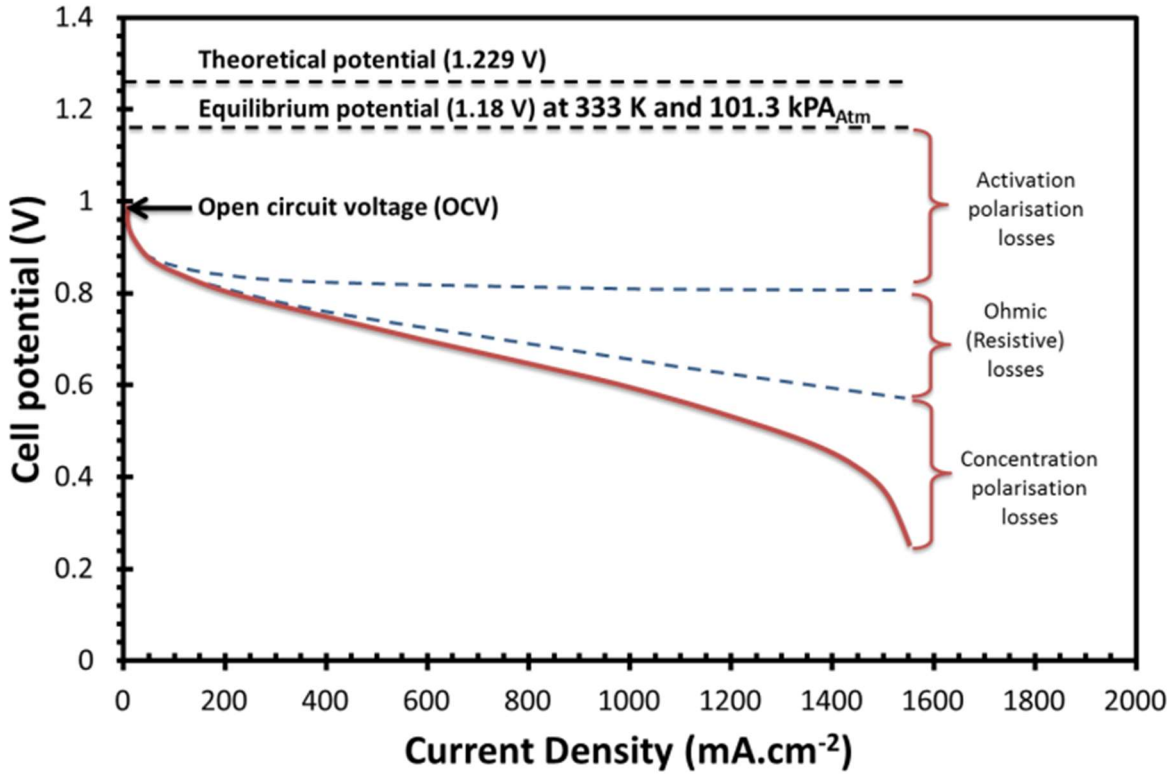

Figure 14: Typical Polarisation Curve: H_2-Air Operation (Barbir, 2005)

In an ideal case, the voltage (also known as the Nernst potential) is given by *equation 3* below. In practice, the OCV is slightly less and the cell voltage varies due to activation, ohmic and mass transport losses. The cell voltage is represented by *equation 4*, which accounts for the losses formerly described. (Labi , 2019)

$$E = -\frac{\Delta g_f}{2F} = -\frac{\Delta g_f^0}{2F} + \frac{RT_{fc}}{2F}\ln\left[\frac{P_{H_2}P_{O_2}^{0.5}}{P_{H_2O}}\right]$$

Equation 3

$$V_{fc} = E - V_{act} - V_{ohm} - V_{conc}$$

Equation 4

Whilst polarisation curves speak to the overall performance, they cannot produce performance information of individual components within the cell and cannot differentiate between different failure mechanisms. Therefore, EIS and other electrochemical techniques are used to accomplish the latter. (Wu, et al., 2008)

2.4.1.2.2. Electrochemical Impedance Spectrometry

Electrochemical Impedance Spectrometry (EIS) is an electrochemical technique that measures the impedance of a system as a result of the AC potential frequency. Impedance is the ratio between voltage oscillation and electric current density oscillation and is measured in ohms. EIS measures the ability of a system to impede the flow of electrical current by repeatedly applying an AC voltage or

current perturbation of known amplitude and frequency to the cell and then measuring the resulting amplitude and phase as a function of frequency. Common uses of EIS in PEMFCs include studying the ORR, characterising transport losses, evaluating ohmic resistance, electrode properties and MEA operating condition optimisation, equivalent circuit modelling and performance differentiation of each component. (Baricci, et al., 2019; Wu, et al., 2008; Yuan, Sun, & Zhang, 2007)

An equivalent circuit is an electrical circuit modelled to the system to extract meaningful data from different regions as shown in Figure 15. Resistors (R), Capacitors (C), Inductors (L) and the Warburg element (Z_W) are used to model the circuit. Resistors represent the Faradaic resistance of the electrochemical reactions, the capacitors represent the double-layer capacitance of the electrode interface and the Warburg element (Z_W) is needed to represent the diffusion and mass transport impedances of the cell. (Labi , 2019)

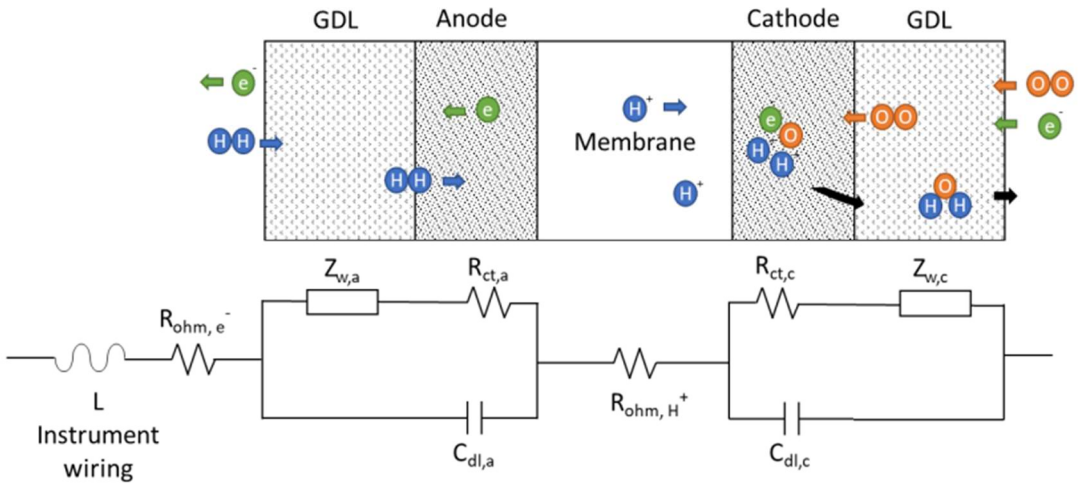

Figure 15: Equivalent circuit modelled for a fuel cell (Labi (2019))

Bode and Nyquist plots are used to represent the impedance spectra. The amplitude and phase of the impedance is plotted as a function of frequency in a Bode plot. The imaginary impedance is plotted against the real impedance at each frequency, increasing from right to left, for a Nyquist plot (Figure 16). The real and imaginary parts are obtained from the vector, where the real part impedance is the resistance caused by the resistors in a circuit and the imaginary part is the resistance caused by a capacitator and inductor in a circuit. In the resulting plot, there are four main regions which correspond to the potential losses seen in the polarisation curves, i.e. ohmic, anode activation, cathode activation and mass transport effects. The first intercept corresponds to the ohmic resistance of the membrane, the high frequency arc reflects the double-layer capacitance in the CLs and the effective charge transfer resistance and the low frequency arc reflects the impedance due to mass transport limitations. A larger semi-circle is usually observed for the cathodic charge transfer resistance as opposed to the anodic charge transfer resistance due to the sluggish kinetics of the ORR resulting in the cathodic activation losses outweighing the anodic activation losses. The frequency ranges between 0.1-10000 Hz. At high frequency (>100 Hz) the HOR and ionic/electron conduction are prominent, at intermediate frequency (1-100 Hz) the ORR is prominent and at low frequency (<1 Hz) the effects of mass transport are prominent. (Wu, et al., 2008; Labi , 2019)

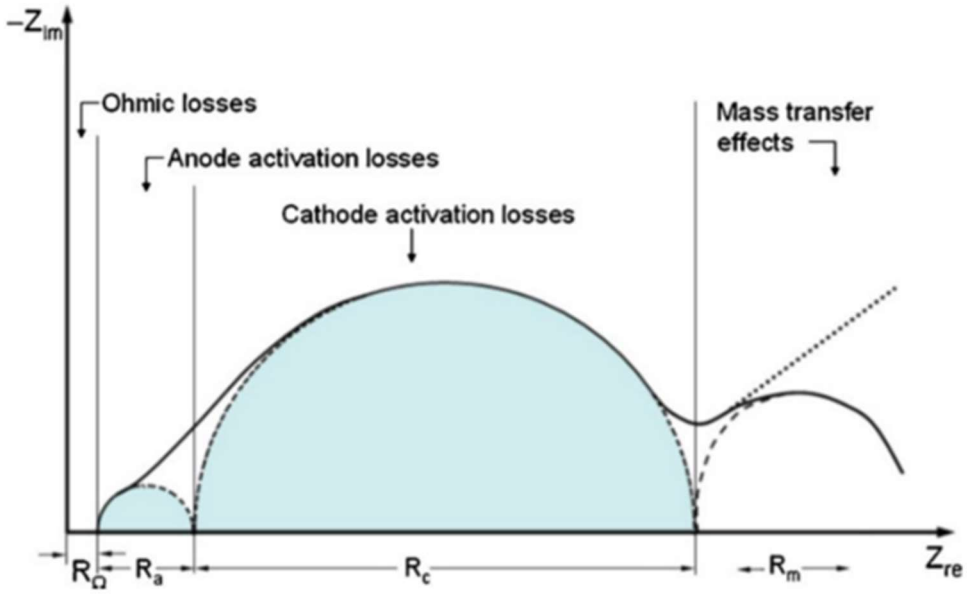

Figure 16: Typical Nyquist plot generated by EIS (Zhu , Payne, & Tatarchuk (2007))

2.4.2. Recently Developed Quality control techniques

The development of efficient, contactless and non-destructive techniques is necessary for the improvement of quality control (Prasad, 2019). The development of IRT and XRF spectroscopy have gained momentum over the last few years. IRT assists with determining CL quality, membrane defects (such as pinholes or microtears), gasket quality and GDL quality. XRF spectroscopy assists with determining PGM loading and surface properties. It is vital that the methods be rapid, non-contact and non-destructive during the quality analysis stages. NREL has demonstrated the feasibility of 100% inspection of moving fuel cell material, which is generally the case with high-volume roll-to-roll manufacturing (Bender, Felt, & Ulsh, 2014) and *Yuan et al. (2021)* has demonstrated the value of using the technique for ex-situ durability testing.

2.4.2.1. Infrared Thermography

Technological improvements and reduced costs of IR cameras has led to the development of IRT as a non-destructive diagnostic technique. IRT has a high resolution, a very sensitive detection and is considered a viable choice for quality control. It is applied in various fields for defect detection in metal surfaces, membrane folds, CL defects, concrete structures and conduct surface analysis. The IRT technique can be used to detect sub-millimetre pinholes and unsealed gasket areas as a result of the heat signature created from H_2 crossing over and combusting with oxygen. IRT detects emitted radiation in the infrared range (700-1000 nm) of the electromagnetic spectrum which corresponds to wavelengths longer than the visible light portion (400-700 nm) of the spectrum and is thus able to create images in total darkness (Haynes, 2011). The thermal camera functions at ambient temperature and senses the heat emitted from an object. The heat signature is then converted into an image using the changes in resistance, voltage or current. (Wang, Yuan, & Li, 2012).

The suggested setups for IRT rigs are shown in Figure 17 and Figure 18 below. The methods proposed by *Phillips et al. (2018)* and *Prasad (2019)* are similar to fuel cell mode testing, however, the cathode flow-field is removed and replaced with a convective air flow and IR camera.

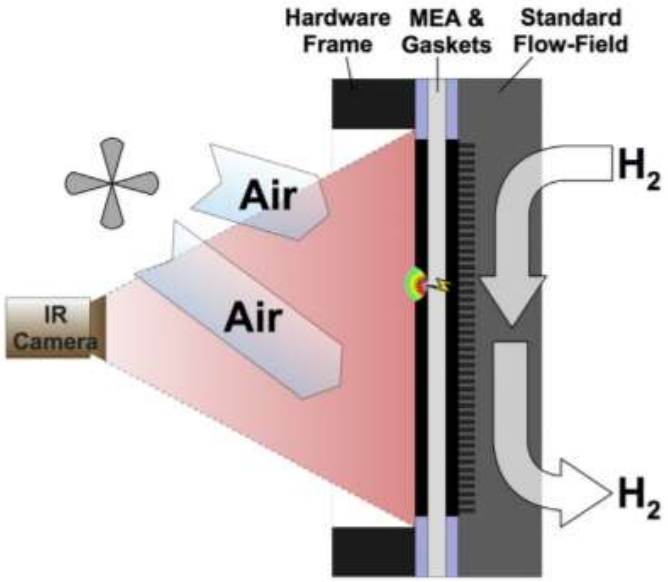

Figure 17: Schematic of IRT Test Rig (Phillips, Ulsh , Neyerlin, Porter, & Bender, 2018)

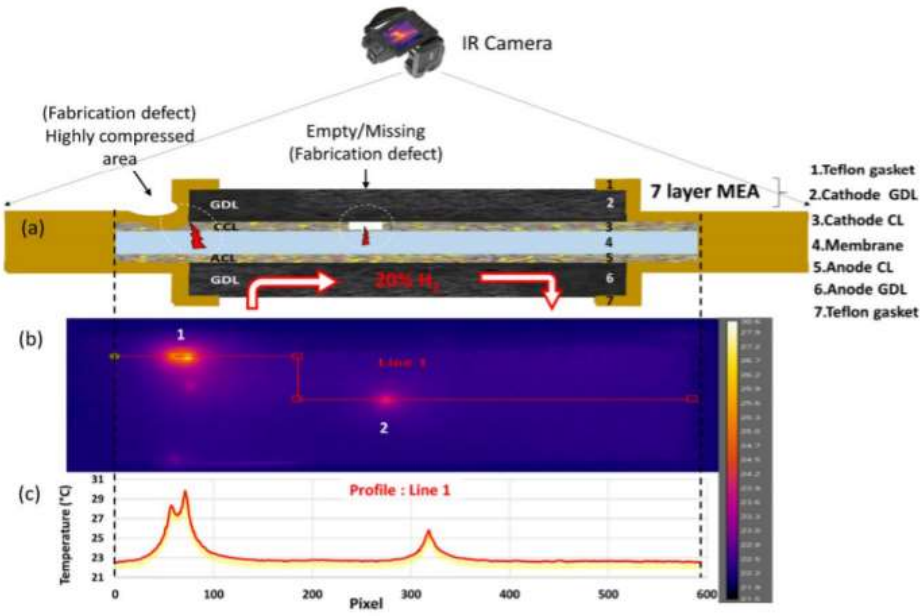

Figure 18: Schematic of IRT Test Rig (Prasad, 2019)

Phillips et al. (2018) reports enabling IRT by stopping cell operation during single cell performance characterisation, reducing the electrode pressures to ambient, cooling the humidifiers, lines and the cell (which is suggested to take 30 minutes) and then removing the cathode flow-field while keeping the MEA in place (Figure 18). In-situ thermography measurements are then taken by generating a thermal response, to generate the thermal response, H_2 is flowed over the anode while the cathode is exposed to air. If there is H_2 crossover via any defective points, an exothermic reaction will occur generating a heat signature. The thermal response can then be correlated to different defect

parameters and a method can be developed to detect defects – such as the different thermal responses seen over variable CL thickness (Figure 19). *Aieta et al. (2012)* provides the methodology for correlating thermal responses by mapping thermal deviations against defects such as catalyst reduction.

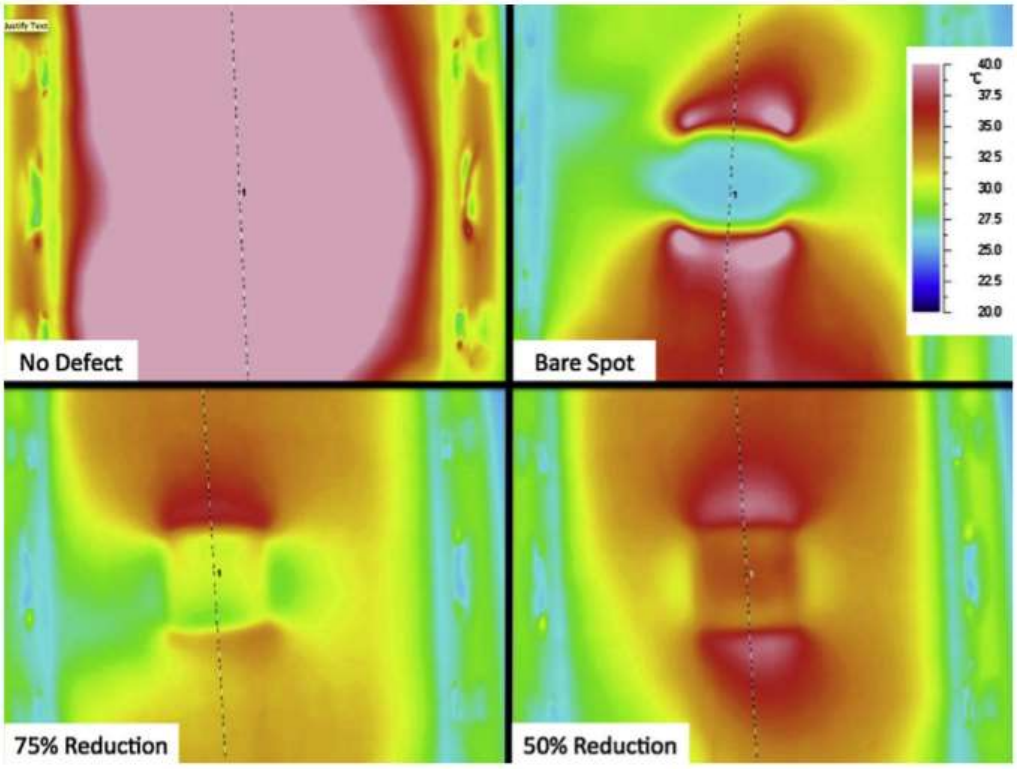

Figure 19: Thermal response of a good MEA (100% target loading), a bare spot (100% reduction), 75% reduction and 50% reduction in CL thickness (Aieta, et al., 2012)

IRT was initially developed for military use and later developed into a wide range of applications such as; astronomical devices, night vision equipment, firefighting operations, search and rescue operations, predictive maintenance on mechanical and electrical equipment, process monitoring, moisture detection, chemical imaging, medical testing, quality control in production, research and development, quarantine monitoring and flame detection (Wang, Yuan, & Li, 2012). NREL has shown that the technique can be implemented in high volume continuous coating applications, such as roll-to-roll manufacturing of MEAs (Figure 20) (Bender, Felt, & Ulsh, 2014). IRT applications in the PEMFC industry now include assessing H_2 crossover, membrane thickness, membrane degradation, in-situ temperature mapping and material screening (Wang, Yuan, & Li, 2012).

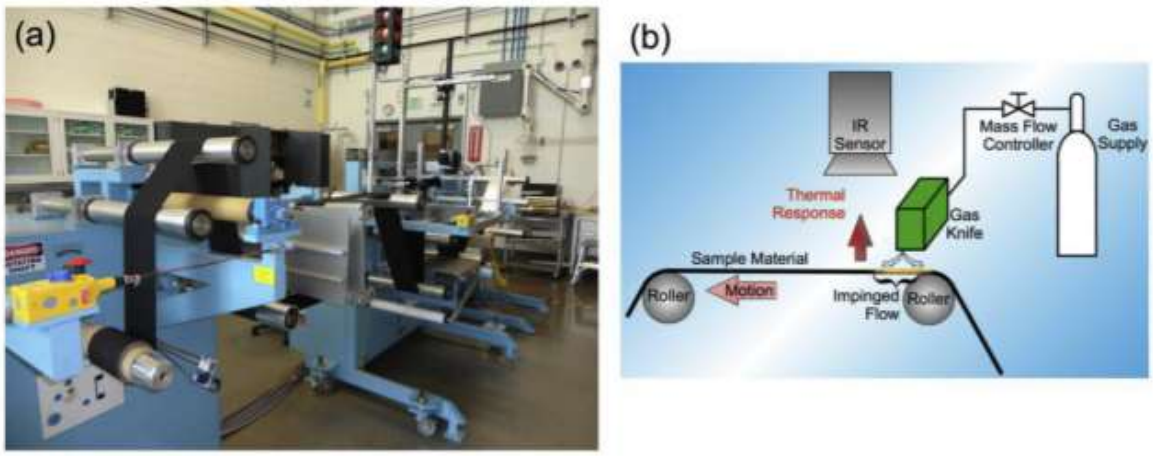

Figure 20: a) Roll-to-roll manufacturing line at NREL. b) Schematic of IRT setup. (Bender, Felt, & Ulsh, 2014)

2.4.2.2. XRF Spectroscopy

X-rays are formed by oscillations in the electro-magnetic field at a wavelength of 0.01-10 nm, placing them between the ultraviolet and gamma-ray spectra (Haynes, 2011). XRF spectrometry is a rapid, accurate and non-destructive technique that is able to measure compositions from as low as ppm to 100% (Wang, Yuan, & Li, 2012). The XRF process shown in Figure 21 involves irradiating a solid or liquid sample with high energy X-ray from a controlled tube. When an X-ray with sufficient energy, which is greater than an atom's shell binding energy, strikes an atom an electron from the inner shell is dislodged. The atom stabilises by filling the vacant space with an electron from a higher orbital shell and the electron drops to a lower energy state by releasing a fluorescent X-ray. The energy of emitted X-rays is detected and plotted against the X-ray count rate to obtain the characteristic spectrum. Qualitative analysis is enabled via analysis of the peak energy positions that are characteristic for the elements present within the samples, while the quantitative analysis is enabled via measurements of peak intensities. (ThermoFisher Scientific, 2020)

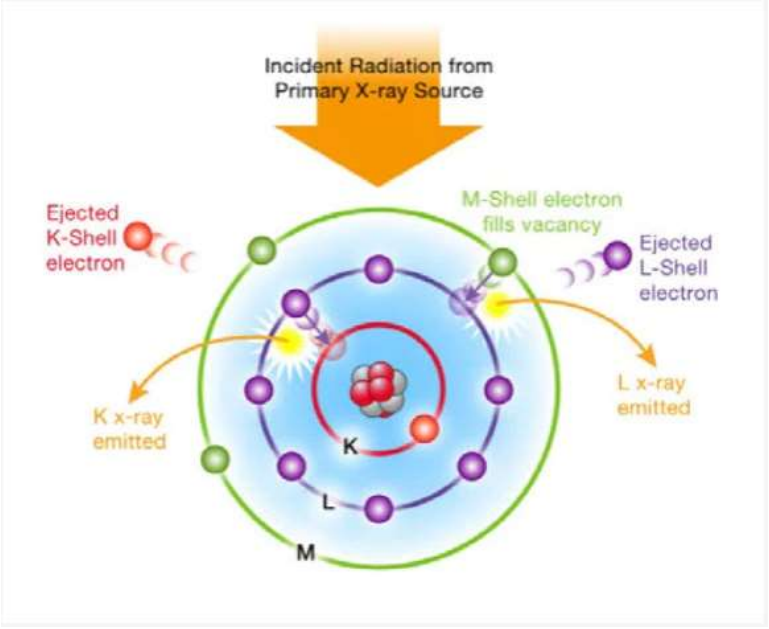

Figure 21: Depiction of the XRF process (ThermoFisher Scientific, 2020)

XRF analysers are used in a wide range of applications which include; scrap sorting, alloy grade identification, quality control in metal manufacturing, geological exploration, mining, testing industrial materials and testing for contaminants in consumer products (Olympus Industrial Solutions, 2021). In PEMFC manufacturing, portable spectrometers are employed to measure catalyst loadings and CL thickness in laboratory scale MEA manufacturing. To identify CL loadings and thickness, a calibration for the types of inks (or catalysts) is required. This involves generating X-ray peak intensities for known elements and loadings and then linear fitting the data to generate a calibration curve (Figure 22). (Chourashiya, Sharma, & Andersen, 2018; Wang, Yuan, & Li, 2012)

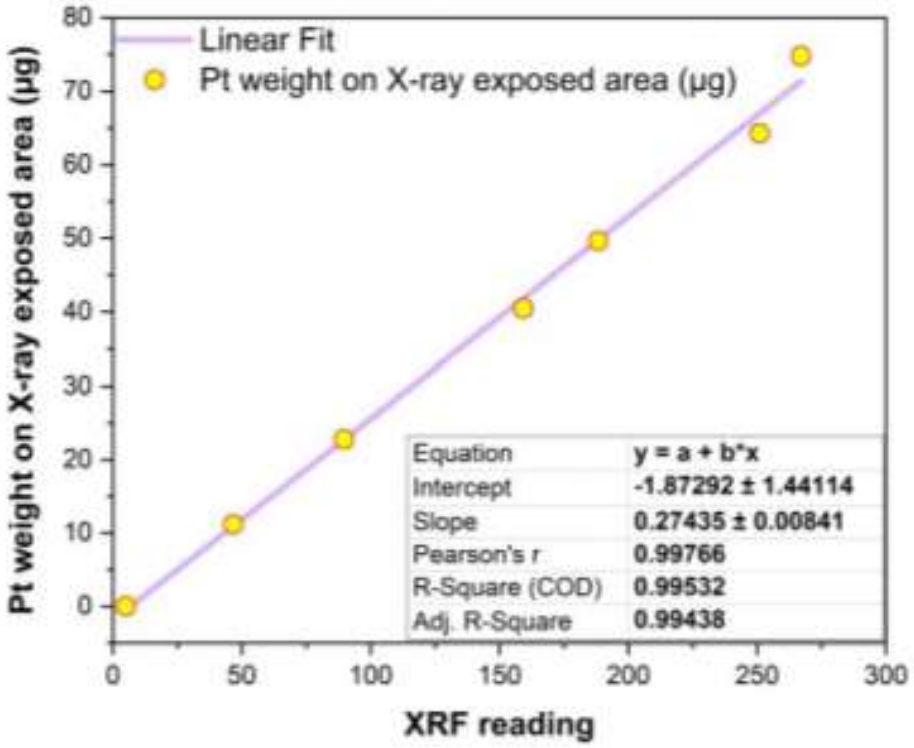

Figure 22: Calibration of XRF Spectrometer (Chourashiya, Sharma, & Andersen, 2018)

One of the challenges with XRF is that it is subject to significant matrix effects, which need to be corrected in order to obtain accurate quantitative results. The matrix effects are a result of absorption and enhancement that affect the magnitude of the analyte signal. Hand-held XRF devices typically come with software that is programmed with algorithms that apply the appropriate matrix effect corrections without user involvement. (Bowers, 2019)

X-rays need to pass through the surface layer to reach the atoms inside a sample, which results in the surface layer absorbing some of the incoming radiation. The characteristic radiation produced also has to pass through the surface layer to leave the sample, once again resulting in some of the radiation being absorbed by the surface layer. Both of which are depicted in Figure 23. (Brouwer, 2003)

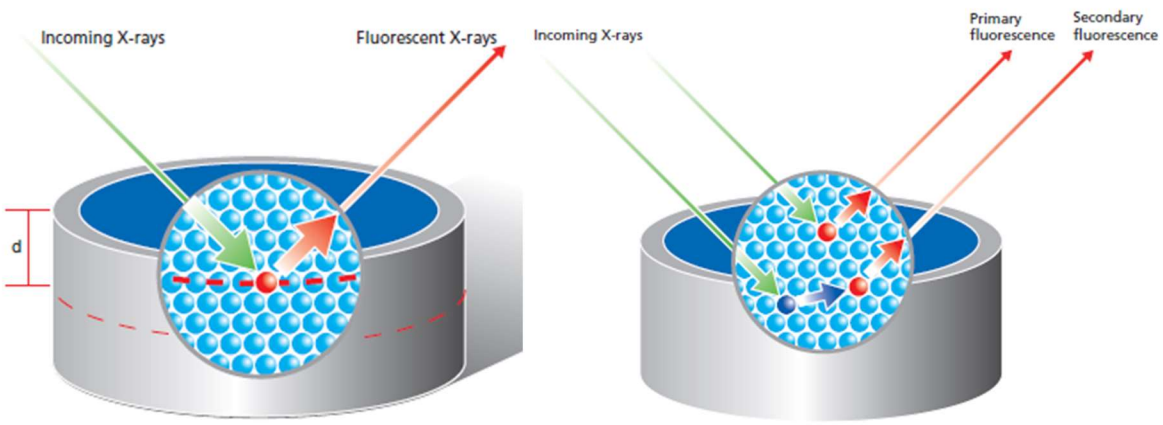

Figure 23: Absorption of incoming fluorescent rays (left) and emission of primary and secondary fluorescence (right) (Brouwer, 2003)

The magnitude of the absorption is dependent on the radiation energy, path length, density and atomic number. Absorption increases with an increase in path length, density and atomic number and a decrease in radiation energy. Absorption can become so high that elements deeper in the sample cannot be reached by the incoming radiation or that characteristic radiation cannot leave the sample. As a result, only elements that are close to the surface are measured. Therefore, as the sample gets thicker, more radiation is absorbed and the limit at which radiation can no longer leave the sample is dependent on the material. (Brouwer, 2003)

CHAPTER III: RESEARCH APPROACH

The scope, objectives and limitations are presented in this chapter to guide the overall approach taken in the thesis based on the literature review in the Chapter 2.

One of the key challenges hindering fuel cell commercialisation is the lack of standard methods for quality control in MEA manufacturing, specifically the lack of in-line, non-destructive and roll-to-roll quality control methods. In-line quality control testing is a critical enabler in alleviating manufacturing costs by detecting and flagging manufacturing defects and ensuring a desired quality standard is met at each step in the process. Nonconforming products are detected early and removed at different stages in the process, reducing manufacturing costs that would have otherwise been wasted on defective product.

Another challenge is transitioning from labour-intensive manufacturing to high-throughput manufacturing to meet volume and target costs (Ulsh, n.d.). However, to obtain high yields in continuous manufacturing processes, it is important to measure the quality of the products made as defective products affect performance and increase costs downstream. To achieve this, improvements in typical quality control methods used are required to allow for real time, contactless detection of defects.

The focus of this study is to address some of the engineering and manufacturing limitations, which contribute to high manufacturing costs, low production volumes and performance issues associated with MEA fabrication. Defect development and detection during manufacturing is targeted by improving typical quality control techniques used and developing methods for local use of newer quality control techniques. The research objectives for this study were as follows:

- Automate Visual Inspection to be able to capture results digitally, thus moving away from it being labour intensive. To achieve this a rig was built and a method was developed for capturing and processing the images to allow for more in-depth and improved quality control that overlaps the need for optical microscopy analysis.
- An IRT rig was built and a method was developed for its use in defect detection. Developing the method locally was necessary because even though it has been developed in industry, information on protocols for testing and use of IRT as a QC technique in MEA manufacturing is limited.
- A method was developed for using XRF spectroscopy to determine PGM loading. Developing the method locally was necessary because even though it has been developed in industry, information on protocols for testing and use of XRF as a QC technique in MEA manufacturing is limited.
- The XRF technology was incorporated into a high-volume production line.

The manufacturing mode for the purpose of method development was low volume manufacturing with single patch coated MEAs and multiple flush coated MEAs. The methods developed under this study were Generation I and further improvement of the methods will need to be investigated in future studies due to the time and budget constraints on this study. The study focussed on the quality control during manufacturing of 3-layer and 5-layer MEAs.

CHAPTER IV: MATERIALS AND EXPERIMENTAL METHODS

This chapter details the materials used and experimental methods which were undertaken to fabricate the MEAs, set up the quality control methods, develop the methods for some of the quality control techniques and analyse the MEAs produced.

4.1. MEA Fabrication

Figure 24 below illustrates the MEA fabrication process that was followed (grey). It further illustrates where the method development and quality control testing fitted into the process.

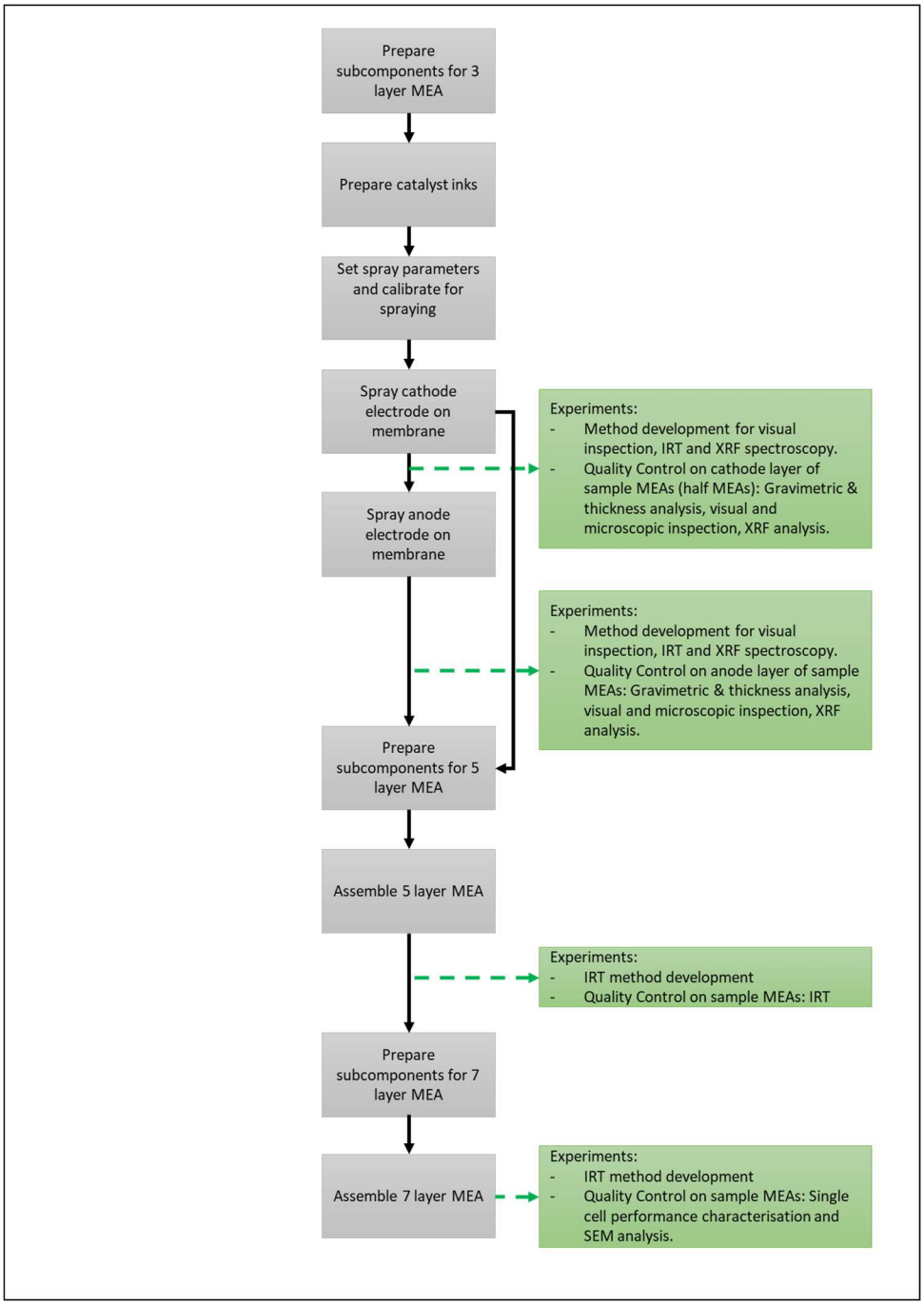

Figure 24: MEA Fabrication Method

4.1.1. List of chemicals and materials

Table 4 lists the chemicals and materials that were used throughout the study.

Table 4: List of chemicals and materials

Chemical / Material	Supplier	Specification
Catalyst	HyPlat	HTK40 40 wt% Pt on high surface area advanced carbon support
Deionised Water	N/A	18.2 MΩ.cm
Isopropanol	Kimix	Analytical grade - 99.9% purity Chemical formula: C_3H_7OH
Ionomer	HyPlat	Aquivion dispersion D72-25BS Solids content: 26 wt.% Specific gravity: 1.147 g/cm^3
Membrane	HyPlat	NC700 Thickness: 15 µm
Membrane	Fuel Cell Store	N115 Thickness: 125 µm
Membrane	Fuel Cell Store	NR212 Thickness: 50.8 µm
Mylar	HyPlat	Thickness: 50 µm
Gasket	HyPlat	32 um PET
GDL	Fuel Cell Store	MB30 80-95% Carbon and 5-20% PTFE Thickness: 198 µm Area Weight: 55 g/m^2 Density: 0.28 g/cc
Double Sided Adhesive	HyPlat	Transfer Adhesive Film Thickness: 9 µm
H_2 Test Gas	Syngas	Purity grade: 99.999%
Nitrogen Test Gas	Air Products	Purity grade: 99.999%
Synthetic Air Test Gas	Air Products	N/A
Resin	Advanced Laboratory Solutions	
Hardener	Advanced Laboratory Solutions	
Silicon Carbide Grinding Paper	Advanced Laboratory Solutions	250 mm SIC paper Grit: 500, 800, 1200, 2400
Carbon Conductive Tape	TechInstro	Width: 8 mm Tape Thickness: 160 µm Adhesive Thickness: 15 µm Resistance: 5 Ω/sq

In research conducted by Yuan, Sun, & Zhang (2007), it was reported that membranes of different thickness had different resistances and influenced charge and mass transfers in the EIS. It was also

reported that thinner membranes show better performance and are less sensitive to humidification conditions, temperature changes, and changes in current density. For that reason, three commercially used membranes were chosen in this work for the XRF method development with thicknesses ranging between 15-125 µm (Table 4*)*. From the three membranes, NC700 (15 µm thickness) was chosen as the membrane for all the other experimental work due to its stability against humidity and temperature variations during the coating process.

4.1.2. Catalyst ink formulation and preparation

The catalyst powder is combined with water and isopropanol under agitation to form an ink. The ink is high shear stirred at 9000 rpm for 5 minutes and then ultra-high shear stirred to ensure a homogenous ink is produced. The ink is then analysed by means of a solids content analysis before being used for coating. To vary the ionomer content for the XRF method development samples, the required amounts of ionomer were measured out and mixed into subsamples of the main ink batch. The adjusted ink was then high shear stirred at 9000 rpm for 5 minutes and analysed by means of a solid content analysis before being used for coating.

4.1.3. CCM Spraying and MEA Assembly

Spray coating is used to deposit an ink onto a substrate and involves atomising the ink for a highly dispersed and even deposition (Figure 25). For the scope of this study, coating was done using USI's Prism 300 Ultracoat (Figure 26). The Prism 300 makes use of thin coating application technology which is superior to conventional air-atomising or ultrasonic spray nozzles. The ultrasonic spraying is combined with a high-performance programmable motion and control platform which is used for direct coating of catalyst inks onto membrane or GDL substrates. (Ultrasonic Systems Inc.)

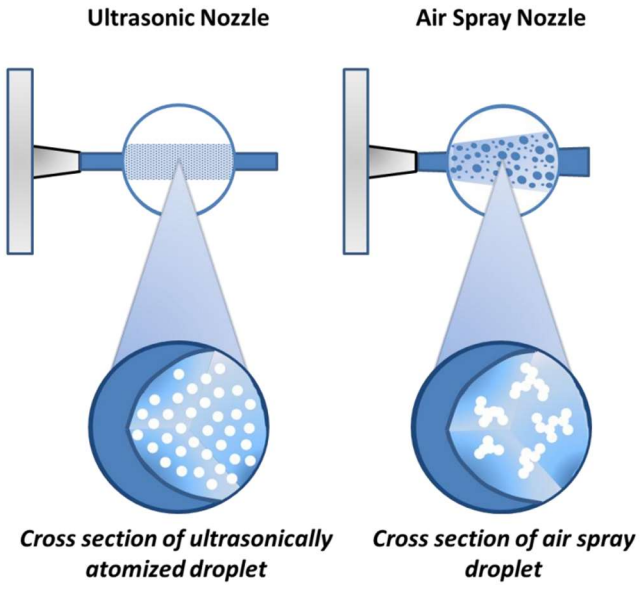

Figure 25: Comparison of ultrasonic coating to air spray coating (Pollet , 2010)

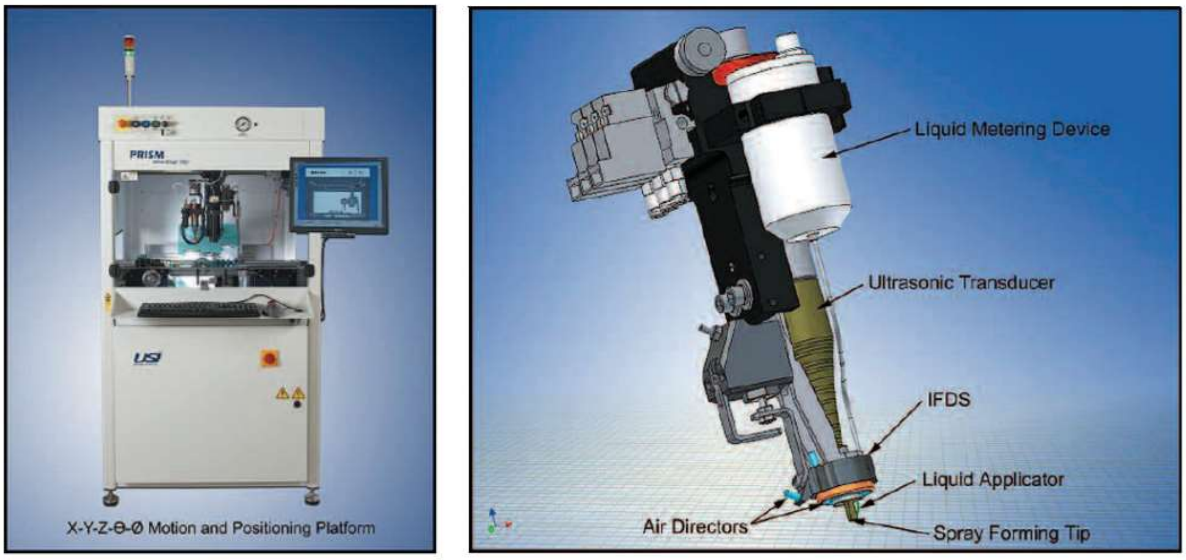

Figure 26: a) Prism 300 Coater b) Spray Head (Erickson, 2007)

The ink is sent to the head at a controlled flow by means of a positive displacement metering pump. In the head, the ink is sent directly to the atomising surface of the spray forming tip, from which it is expanded and accelerated by an adjustable velocity air stream. This prevents the drops from coalescing and forming larger drops which affects the layer quality of MEAs produced. (Ultrasonic Systems Inc. ; Erickson, 2007)

Table 5 *and* Table 6 below describes the MEAs that were sprayed for the method development and QC test evaluation in the study. The 3 layer MEAs (or CCMs) were then assembled into 5 layer MEAs by gasketing with a pair of 32 um PET at 90°C and 2300 lbs for 1 minute. The 5 layer MEAs are then assembled into 7 layer MEAs by attaching the GDL to the 5 layer MEA and cutting the final gasket to fit the test fixtures.

Table 5: Summary of CCMs prepared for method development work

Equipment	Purpose / Type	Cathode Loading (mg/cm^2)	Anode Loading (mg/cm^2)	Active Area (cm^2)	Substrate
IRT	Half CCMs	0.40	n/a	280	Confidential
	Full CCMs	0.40	0.20	280	Confidential
XRF	Substrate Variation	0.40	n/a	25	Mylar, N115, N212, NC700
	Catalyst Variation	0.05 – 0.50	n/a	9	Mylar
	Ionomer Variation	0.05 – 0.50	n/a	9	Mylar
	Calibration via stacking	0.02	n/a	80	NC700
	Calibration via top-up	0.05 – 0.50	n/a	25	NC700
	Cathode calibration via top-up	0.02 – 1.30	n/a	9	NC700
	Cathode & Anode calibration via top-up	0.06 – 0.80	0.06 – 0.80	9	NC700
	Cathode calibration for high volume coating	0.04 – 0.44	n/a	7	NC700
	High Volume Line	0.50	n/a	840	Mylar, NC700

Table 6: Summary of sample MEAs prepared for QC investigation (QC Acronyms: GA – Gravimetric Analysis, TA – Thickness Analysis, VI – Visual Inspection, OMI – Optical Microscopy Inspection, SEMA – Scanning Electron Microscopy Analysis, XRFS – X-ray Fluorescence Spectroscopy, IXRFS – Intensive XRFS, IRT – Infrared Thermography, SSPC – Single Cell Performance Characterisation.

Sample Set	Purpose	Cathode Loading (mg/cm^2)	Anode Loading (mg/cm^2)	Active Area (cm^2)	Membrane	Quality Control Analysis Sequence
1	Typical and non-destructive QC measures	0.40	0.20	25	NC700	GA → TA → VI → OMI → SEMA
2	XRF QC	0.40	0.20	25	NC700	GA → TA → VI → OMI → XRFS → SEMA
3	XRF QC	0.40	0.20	25	NC700	GA → TA → VI → OMI → XRFS → SCPC → SEMA
4 / 4R	Benchmark for performance characterisation	0.40	0.20	25	NC700	GA → TA → VI → OMI → SCPC → SEMA
5	IRT QC	0.40	0.20	25	NC700	GA → TA → VI → OMI → IRT → SCPC → SEMA
6	IRT QC	0.40	0.20	25	NC700	GA → TA → VI → OMI → IRT → SEMA
7	Intensive XRF QC	0.40	0.20	25	NC700	GA → TA → VI → OMI → IXRFS → SCPC → SEMA

The results in CHAPTER VI: RESULTS & DISCUSSION will discuss sample set 7, which had undergone intensive XRF testing. These were samples that were put through 20 iterations of XRF measurements, to test if passing x-rays through the MEA multiple times would have any negative effects on the chemical nature of the MEA.

4.2. Apparatus And Experimental Methods for Quality Control Techniques

4.2.1. Thickness Analysis

To perform the thickness analysis a digital micrometre, Mitutoyo ID-C112X Digimatic Indicator, was used. The indicator is able to measure a thickness of up to 127 µm with an error of ±1 µm. (Mitutoyo, 2022)

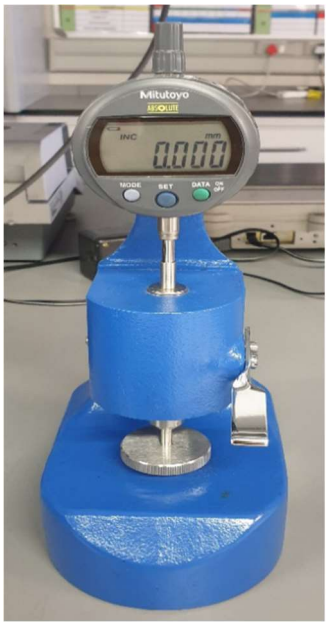

Figure 27: Digital Micrometre - Mitutoyo ID-C112X Digimatic Indicator

Table 7 summarises the thickness data that was considered for this study, explains how they were obtained and reports an industry benchmark of expected thicknesses relative to specific loadings. The thickness measurement was not used to determine the PGM loading but rather was used to cross check that the loading achieved from the weight analysis had a thickness in the range of the targeted loading.

Table 7: Thickness Measurements

Thickness Measurement Type	Obtaining Measurement	Targeted PGM Loading (mg/cm^2)	Industry Benchmark for Thickness
Membrane	Remove cover films and backer films prior to taking measurement	N/A	See specifications in Table 4.
Cathode CL	The membrane thickness will be subtracted from the thickness taken after coating the cathode CL	0.4	The average thickness ranges between 25-30 µm for a loading of 0.4 mg/cm^2 according to internal and commercial standards.
Anode CL	The thickness taken after coating the cathode CL (cathode CL + membrane thickness) will be subtracted from the thickness taken after coating the anode CL	0.2	The average thickness ranges between 15-20 µm for a loading of 0.2 mg/cm^2 according to internal and commercial standards.

4.2.2. Gravimetric Analysis

To perform the gravimetric analysis an analytical balance, Mettler Toledo XS104, was used. The balance is capable of weighting up to 120 g with a ±0.1 mg error and 0.07 mg repeatability. (Mettler Toledo, n.d.)

Figure 28: Analytical Balance - Mettler Toledo XS104 (Mettler Toledo, n.d.)

The scale was used with a weighting boat for smaller samples and within an enclosed chamber (using the undercounter weighting function) for larger samples.

The PGM loading was calculated using the weights as per the equations below:

Equation 5:

$$M_{net} = M_{final} - M_{initial}$$

$$where\ M_{initial}\ is\ the\ weight\ (g) of\ the\ substrate\ prior\ to\ coating$$

$$and\ M_{final}\ is\ the\ weight\ (g)\ of\ the\ substrate\ after\ coating$$

Equation 6:

$$L = \frac{M_{net} \times F}{A \times 1000}$$

$$Where\ L\ is\ the\ PGM\ loading\ (mg/cm^2)\ of\ the\ substrate\ after\ coating,$$

$$and\ F\ is\ the\ platinum\ loading\ factor\ (equation\ 7)$$

Equation 7:

$$F = \frac{P}{100} \times \left(1 - \frac{I}{100}\right)$$

$$Where\ P\ is\ the\ PGM\ content\ (wt\%)\ and\ I\ is\ the\ Dry\ CL\ Ionomer\ content\ (wt\%)$$

4.2.3. Visual Inspection

Visual inspection is currently a human process and a technique for automated visual inspection was developed in this work (Section 5.1). Visual inspection is done to determine the layer quality by;

- Identifying potential surface defects such as cracks, scratches, debris and CL uniformity and misalignment
- Identifying through plane defects such as pinholes or light translucency

Visual inspection involves placing the MEA on an elevated glass surface with a bright light source underneath. The opacity and amount of light translucency seen by eye is then used to gauge the quality of the MEA. Uniform opacity across the MEA is linked to low PGM loading, whereas light translucency is linked to the quality of coating. To improve on the visual inspection technique, the process could be automated and ImageJ can be used to determine the light translucency .

4.2.4. Optical Microscopy Inspection

For the optical microscopy, a Wild M400 Photomacrosocpe (Figure 29) was used. It has a magnification of 2-64x and is coupled with an Axiocam software for imaging.

Figure 29: Wild M400 Photomacroscope

The optical microscopy inspection was done to determine the layer quality by;

- Identifying potential surface defects such as cracks, scratches, debris and CL uniformity and misalignment
- Identifying through plane defects such as pinholes or light translucency

The CL was inspected using a 10x magnification lens, a digital camera and lighting system. The digital camera was connected to a computer such that picture capture and analysis could be carried out. The illumination system consists of two lights attached to flexible arms which allowed for optimal contrast on the black samples investigated.

The sample was placed under the microscope lens and was focused using the adjustable stand connected to the lens. It was ensured that the sample was flat otherwise it would interfere with the focus of the microscope. The sample was then examined using the desired magnifications. The samples were divided into 9 zones (Figure 30) and each zone was studied to ensure that the full area of the sample was analysed.

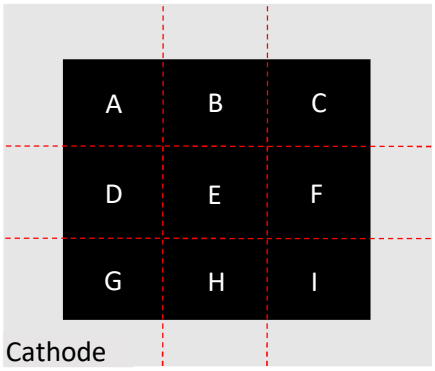

Figure 30: Depiction of zoning used for measurements

To analyse the images with ImageJ, the method that will be discussed in Section 5.1 as it was the same as the method developed for automated visual inspection.

4.2.5. Infrared Thermography

In this work, an inhouse IRT rig was engineered by building a wooden box and fitting it with a pre-developed test fixture (the nature of which is confidential), an IR camera, gas lines and lighting.

A FLIR ONE Pro IRT camera coupled with a smartphone (Figure 31) was used. The FLIR ONE Pro camera has a 19 200 pixel resolution and enhanced image clarity, is able to measure temperature up to 400°C and has a thermal sensitivity of 70mK (FLIR, 2021).

Figure 31: FLIR ONE Pro Camera Setup (FLIR, 2021)

4.2.6. XRF Spectroscopy

An Olympus Vanta XRF analyser coupled with a Vanta field stand was used in this study (Figure 32). The XRF analyser is portable and allows for fast and precise identification and analysis of elements (Olympus, 2018).

Figure 32: Olympus Vanta XRF Analyser

4.2.7. Single Cell Performance Characterisation

A FuelCon Evaluator C50-LT test station with FuelCon TestWork® software and a Baltic test fixture was used for testing. The details of the fixture are listed in Table 8. The test station is equipped with humidification control, electronic flow control, temperature and pressure control, nitrogen purge and electronic load management that is coupled with SQL data logging. The feed gases used are H_2, N_2 and synthetic air. Figure 33 and Figure 34 below provides a schematic of the test station setup that was used for performance characterisation.

Table 8: Test Fixture Specifications

Manufacturer	Baltic Fuel Cells
Model	cF 25/100 LT V1.1
Active Area	25 cm^2
Flow Field Material	Graphite Composite
Flow Field Geometry	5-fold mixed serpentine
Flow Field Sealing	O-ring
Flow Field Configuration	Parallel Channels
Flow Field Channel Width and Depth	1 mm

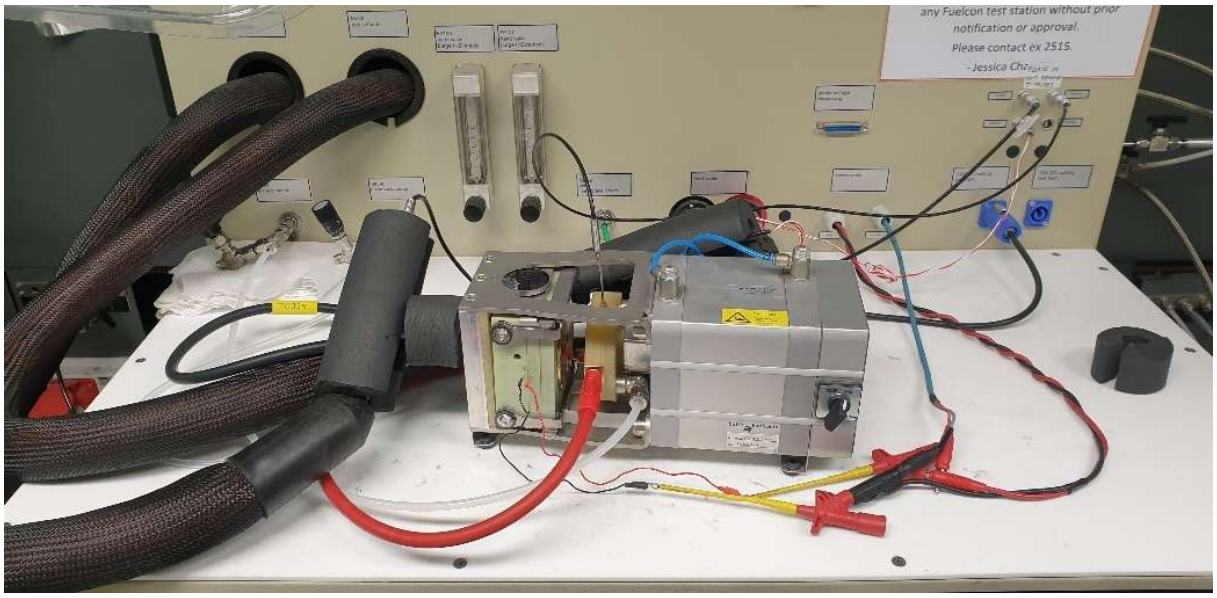

Figure 33: Fixture setup for performance characterisation

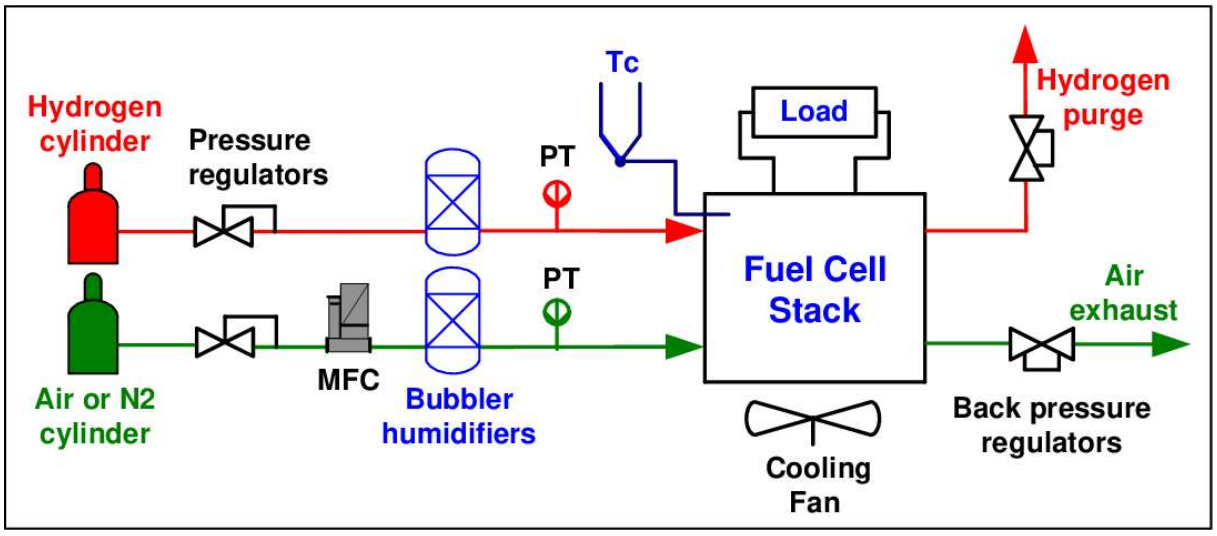

Figure 34: Schematic of the fuel cell system used for performance characterisation (Migliardini & Corbo, 2013)

The cell conditions, shown in Table 9Table 10, were used in accordance with HySA internal protocols.

Table 9: Cell Conditions used for Single Cell Performance Characterisation (APPENDIX G: Single Cell Performance Testing).

Test Parameter		Units
Active Area	25.00	cm^2
Anode Bubbler Temperature	77.50 (80% RH)	°C
Cathode Bubbler Temperature	77.50 (80% RH)	°C
Anode Line Temperature	78.5	°C
Cathode Line Temperature	78.5	°C
Anode Back Pressure	2.00	Bar
Cathode Back Pressure	2.00	Bar
Cell Temperature	80.00	°C
Anode Stoichiometry	4.00	-
Cathode Stoichiometry	4.00	-
Anode minimum flowrate	1.11	NL/min
Cathode minimum flowrate	2.65	NL/min
Fixture Pressure	4.8	bar
No. of conditioning cycles	12	-
No. of pol curves	3	-

At the start of the test the cell was automatically compressed by applying a pressure of 0.25 bar, thereafter the pressure was increased to 4.8 bar in increments of 0.05 bar. Once compressed, N_2 was purged for 25 minutes whilst setting the cell conditions before conditioning. The MEAs were conditioned 12 times by oscillating a voltage cycle between OCV and 0.3 V (which corresponds to the maximum current density). Thereafter, 3 polarisation curves were done at a stab of 0.5 and are split into a low load density region and a high load density region, allowing smaller load steps to be taken at low load densities and larger ones at higher load densities (and vice versa). EIS was done to understand the dynamic response and status of individual components of the cell using the built-in TrueData-EIS on the Fuel-Con, which has a maximum DC current of 1000 A and a frequency range between 200 uHz to 100 kHz. The data was recorded by sweeping the AC frequencies over the range of 20 kHz to 0.1 Hz at 0.02 A/cm2 to determine the charge transfer resistances and ohmic resistances.

4.2.8. SEM Analysis

A NovaNano FEI 230 SEM-EDS unit (Figure 35) was used as a tool for surface topography characterization and for cross-sectional inspection of the MEA – both of which required special sample prep. Two detectors are used, an Everhart Thornley detector (ETD) and a low-voltage high-contrast detector (vCD). The ETD makes use of side scattered secondary electrons to obtain a topographical image and the vCD highlights components of different densities.

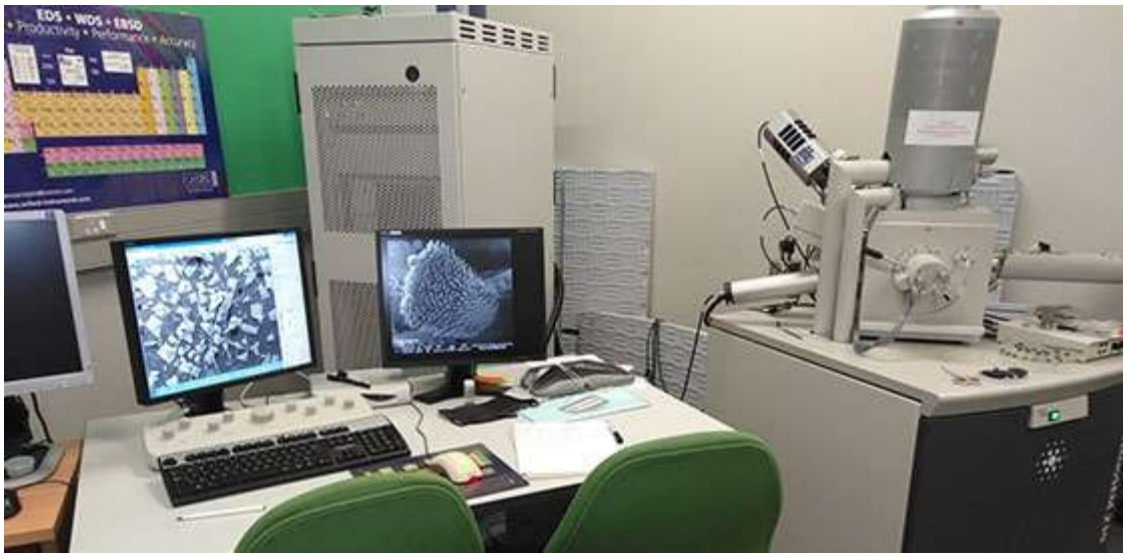

Figure 35: NovaNano FEI 230 SEM-EDS unit

Table 10 describe the sample preparation process that was used in this work to prepare samples for surface imaging. The sample pucks for surface analysis were placed into the SEM (Figure 36) and 4-8 images were taken per sample depending on the condition of the sample, the presence of features and at different magnifications.

Table 10: Sample preparation for surface inspection with SEM, developed by HySA Catalysis (Mawungwe, Submitted in February 2023)

Apparatus required	▪ Pucks (1 per sample) ▪ Carbon two-way tape ▪ Tweezer ▪ CCM/MEA samples
Step 1: Sample cutting	Cut samples into square/rectangular pieces which will fit on the puck.
Step 2: Puck prep	Place a piece of tape (big enough for the sample) on the puck.
Step 3: Sample depositing	Use the tweezer to peel away the cover film from the tape and place the sample onto the tape, with the CL or electrode being studied facing up.
Step 4: Sample marking	If there is a specific area of interest being looked at, use the tweezer to make a mark (in the form of a scratch) as close to the area of interest as possible. This will make it easier to locate the point of interest when looking through the microscope.
Step 5: Sample storage	Store prepped samples in a puck holder until they are loaded into the microscope.

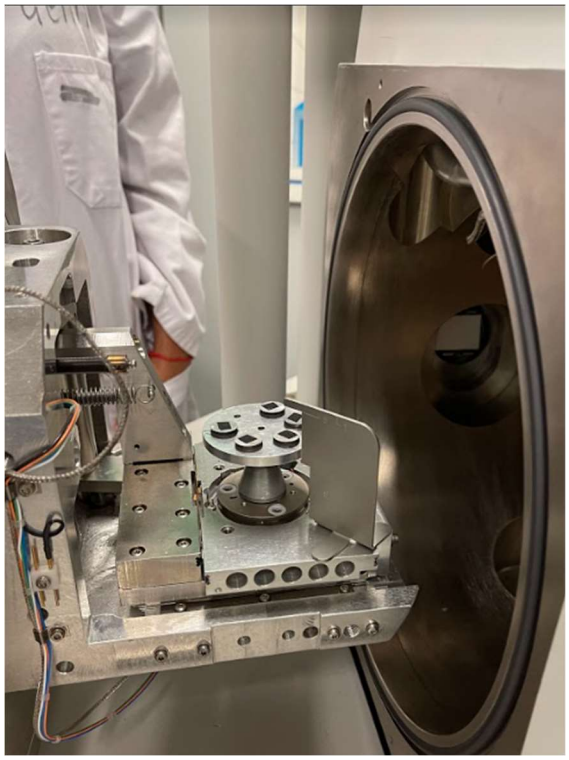

Figure 36: SEM Unit used for surface imaging

To analyse the images taken by SEM with respect to the light translucency, pinholes sizes and size and extent of debris or defects, the method depicted in Figure 37 was used.

Convert image to 8-bit	Open recorded image and click "image">"type">"8-bit" in the ImageJ bar.
Set scale	Draw a straight line over the scale bar, using the "shift" key to keep the line straight. Click "analyse">"set scale" in the ImageJ bar and then enter known distance and units.
Measuring lengths	Draw a line, click "analyse" and hold down "ctrl+m". To analyse measurements, click "results">"summarise".
Measuring area for pinhole sizes or light passing through	Select area to be analysed and click "image">"duplicate". Then click "image">"adjust">"threshold" and set default to red. Use slider to select features of interest and click "apply". Go to "analyse">"analyse particles" and ensure the boxes are ticked for "display results", "clear results" and "add to manager". Set the size to "0-infinity", the cicularity to "0.00-1.00" and enable "show outlines". Click on "results">"summarise".

Figure 37: Procedure for analysing surface images using ImageJ

For the sample preparation for cross-sectional imaging, a procedure developed by HySA catalysis (Mawungwe, Submitted in February 2023) was used. The samples were cut into 2 cm^2 strips and stacked as shown (Figure 38). They were then embedded in resin using mounting cups (Figure 38) and cured. It was then polished and carbon coated to obtain the prepared sample shown in Figure 39.

Figure 38: Stacked and clipped sample prior to embedding (left) and mounting cup with samples (right)

Figure 39: Polished, carbon coated puck

The resin pucks for cross sectional analysis were placed into the SEM Unit (Figure 40), and 4-8 images were captured per sample depending on the condition of the sample, the presence of features and at different magnifications.

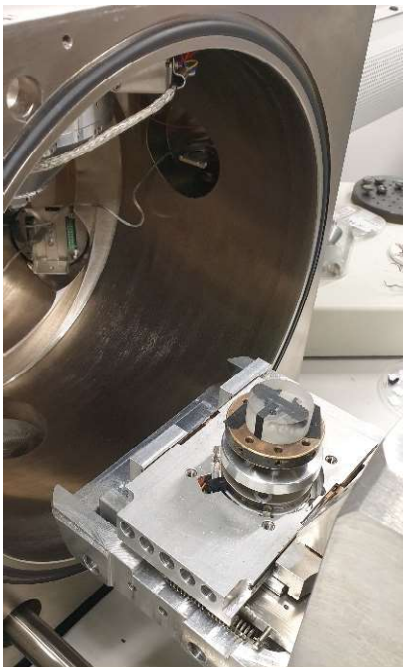

Figure 40: SEM Unit for Cross-sectional imaging

To analyse the images taken by SEM with respect to the CL thickness, the method depicted in Figure 41 that was developed by *HySA Catalysis* was used.

Image Import	Import SEM image to ImageJ
Set scale	Draw a straight line over the scale bar, using the "shift" key to keep the line straight. Click "analyse">"set scale" in the ImageJ bar and enter known distance and units.
Area of Interest	Crop the area of of interest. Select "shape function", select area and press "Ctrl + Shift + X".
Convert to Binary	Smooth the image using "Ctrl + Shift + S" in 5 repeats. Then make the image binary - click "process">"binary">"make binary" in the ImageJ bar.
Fill holes, Find Edges & Skeletonise	To fill the holes - click "process">'binary">"fill holes" To find edges - click "process">"find edges" To skeletonise - click "process">"binary">"skeletonise".
Export X-Y Coordinates	Click "analayse">"tools">"save X-Y coordinates" in the ImageJ bar
Analyse Data	Sort the X values in ascending order, find the non-overlapping Y value, calculate ΔY (catalyst layer thickness) and convert from pixels to µm.

Figure 41: Procedure for analysing cross-sectional images using ImageJ, developed by HySA Catalysis

CHAPTER V: METHOD DEVELOPMENT

This chapter covers the method development that was done for automated visual inspection, IRT and XRF. The MEA sample sets referred to in this chapter were described in detail in Table 5 *Section 4.1.3. Some of data for the work done in this section can be found in APPENDIX C: Visual Inspection, APPENDIX E: XRF Spectroscopy and APPENDIX F: IRT. All other data can be seen upon request.*

5.1. Automated Visual Inspection

5.1.1. Apparatus and Rig

The human eye has many features that are similar to a digital camera, using a lens with features that are equivalent to the human eye would therefore allow for the visual inspection method to be automated. A human eye has the following properties (Mitchell, n.d.):

- A nominal focal length of 22 mm
- A maximum aperture of 2.1-3.8
- A resolution of 576 megapixels
- An ISO ranging from 1 in bright light to 800 in dim light
- A shutter speed of 0.005-0.010

The lens closest to the human eye is a 50 mm prime lens with an aperture of 2.1-3.8 mounted on a full frame camera or a 35 mm prime lens mounted on a APS-C crop frame camera. The angle of view created by the former lens is almost identical to the human eye. To perform the visual inspection a rig was set up using LED lights, tempered glass and a full frame DSLR camera with a 50 mm prime lens attached to a stand (Figure 42) . The DSLR was therefore set to capture the same details and magnification as would be seen by the naked eye. (Mitchell, n.d.; Shutter Release World , n.d.; Cambridge in Colour , n.d.)

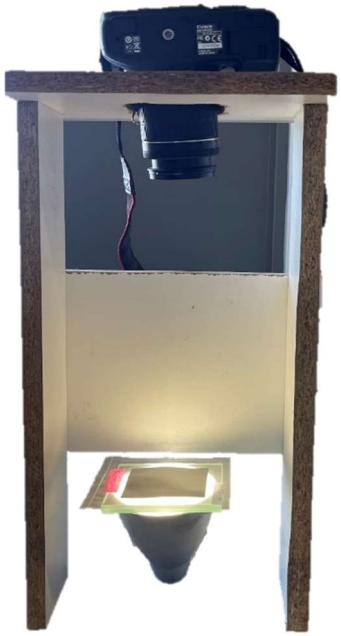

Figure 42: Experimental Setup for Visual Inspection Rig

5.1.2. Capturing and Processing Images

Visual inspection involves placing the MEA on an elevated glass surface with a bright light source underneath. The opacity and amount of light translucency seen by eye is then used to gauge the quality of the MEA. Uniform opacity across the MEA is linked to low PGM loading, whereas light translucency is linked to the quality of coating. To improve on the visual inspection technique, the process of digitising visual inspection was developed in this work and is a step towards automating the process. ImageJ was then used to determine the light translucency according to the process outlined in Figure 43.

Convert image to 8-bit	Open recorded image and click "image">"type">"8-bit" in the ImageJ bar.
Set scale	Draw a straight line over the scale bar, using the "shift" key to keep the line straight. Click analyse, set scale and enter known distance and units.
Measuring lengths	Draw a line, click analyse and hold down "ctrl+m". To analyse measurements, click results and summarise.
Measuring area for pinhole sizes or light passing through	Select area to be analysed and click image, duplicate. Go to image, adjust, threshold and set default to red. Use slider to select features of interest and click apply. Go to analyse, analyse particles and ensure the boxes are ticked for display results, clear results and add to manager. Set the size to "0-infinity", the cicularity to "0.00-1.00" and enable "show outlines". Click on results and summarise.

Figure 43: Procedure for analysing visual inspection images using ImageJ

To calculate the light translucency, the following equation was used:

Equation 8

$$Percentage\ of\ light\ passing\ through = \frac{Sum\ of\ areas\ of\ light}{Total\ area\ analysed}$$

It is envisioned that for future work, a Gen II setup for automated visual inspection can be developed that retrofits the digitised system to a manufacturing line for inline quality control.

5.2. Infrared Thermography

Having the ability to identify pinholes on a manufacturing line is vital as they are known to cause sudden failure by allowing reactant gas crossover. Therefore, pinholes are of the highest priority and

highest severity defects that can lead to performance losses, combustion of H_2, increased stresses and electrode short-circuiting. IRT provides a means of identifying pinholes and is an invaluable test. (Weber , 2008)

5.2.1. Apparatus and Rig

Wood was used to construct the box to allow for flexibility during the build and to ease post-design alterations. It was built at dimensions based on the predeveloped test fixture. The fixture was designed to photograph a part that is at least 50 cm in length and 20 cm wide. The test fixture was designed to have a clamping mechanism to create a gas-tight chamber on one side of the MEA. The fixture needed to allow for the flow of gases through an inlet and outlet port in the chamber area. Furthermore, the fixture needed to contain a surface that will allow an even distribution of gases to be exposed to the MEA. Specific details on the fixture are confidential and may not be disclosed in this work.

It was necessary to build a box for the test fixture and camera to go into as the camera picks up heat signatures that are reflected off specific materials, thus to alleviate any heat reflections, the box would fully enclose the test fixture creating a dark environmental chamber and the only openings in the box would be for the camera, the gas inlets/outlets and the light connection. The box height was determined by the length and width of the area that the camera could see as the camera would be placed in the roof of the box. The built rig containing the fixture, lighting and camera is shown in Figure 44.

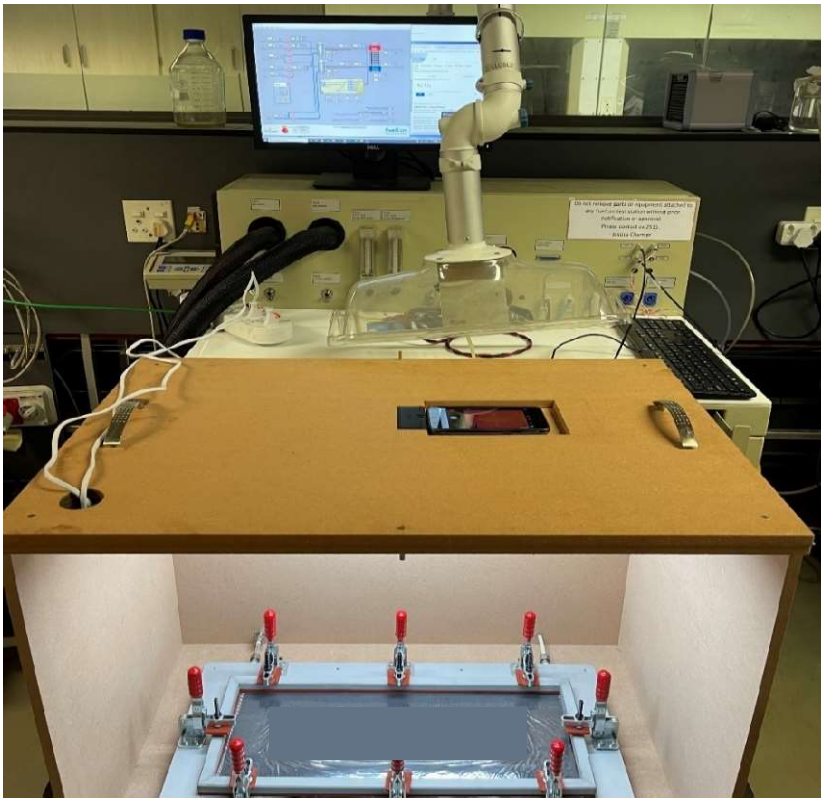

Figure 44: Inhouse IRT Rig

5.2.2. Experimental Procedure

The method development for the IRT rig followed the procedure outlined in Figure 45. The work done by *Prasad (2019)* and *Phillips et al. (2018)* was used as a starting point, especially in formulating a safe / non-hazardous ratio for a gaseous blend of H_2, Nitrogen and potentially Oxygen. The blend suggested by *Prasad (2019)* is 20% H_2 and 80% N_2 – furthermore, it is suggested that the anode be exposed to the gaseous blend and the cathode be exposed to air. The blend suggested by *Phillips et al. (2018)* is a flowrate of 0.2/0.2 std.L/min of H_2/N_2 on the anode for 15 minutes prior to exposing the cathode to air, thereafter, reducing the flowrate to 0.01/0.00 std.L/min and exposing the cathode to air. *Phillips et al. (2018)* further suggests using low flowrates and a detached anode outlet to minimise the pressure drop between the two electrodes and prevent the MEA from bulging.

Determine N_2 flowrate	Vary between 10-30 NL/min in steps of 5 NL/min. 10 NL/min is the minimum stable flowrate that the equipment can apply and 30 is the standard inhouse flow rate for operating the equipment for all tests.
Determine Back Pressure	Vary between 1-2 bar in steps of 0.1 bar. 1 bar is the minimum back pressure that the equipment can apply and 2 bar is the standard inhouse back pressure for operating the equipment for all tests.
Determine H_2 flowrate and H_2:N_2 ratio	Vary the flowrate between 0.04 and 6.00 NL/min. 0.04 NL/min is the minimum flowrate that the equipment can apply and 6 NL/min is at a 1:4 ratio as suggested by *Prasad et. al (2018).*
Determine purge conditions	Vary the time for pre and post purge - 5, 15, 30, 60, 120, 180 minutes. Inhouse purge conditions for performance characterisation of MEAs are 15-30 min.
Assess effect of gasket border overlapping CCM	Vary border overlap - 1, 3, 5, 7 and 10 mm. Where 1 mm is the minimum and 10 mm is the maximum overlap generally used inhouse and in commercial manufacturing.
Assess effect of single electrode versus double electrode	Test single coated electrode parts with coated area exposed to air or exposed to the N_2:H_2 blend and test test dual coated electrode parts with the anode exposed to air or exposed to the N_2:H_2 blend.
Assess effect of varying active area dimensions	Test a 25 and a 250 cm^2 part and compare the effects of increasing active area. 25 cm^2 is the general lab scale size and 250 cm^2 is in the larger range of active areas manufactured commercially.
Classify appearance of potential pinholes and defects	Puncture the MEA with different pin sizes and analyse the thermal response versus actual pinhole size. Pinehole sizes: 0.23, 0.30, 0.35, 0.45 and 0.5 mm based on the smallest pin sizes that could be obtained for this study.
Write up testing procedure	Develop a method for testing based on all the parameters manipulated above.
Defect Catalogue	Create a thermal imaging catalogue of common defects that occur during MEA fabrication.

Figure 45: Method Development for IRT

The template in Figure 46 was used as a schematic to outline MEA features on the IR images that will be shown in Sections 5.2.3, 5.2.4, 5.2.5, 5.2.6 and 5.3.3. The white outline indicates the outer perimeter of the gasket frame, the black outline indicates the CCM perimeter and the blue outline indicates the active area.

Figure 46: Template for IR MEA features; White - Outer Perimeter of Gasket Frame, Black - CCM Perimeter under Gasket Frame, Blue - AA.

5.2.3. Determining the Test Conditions

The procedure depicted in Figure 45 in the methodology section was followed to determine the test conditions to be used, the start-up/operational/shutdown procedure to be followed and the sensitivity of the test. As well as to create a thermal imaging catalogue for identifying defects and assessing whether environmental factors such as humidity or temperature would affect the results.

The test conditions obtained from literature were used as a starting basis and were adjusted according to the capabilities or limitations of the equipment used in this study. The ratio of H_2 to N_2 was chosen as 1:12.5, which is significantly lower than that of literature at 1:4 (Prasad, 2019) or 1:1 followed by pure H_2 (Phillips, Ulsh , Neyerlin, Porter, & Bender, 2018). This ratio was chosen as it allowed for defect detection and was within the safety limitations involved adhered to the lower flammability limit of H_2. When the system was run at anything equal to or higher than a 1:6.5 ratio, there were large temperature spikes and the MEA often caught alight and burnt if there was any gas crossover.

The flowrate chosen was 0.5 NL/min for N_2 and 0.04 NL/min for H_2, which was similar to the suggested literature amount of 0.6 NL/min (Phillips, Ulsh , Neyerlin, Porter, & Bender, 2018). As suggested by *Phillips et al. (2018)*, an anode open to ambient conditions was used to minimise the pressure difference on the two electrodes to prevent the MEA from bulging.

The pre and post N_2 purge times were chosen at 30 minutes and 15 minutes, respectively. This was chosen based on the presence of the H_2 front that was created when running the test – the H_2 front referred to is a moving temperature peak that crossed the sample moving from the inlet towards the outlet as the H_2 reacted with the oxygen that was present in the CL or in the chamber (Figure 47). To test the purge time required to remove majority of the oxygen from the chamber an uncoated PET film was used and resulted in a 5-minute purge time. To test the purge time required to remove majority of the oxygen present in the CL two factors were considered, i.e. the size of the active area and the loading. For the size of the active area, the purge conditions were tested at a minimum size of 25 cm^2

and a maximum size of 250 cm^2, both sizes still resulted in a H_2 front at 180 minute purge time, however, the front dissipated faster between 15-30 minutes of purging. Therefore, suggesting that the maximum amount of oxygen that could have been removed from the CL was achieved by the 30 minute mark and the pre-purge time was set at 30 minutes. For reasonability with regards to test times, the post-purge time was based on the time required to flush out the H_2 from within the chamber and was assessed by the time taken for the temperature to return to the ambient temperature prior to H_2 flow, which was achieved at 15 minutes.

For the loading, it was discovered that an increase in loading resulted in a minimal increase in purge time, however, the increase in time was between 3-5 minutes and was accounted for within the 30 minute pre-purge and 15-minute post purge times. Therefore, it was decided that the test would be done with the anode exposed to the chamber and the cathode exposed to the air as the anode generally has a thinner CL thus trapping less air. Furthermore, the anode is exposed to hydrogen and the cathode to air in fuel cell operation thus complying with operating conditions.

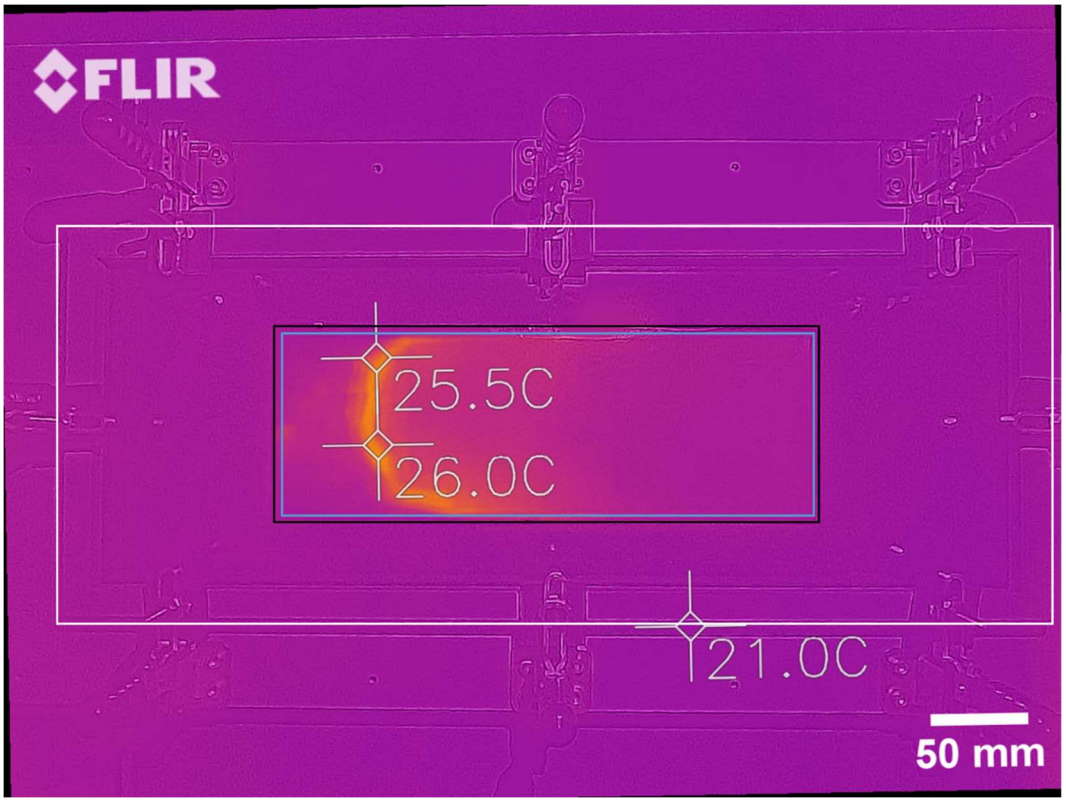

Figure 47: Depiction of H_2 Front moving across sample in IRT Test

5.2.4. Sensitivity Analysis

To assess the effect of the gasket border thickness and determine the minimum thickness needed to prevent gas crossover at the seal between the CCM and the subgasket. The test was run with half CCMs (has 1 electrode coated) and with the coated electrode exposed to air so that no temperature change would be seen due the H_2 front and only a change in temperature at a point of gas crossover would be seen. The results (Figure 48) show that the gasket border thickness from 1 mm up to 10 mm had no gas crossover and thus 1 mm can be used as the minimum overlap of the subgasket on the CCM without breaking the seal.

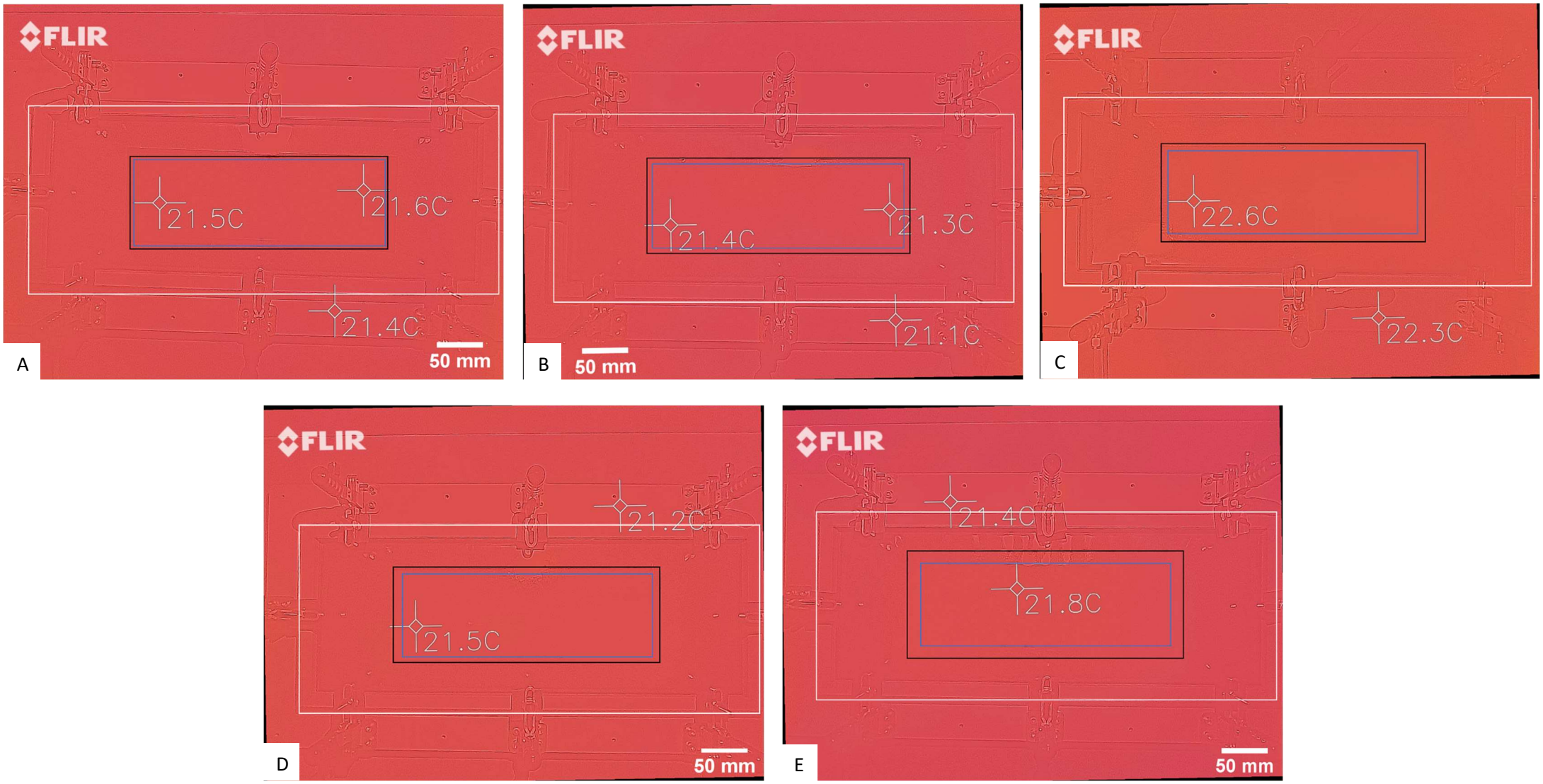

Figure 48: A - Cathode Electrode with 1 mm gasket border, B - Cathode Electrode with 3 mm gasket border, C - Cathode Electrode with 5 mm gasket border, D - Cathode Electrode with 7 mm gasket border, E- Cathode Electrode with 10 mm gasket border.

The same procedure was then repeated on full CCMs (having CL coated on both electrodes) with the anode electrode being flush coated. Therefore, the subgasket was laminated over the CL rather than on bare membrane to assess if the presence of both electrodes or if this form of gasketing would affect the conditions for testing or cause gas crossover at the seal. It was discovered that the presence of the second electrode and both forms of gasketing, i.e. on bare membrane or on the CL, had the same results (Table 11). The presence of both CL increased the time for the H_2 front to pass, adding 2-3 minutes to the test time before any defects can be identified.

Table 11: Time elapsed for H2 front to pass based on gasket-CCM frame overlap, presence of both CLs and gasketing on bare membrane versus CL

Sample	Time taken for H_2 front to pass (min)	Time taken for temperature to stabilise (min)	Stable temperature reached (°C)
Single Electrode			
1	No front	3	24.8
2	No front	2	24.2
3	No front	3	24.2
4	No front	2	24.0
5	No front	2	24.4
Double Electrode			
1	1.45	1	23.4
2	1.00	2	24.3
3	1.06	2	24.2
4	2.21	1	24.0
5	1.08	2	23.5

5.2.5. Pinhole Identification

Weber (2008), states that there is a lack in literature on the signature of a pinhole and the effect of pinhole size on performance. This work aimed to create a method for identifying pinhole sizes based on the thermal signature of a pinhole so that future work could potentially link it to performance.

To be able to identify and classify the appearance of potential pinholes, pinholes of varying size between 0.23-0.50 mm were introduced into the CCM using hyperdermic needles. The pinholes created were analysed using SEM to verify the size of the hole that was made. The SEM analysis revealed that the pinholes made were in the shape of elongated ovals (Figure 49). The length of the ovals were then measured and is tabulated in Table 12.

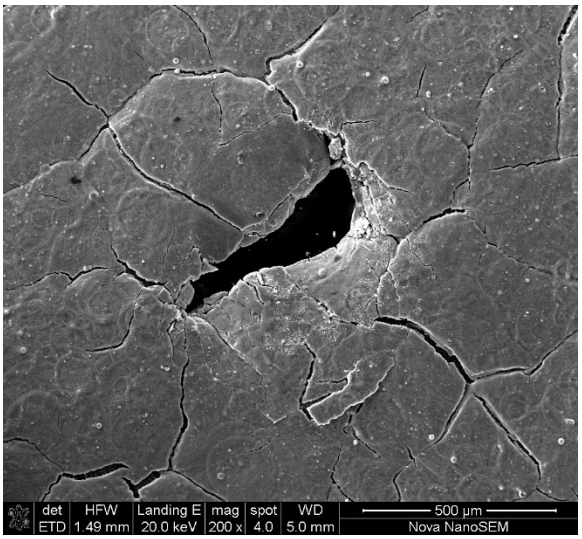

Figure 49: SEM image of pinhole created by 0.50 mm pin

Table 12: SEM Analysis of Pinhole sizes used for IRT method development (the full set of measurements for individual pinholes can be found in Appendix F)

Pin size used to create pinhole (mm)	Average size of pinhole measured using SEM imaging (mm)
0.23	0.21
0.30	0.40
0.35	0.55
0.45	0.61
0.50	0.65

Figure 50 shows that the IRT was successful in detecting pinholes of ≥0.21 mm large. However, it was unsuccessful in differentiating between a pinhole size that was 0.23 mm large to one that was 0.65 mm large. This can be seen in the image, given that the 5 pinhole sizes were punctured in order of decreasing magnitude from top to bottom but have thermal signatures which imply otherwise.

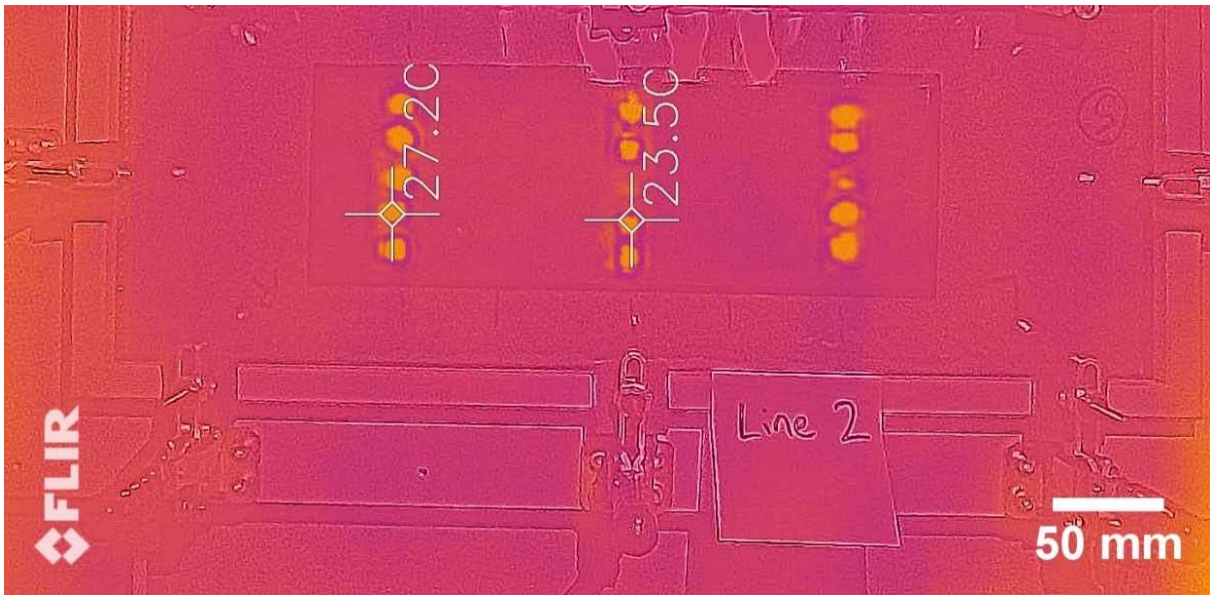

Figure 50: Thermal image of pinholes varying from 0.23 mm to 0.50 mm in diameter

5.2.6. Thermal Signatures for Typical Defects

To create an imaging catalogue of what defects might look like through the IRT test, defects such as wrinkles in the gasket and CCM and unsealed gasket borders or tears in the gasket/CCM were imaged from defects donated towards the study by a commercial line. Below are some examples of the defects that the IRT test was able to identify.

Table 13: Thermal imaging catalogue for typical defects

Type of Defect	Image of Defect	IR Response
Wrinkle in gasket frame (not connecting to AA)	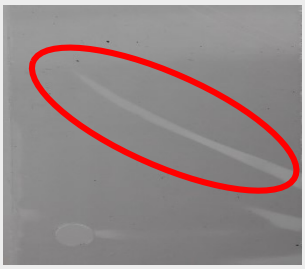	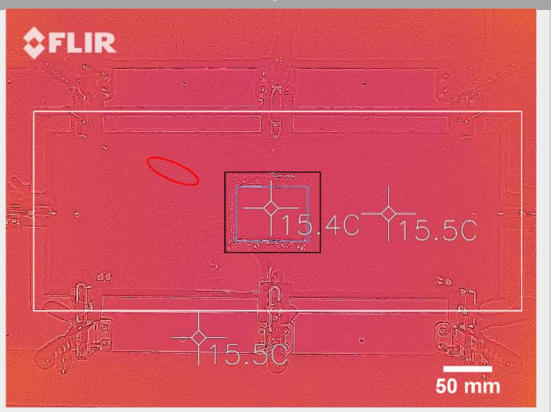
Wrinkle in gasket frame (connecting to AA)	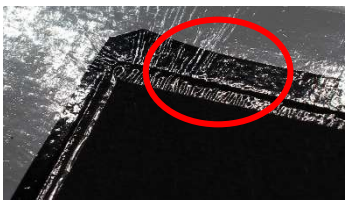	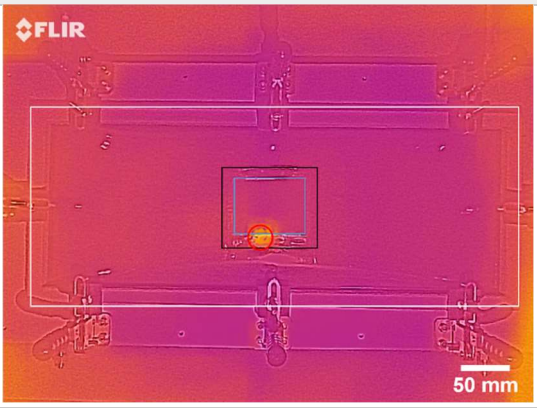
Unsealed gasket border (slow leaking gas crossover)	Not visible on MEA	

Unsealed gasket border (fast leaking gas crossover)	Not visible on MEA	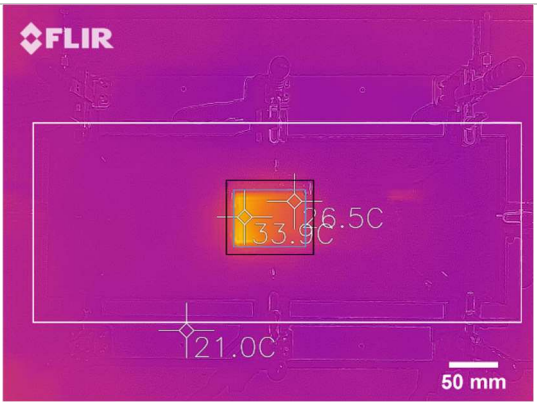
Tear in CCM	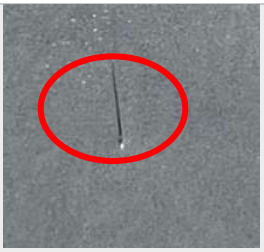	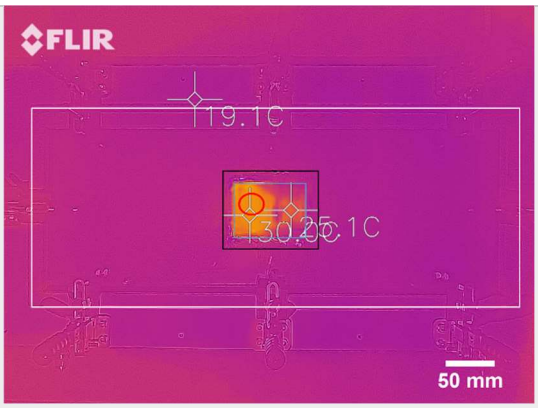
Hole in gasket frame	Not visible on MEA	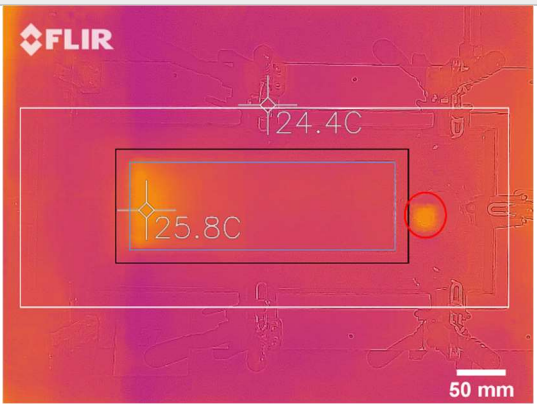

5.2.7. Incorporation into high volume line

The rig and method developed in this work could only be used for low volume production as MEAs fabricated would have to be sampled by pulling them off the main manufacturing line, running the IRT test and returning them to the line. For high volume production, a rig similar to the one demonstrated by *Bender, Felt, & Ulsh (2014)* in the literature review (Section 2.4.2.1, Figure 20) would be a better option. However, this rig was not investigated in this work due to financial limitations imposed on the study, as well as safety concerns with regards to having exposed, flowing gases in a laboratory as well as near an MEA manufacturing line.

5.3. XRF Spectroscopy

The approach for method development for the XRF spectroscopy entailed spraying samples to assess if the equipment could handle variability of the substrate, determine what environmental factors (such as temperature, humidity or time that the sample is exposed to the environment) would affect the

equipment, calibrate the equipment for platinum loading analysis and create a procedure for analysing MEAs.

To calibrate the equipment for platinum loading analysis, the following approaches were taken:

- Using a stacking method, in which a large CCM was sprayed at a specific PGM loading and cut into 3x3 cm samples. The samples were then stacked onto each other and a reading was taken each time a sample was added to the stack, thereby demonstrating an increase in the PGM loading.
- Using a top-up method, in which samples with a 3x3 cm active area were continuously topped up by a specific PGM loading and measured each time the top up was done.

To assess if the equipment could handle variability, the following parameters were manipulated:

- Membrane Thickness – Three types of membrane were used to represent the lower bound thickness, intermediate thickness and upper bound thickness generally used in MEA manufacturing to determine if the thickness of the membrane would affect the reading.
- Sample Orientation – Readings were taken with the catalyst coated side (for single electrode samples) facing the eye of the XRF or facing away from the eye of the XRF to determine whether the sample orientation affected the reading.
- Electrode Orientation – Readings were taken for the anode being sprayed first versus the cathode being sprayed first as well as for the cathode facing the eye of the XRF or the anode facing the eye of the XRF to determine if the electrode orientation affected the reading.
- Ink formulation – MEAs that were sprayed with different ink formulations (such as varying ionomer content or varying catalyst type) were tested to determine if a single calibration curve can be used for different ink formulations.

To determine what environmental factors would affect the equipment, the following parameters were manipulated based on the factors that generally affect the gravimetric analysis:

- Temperature – The samples were analysed when the temperature of the CCM was at a high temperature versus when it was at a low temperature to see if the temperature affected the reading.
- Humidity – The samples were analysed when the humidity in the lab was high versus when it was low to see if the humidity affected the reading.
- Time exposed to environment – The samples were analysed at specific time intervals after being exposed to the environment to see if exposure to the environment affected the reading.

The method development for XRF spectroscopy is discussed in *sections 5.5.*1, the implementation of the XRF on the lab scale test MEAs are discussed in *section 5.5.*2 and the incorporation of the XRF in a high volume line is discussed in *section 5.5.3*. The experimental data for the XRF results can be found in *Appendix E*.

5.3.1. Developing a calibration method

The calibration procedure was developed, whereby two approaches to calibrating was used. The first approach involved a stacking method, in which samples were coated at an average PGM loading of 0.0673 mg/cm^2 and then stacked on top of each other in the XRF chamber to compound the loading and achieve a calibration curve for a PGM loading of 0 – 1.5 mg/cm^2.

For the stacking method, the sample was cut as shown below and the measurements were taken for each individual sample before they were stacked.

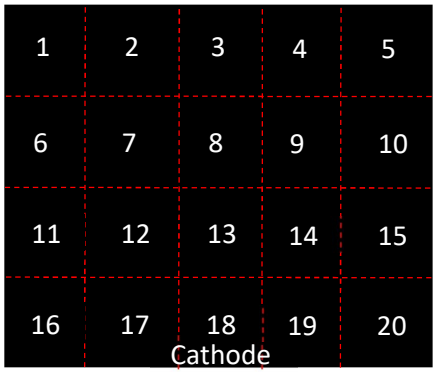

Figure 51: Depiction of sample division for stacking method

From Figure 52, it can be seen that initially the calibration curve increases linearly as would be expected due to the loadings increasing linearly. However, after the 5th sample was stacked the curve starts to plateau for the XRF readings. After the 10th sample the XRF readings plateaued and the XRF reading appeared as if it was staying constant but the gravimetric loading was increasing. After the 17th sample the curve starting dipping lower than the plateau indicating a drop in loading even though it should still be increasing. Therefore, the exponential curve obtained (Figure 53) suggests that this approach would not work and was unsuccessful. This approach could have failed due a maximum depth through which the XRF can penetrate or due to the absorption effect explained in Section 2.4.2.2 by *Brouwer (2003)* as a result of the matrix being changed. The matrix is made up of parameter changes which can potentially affect the XRF reading, such as substrate thickness, catalyst type, ionomer content and sample orientation (which will be discussed in Section 5.3.2). Therefore, in this approach the matrix is constantly being changed by including multiple layers of membranes and catalyst, as well as changing the net substrate thickness.

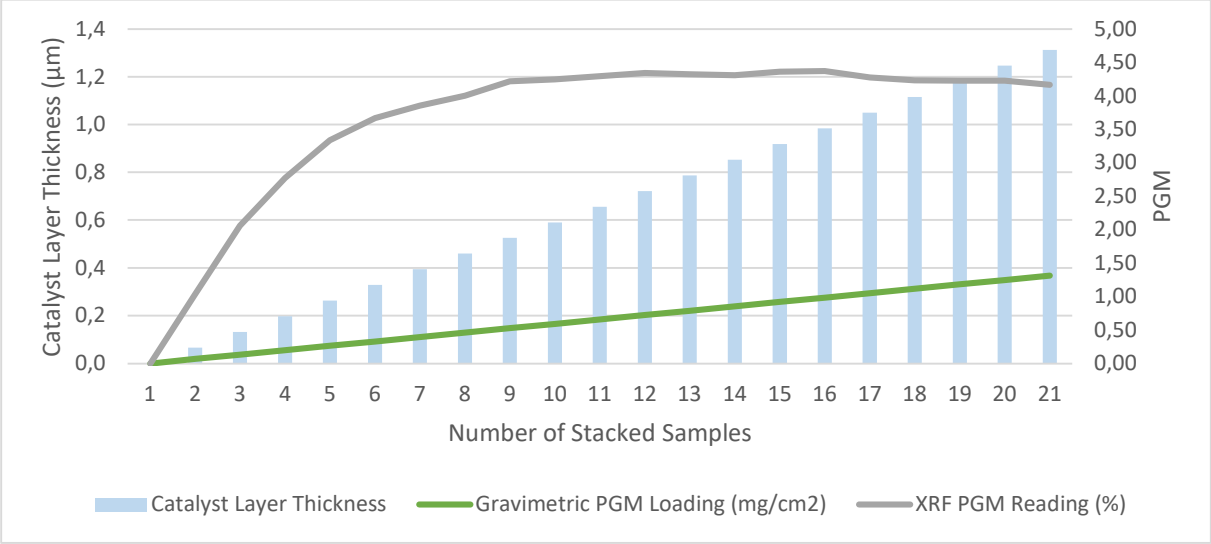

Figure 52: XRF calibration via stacking method

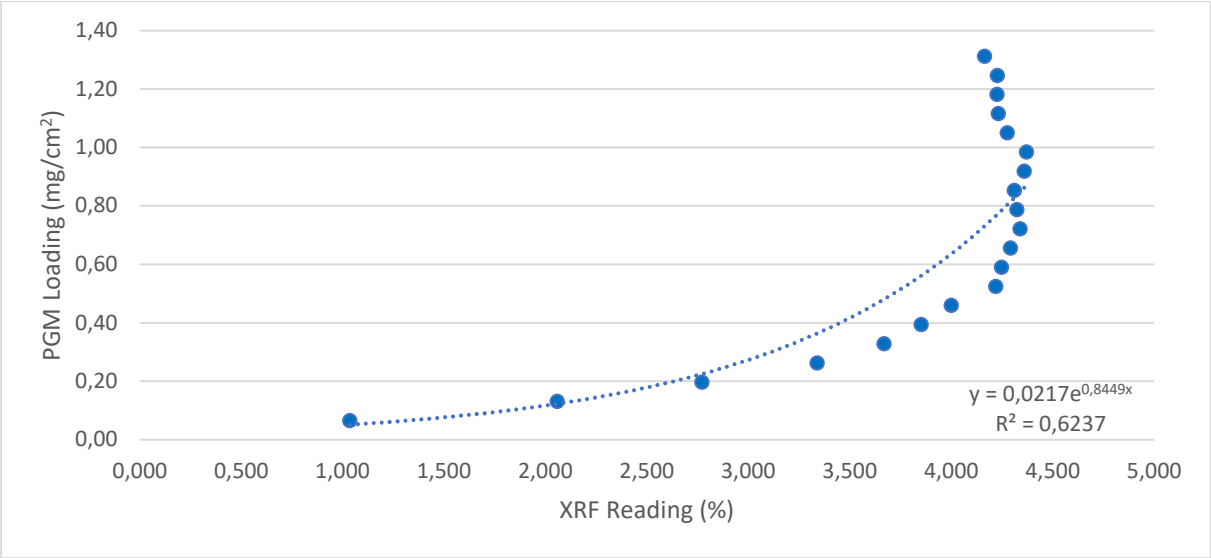

Figure 53: XRF calibration curve for stacking approach

To overcome the challenges encountered with the stacking method, a different method was evaluated. This approach is a top-up method, whereby, the same sample was coated at a PGM loading of approximately 0.05 mg/cm^2 and then topped up by approximately 0.05 mg/cm^2 after each XRF reading until 1.5 mg/cm^2 was achieved. When calibrating the equipment for the top-up method, the samples were divided into 9 zones (Figure 54) and measurements were taken at each zone to ensure that there was consistency in the coating across the sample.

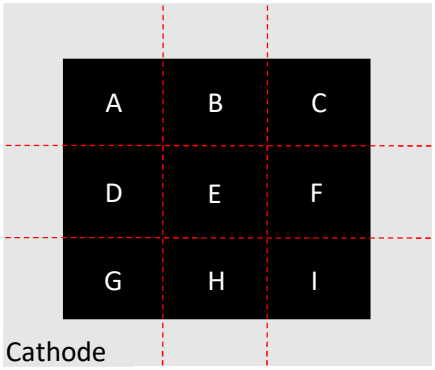

Figure 54: Depiction of zoning used for measurements

For repeatability, this was done for 3 identical samples from which the data was then averaged and the calibration curve in Figure 55 was obtained. The linear equation obtained from the calibration curve was $y = 0.0829x$ and the correlation coefficient for the data was 0.99.

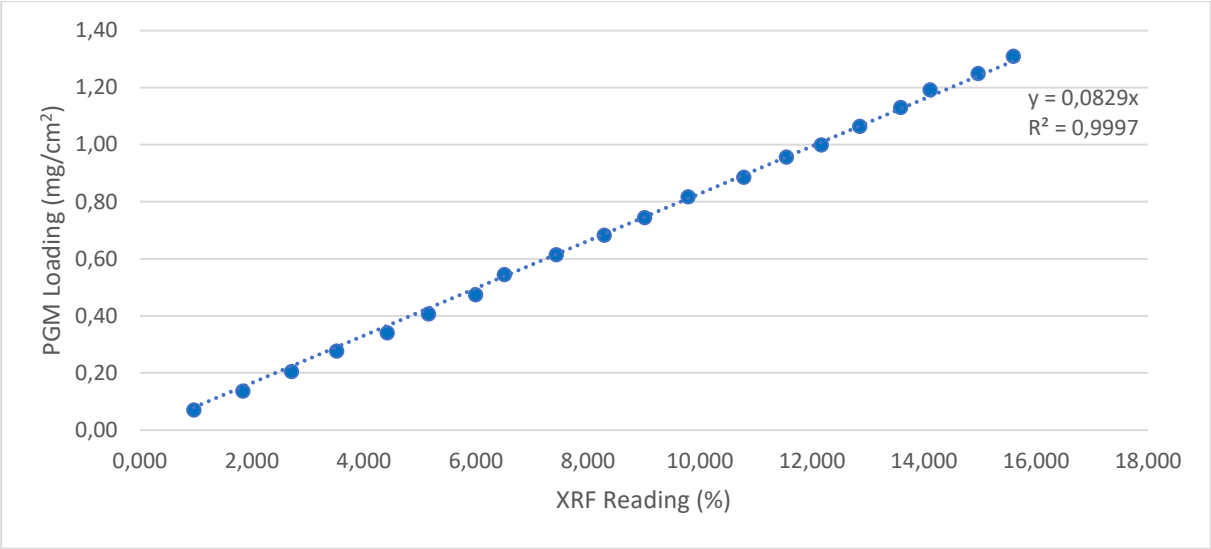

Figure 55: XRF calibration curves for top-up approach

The second approach to calibration was successful due to the matrix being kept constant. This was then expanded to a calibration for the cathode side and a calibration for the anode side, which was necessary to keep the matrix the same by keeping the sample orientation (either the cathode CL or the anode CL facing the eye of the XRF throughout calibration and testing). Figure 56 shows the calibration curves for the cathode and the anodes. Their respective equations and correlation coefficients were $y = 0.0803x$ and 0.99 for the cathode and $y = 0.0973x$ and 0.99 for the anode. The anode calibration is dependent on the cathode calibration. Therefore, the XRF reading for the cathode was subtracted from the XRF reading for the anode in determining the calibration curve.

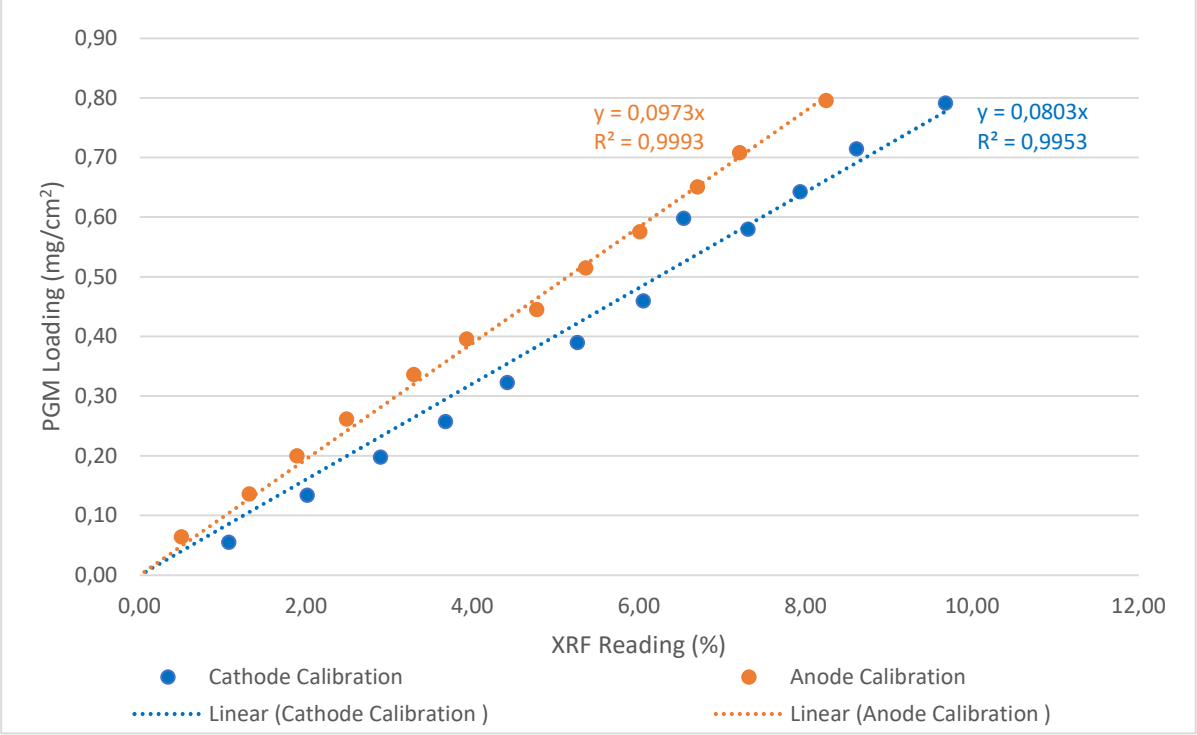

Figure 56: XRF Calibration Curves for the Anode and Cathode CLs

5.3.2. Sensitivity Analysis

XRF readings were taken to assess the sensitivity related to the substrate thickness, the sample orientation, the electrode orientation and the ink formulation. The results are shown in Figure 57, Figure 58, Figure 59 and Figure 60, respectively. From the results it can be seen that all 4 scenarios have an effect on the XRF reading, confirming that it is sensitive to and would have to be calibrated for each scenario. For the purpose of the quality control done in this work, the XRF was calibrated with no backing film present and the catalyst coated side and/or cathode facing the eye of the XRF.

To assess if the equipment could handle variability in substrate changes, 4 substrates were tested that varied in thickness and elemental composition whilst all other variables were kept constant. The 4 substrates used were mylar, N115 membrane, N212 membrane and NC700 membrane. Figure 57 depicts the XRF analysis done on the 4 types of substrates selected for the experiment, in which a loading of 0.40 $mg.cm^{-2}$ was targeted. It can be seen that the XRF gives a varying output for the different substrates. The trends observed indicate that the XRF values obtained for the N212 and the NC700 membranes share a similar offset of 0.02 $mg.cm^{-2}$ from the gravimetric analysis, whereas the mylar has an offset of 0.03 $mg.cm^{-2}$ and the N115 has an offset of 0.05 $mg.cm^{-2}$. These offsets indicate that the XRF is sensitive to the change in thickness of the substrates, where the offset increases as the thickness of the substrate increases that is potentially due to the matrix absorption effect. Therefore, it can be concluded that the XRF would need to be calibrated for the specific substrate it is being used on.

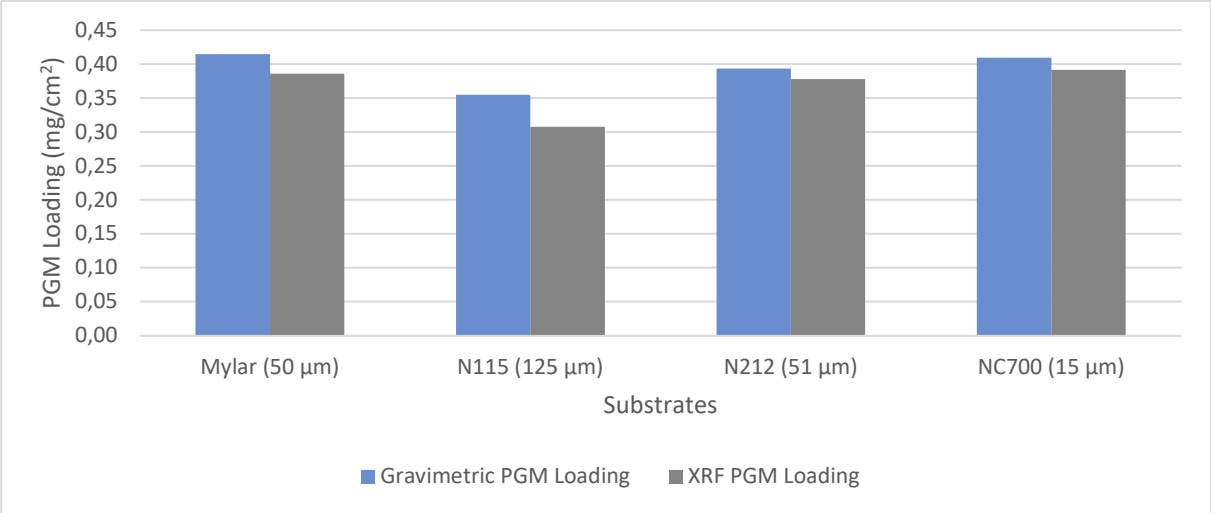

Figure 57: XRF substrate testing – Averages of Different Substrates

The sensitivity of the handheld XRF to sample orientation was evaluated by performing a calibration on the same sample when it had the CL was facing the eye of the analyser and when it had the CL facing away from (or the substrate facing) the eye of the analyser. The results are depicted in Figure 58, from which it can be seen that it is not as sensitive to this parameter. At lower loadings the curves overlap almost perfectly, however, the curves do start to deviate from each other as the loading increases.

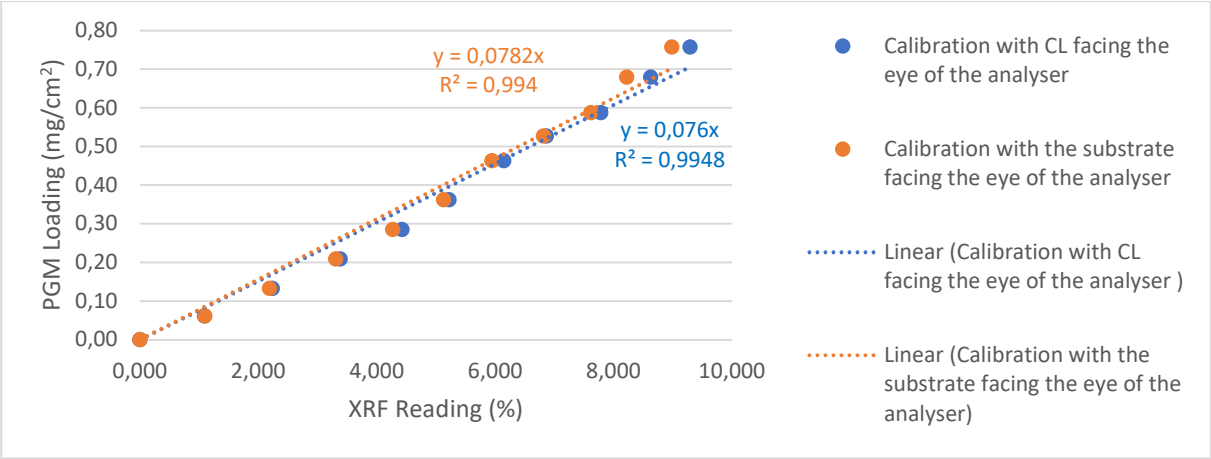

Figure 58: XRF sensitivity to sample orientation

The next steps focused on evaluating the sensitivity of the handheld XRF to changes in catalyst and ionomer content. To assess if the equipment could handle variability in ink changes, a calibration (Figure 59) was done for 2 different commercial inks in which the catalyst was the only variable being changed. Catalyst A was a 45% platinum on carbon catalyst and B was a 40 % platinum on carbon catalyst containing iridium. The calibration curve of catalyst A had a steeper gradient than catalyst B, suggesting that the XRF is sensitive to catalyst changes within the ink.

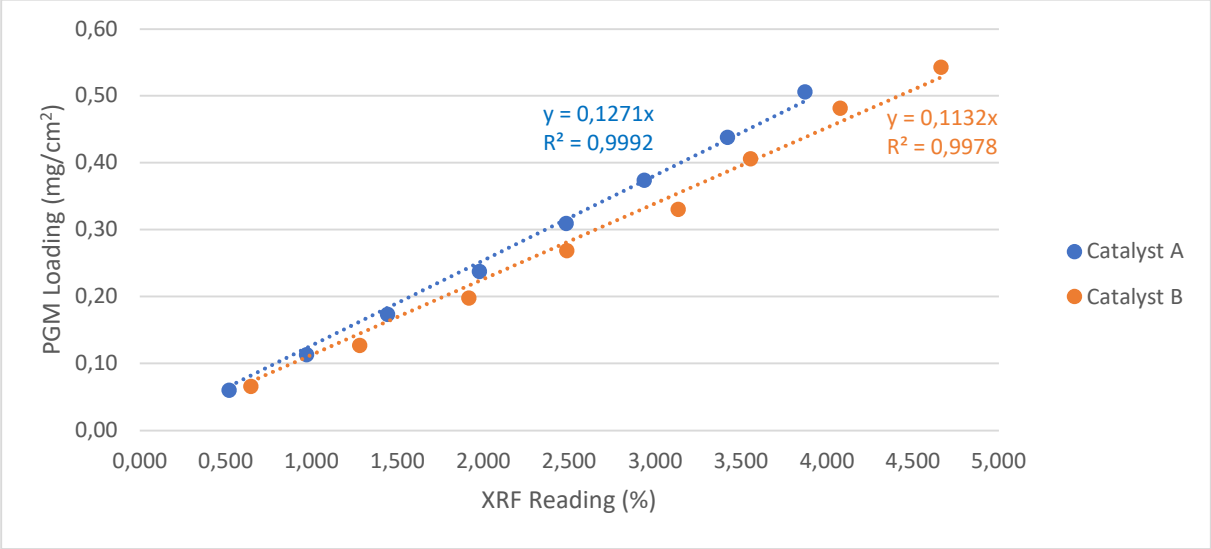

Figure 59: XRF Variability Handling - Catalyst Variation

Ionomer content changes within the ink were also tested by varying the ionomer content between 3 – 30 wt%. The results are depicted in Figure 60, which shows that the gradient of the calibration changes as the ionomer content changed. Therefore, suggesting that the XRF is sensitive to ionomer changes within the ink. However, it is more susceptible to large changes (i.e. >27%), and less susceptible to small changes (i.e. >5-15%). This is shown by the distinct difference between the curves for a 5-15% ionomer content change versus a 27% change.

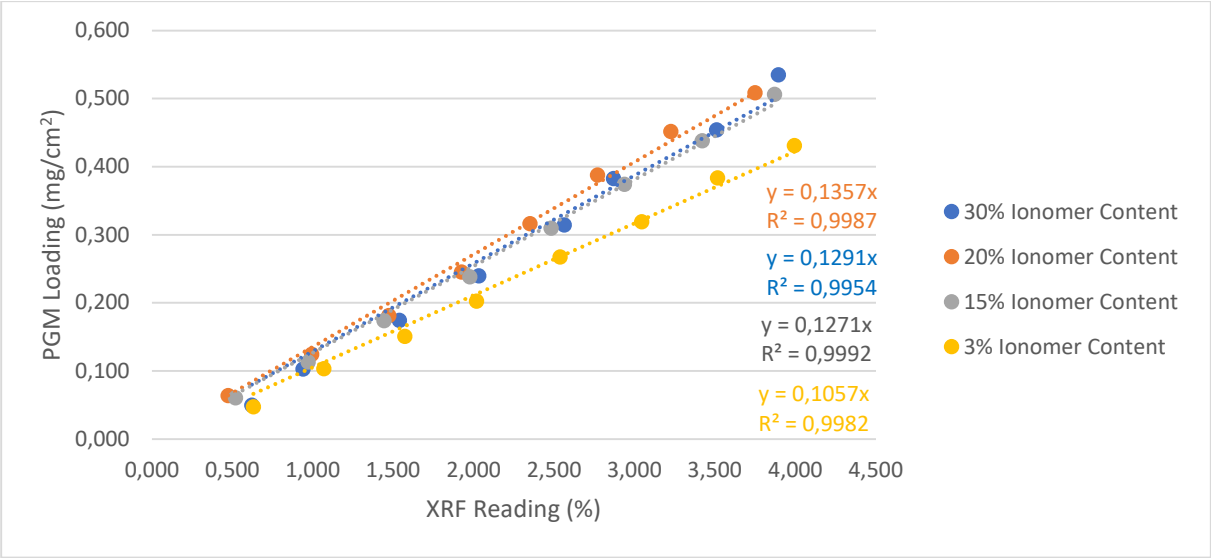

Figure 60: XRF Variability Handling - Ionomer Content Variation

5.3.3. Incorporation into high volume line

To show that the XRF can be integrated into an inline feedback loop for high volume manufacturing, the XRF was mounted onto a high volume line and calibrated. The calibration was done for 3 scenarios, i.e. when the conveyor belt was stationary and the copper plate manufactured to work with the XRF was mounted under the sample, when the conveyor belt was stationary and the stainless steel plate attached to the conveyor was being used with the XRF instead of the copper plate and lastly when the conveyor belt was moving at a speed of 1 m/min and the stainless steel plate attached to the conveyor was being used with the XRF instead of the copper plate. These 3 scenarios were tested so that the calibration obtained for the copper plate versus the stainless-steel plate could be compared to see the effect it would have on the XRF result. In the scenario where the belt was stationary, the eye of the analyser was placed flush against the MEA and when it was moving and the eye was elevated 5 mm above the MEA to check if this would have an effect on the test.

From Figure 61, it can be seen that the stainless steel yielded a much higher gradient curve confirming that if the XRF is to be used with a different refraction material, it would need to be calibrated for that material. Similarly, the calibration done on the stainless steel plate when it was stationary versus when it was moving was done to compare the effect the movement would have on the XRF results. Figure 61 further shows that the two scenarios overlap each other almost perfectly thus indicating that the XRF can successfully be incorporated into a high volume line and can track the real time loading without needing to stop the manufacturing line.

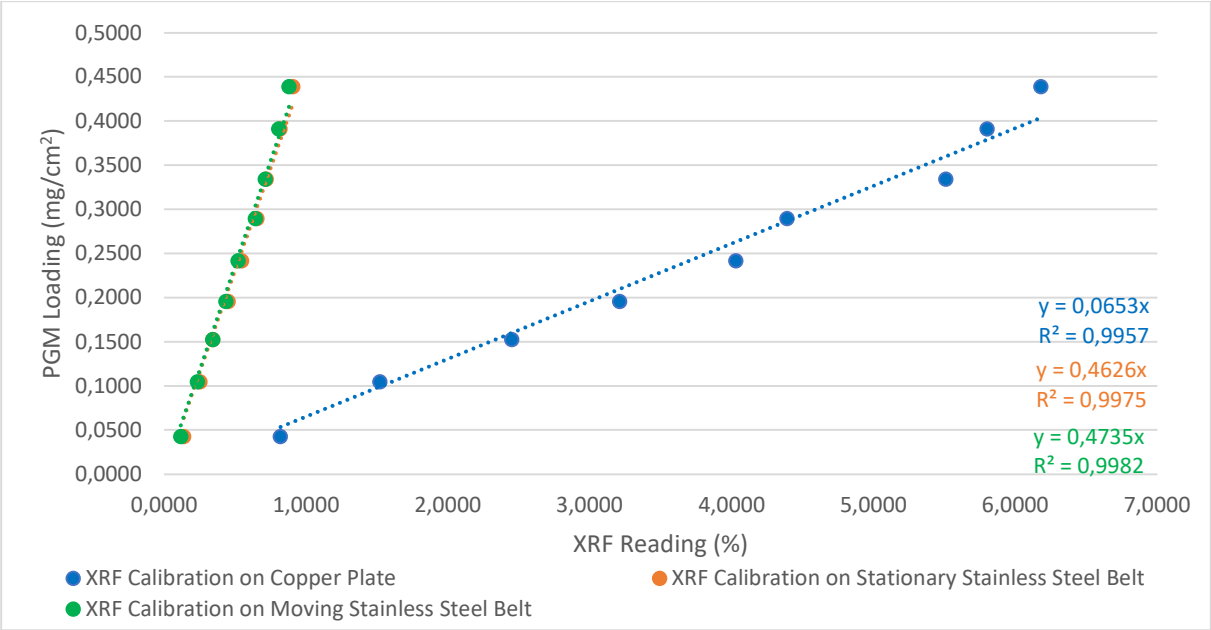

Figure 61: XRF Calibrations for high volume coating line

A high volume line was used to demonstrate the use of the XRF as an inline system. However, trying to adjust a high volume system to coat at lower volumes with minimal ink usage for the scope of this project resulted in poor CLs. In the images below, visual defects such as wrinkling, cracking and light translucency can clearly be seen. Figure 62 depicts the area in which the copper plate used for stationary XRF analysis was set up under the membrane during coating. The visual inspection identifies the permanent damage in the form of stretched areas of the membrane caused by a combination of the vacuum and the copper plate. Figure 63 depicts the area in which stationary XRF analysis was conducted without the copper plate for a comparison in quality. Figure 64 depicts different areas along which in-line XRF analysis was done to show. The comparison between the 3 figures shows that the copper plate (in its current form) is not suitable to be retrofitted to an inline test. It also showed that the inline test (with the belt in motion) can successfully be done with no negative impact on the layer quality as no significant difference in quality was seen in the visual inspection for when the belt was stationary versus when it was moving.

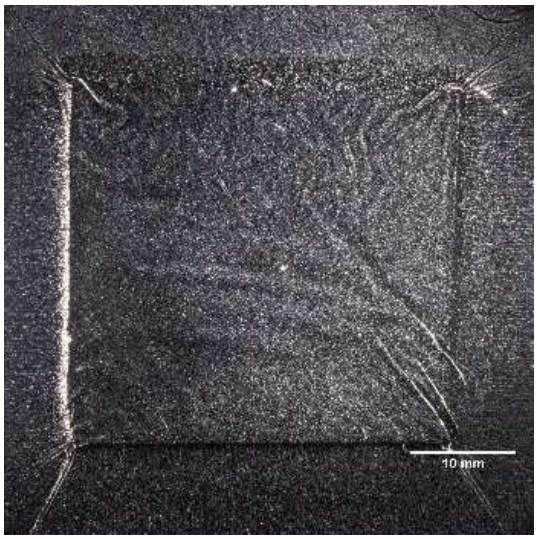

Figure 62: Image of sample on which stationary XRF analysis was done with the copper plate positioned underneath the sample

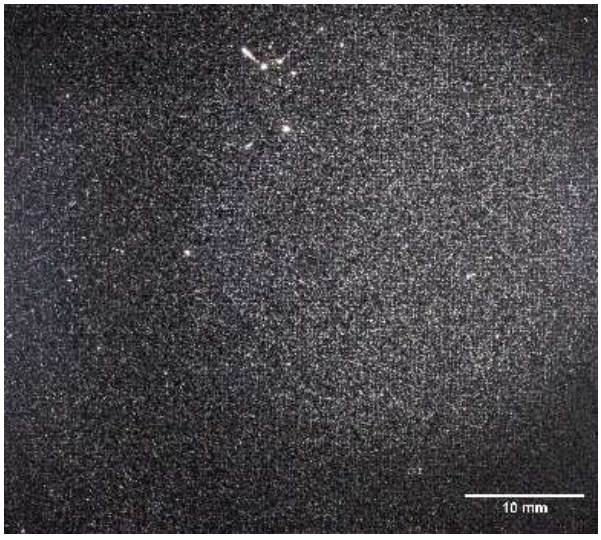

Figure 63: Image of sample on which stationary XRF analysis was done without the copper plate underneath

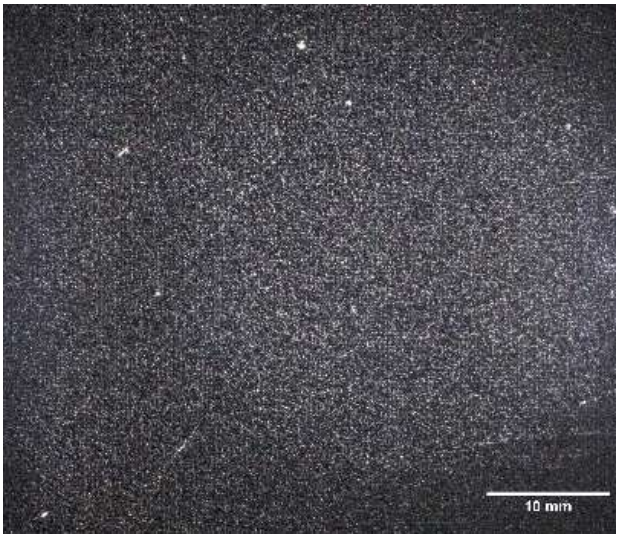

Figure 64: Samples on which in-line XRF analysis was done

Optical microscopy images were also taken (Figure 65 to Figure 67), which shows the defective areas where stretching and light translucency can clearly be seen. Figure 65 depicts a section of the area in which the copper plate used for stationary XRF analysis was set up under the membrane during coating, showing the permanent damage in the form of stretched areas of the membrane caused by the plate. Figure 66 and Figure 67 depicts the area in which stationary XRF analysis was conducted without the copper plate for comparison, from which no differences were noted in the quality.

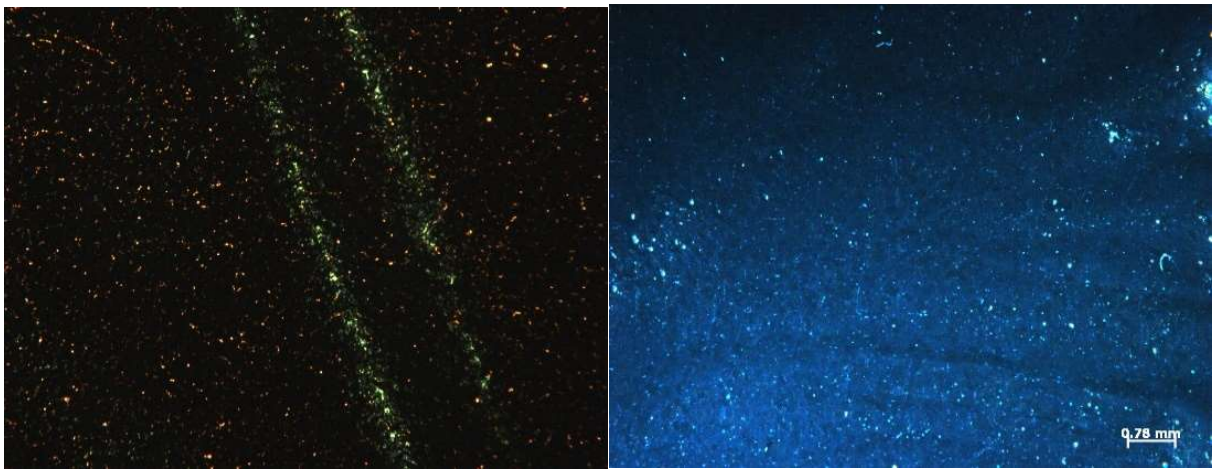

Figure 65: Image of sample on which stationary XRF analysis was done with the copper plate positioned underneath the sample (left – showing light translucency , right – showing surface image)

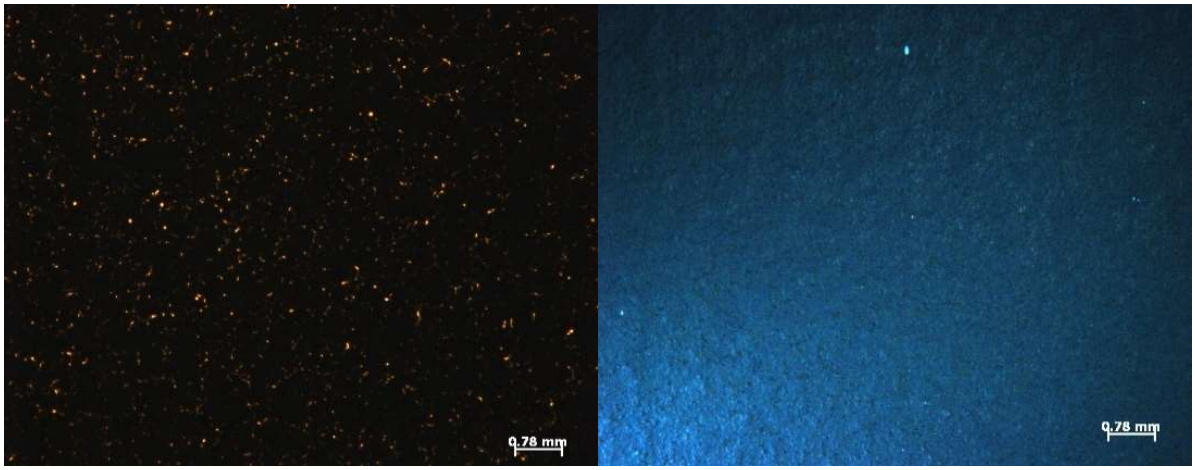

Figure 66: Image of sample on which stationary XRF analysis was done without the copper plate underneath (left – showing light translucency , right – showing surface image)

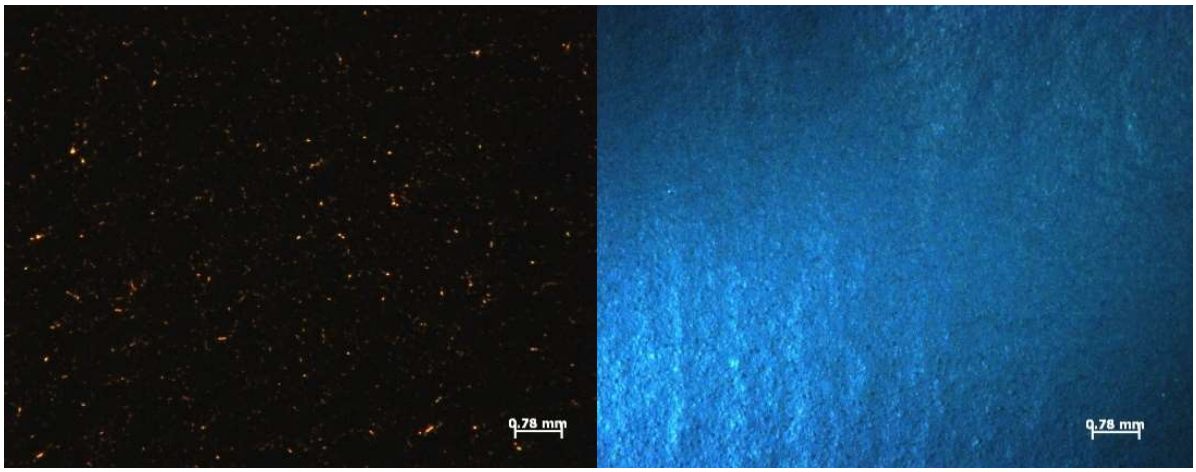

Figure 67: Samples on which in-line XRF analysis was done (left – showing light translucency , right – showing surface image)

The MEA samples that were coated on the high-volume line and tested using in-situ XRF testing were also analysed using the IRT test to see if the XRF might have caused any structural damage to the MEAs. The results shown in Figure 68, indicate no structural damage (such as pinholes) to the MEA from the XRF testing. However, stretching of the membrane and unevenly coated CLs was seen visually and by optical microscopy inspection which suggests that the current IRT setup is not sensitive enough to detect these sort of defects.

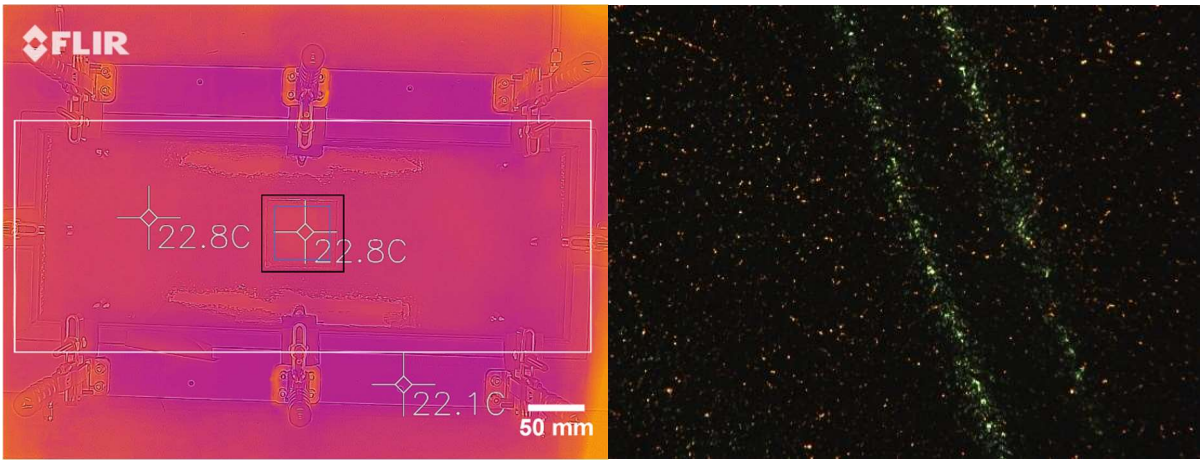

Figure 68: IRT image and microscopy image of sample on which stationary XRF analysis was done with the copper plate positioned underneath the sample

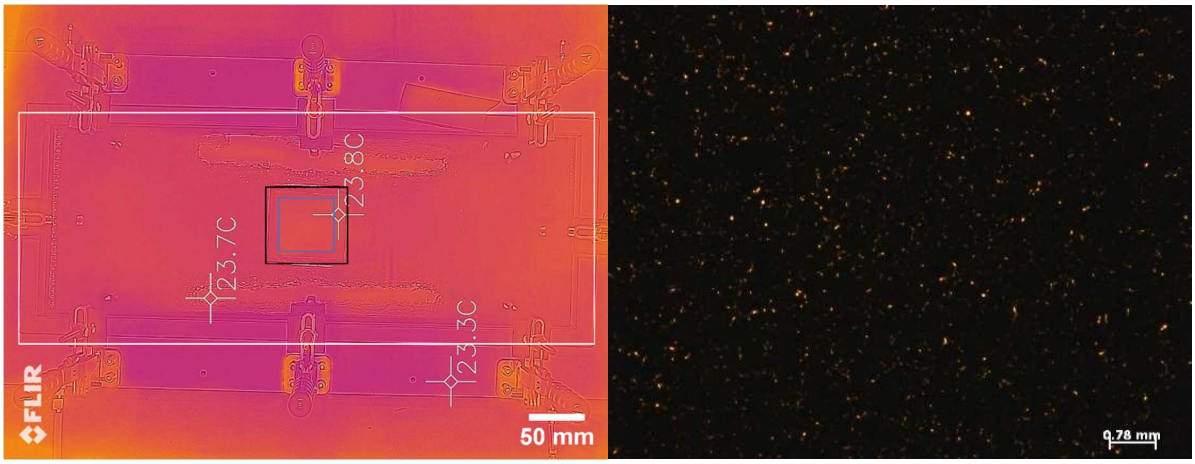

Figure 69: IRT image and microscopy image of sample on which stationary XRF analysis was done without the copper plate underneath (light translucency shown on the left and surface imaging shown on the right)

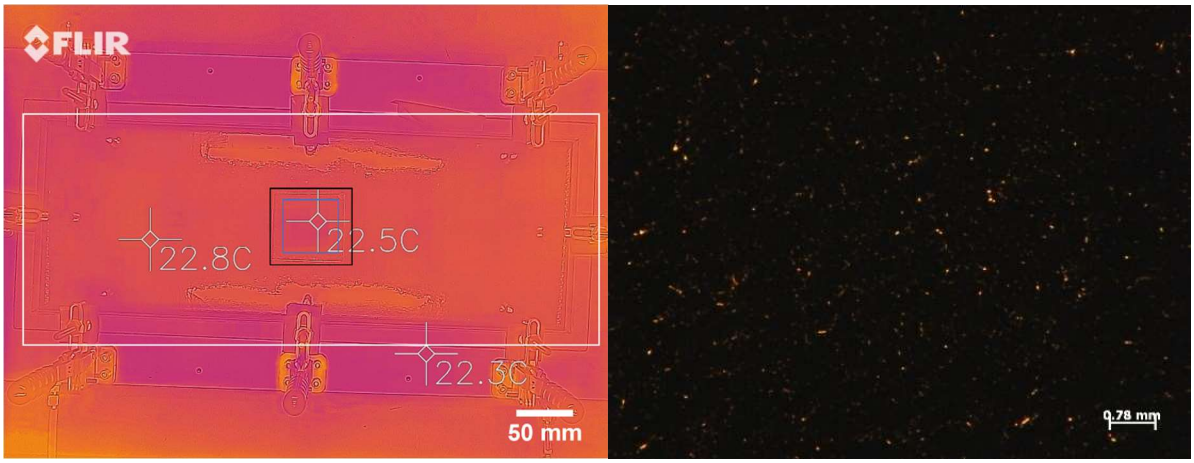

Figure 70: IRT image and microscopy image of samples on which in-line XRF analysis was done (light translucency shown on the left and surface imaging shown on the right)

CHAPTER VI: RESULTS & DISCUSSION

This chapter tabulates and depicts the results obtained for a batch of test MEAs that were run through the various quality control analysis to investigate each technique. The chapter ends with a summary discussing the relation between each quality control method analysed, how they relate to or impact one another and which techniques would have the best outcome for application in commercial manufacturing of MEAs. The MEA sample sets referred to in this chapter were described in detail in Table 6 Section 4.1.3. Some of data for the work done in this section can be found in APPENDIX A: Thickness Analysis, APPENDIX B: Gravimetric Analysis, APPENDIX C: Visual Inspection, APPENDIX D: Optical microscopy inspection, APPENDIX G: Single Cell Performance Testing and APPENDIX H: SEM. All other data can be seen upon request.

6.1. Thickness Analysis

Thickness was taken at 3 random points for each sample and averaged, the average of each sample set was then taken. The results are shown in Table 14.

Table 14: Results obtained for the thickness analysis for the batch of test MEAs (results displayed in the table are the average for each sample set (Error in the measurements is ±1 µm)

Electrode	**Cathode**			**Anode**		
Sample Set	Initial Thickness (µm)	Final Thickness (µm)	Net Thickness (µm)	Initial Thickness (µm)	Final Thickness (µm)	Net Thickness (µm)
1	15	43	28	43	64	21
2	15	42	27	42	60	19
3	15	42	27	42	60	18
4	15	44	28	43	61	18
4 - repeat	15	41	26	41	57	16
5	15	41	26	41	62	21
6	15	43	28	43	59	16
7	15	42	27	42	63	21
Average	15	42	27	42	61	19
Standard deviation	0	2	2	2	2	2

From *table 10* above, it can be seen that the average thickness for the cathode is 27 µm at a loading of 0.40 mgPt/cm^2 and 19 µm for the anode at a loading of 0.20 mgPt/cm^2 – both of which are in line with the inhouse and commercial standards of 25-30 µm for a 0.40 mgPt/cm^2 loading and 15-20 µm for a 0.20 mgPt/cm^2 loading. The standard deviation for the cathode layers were 1.5 µm whereas the anode layers had a standard deviation of 2.2 µm. This is a result of the cathode layer being sprayed first and having less deviations, as non-uniformities in the cathode layer can cause deviations in the anode layer to appear more pronounced.

6.2. Gravimetric Analysis

Gravimetric loadings were taken for each sample, the average of each sample set was then taken and is shown in Table 15.

Table 15: Results obtained for the gravimetric analysis for the batch of test MEAs (results displayed in the table are the average for each sample set (Error in the measurements is ±0.1 mg for weights and 0.01 mg/cm^2 for loadings)

Sample set	Sample	Initial Weight (g)	Final Weight (g)	Net Weight (g)	Loading (mg Pt /cm2)	Initial Weight (g)	Final Weight (g)	Net Weight (g)	Loading (mg Pt /cm2)
1	1	0,14	0,18	0,034	0,41	0,18	0,19	0,017	0,20
2	1	0,14	0,18	0,033	0,40	0,18	0,19	0,017	0,20
3	1	0,14	0,18	0,034	0,41	0,18	0,20	0,017	0,20
4	1	0,14	0,18	0,034	0,41	0,18	0,19	0,017	0,21
4 - repeat		0,14	0,18	0,033	0,40	0,18	0,20	0,016	0,20
5	1	0,14	0,18	0,034	0,41	0,18	0,19	0,017	0,20
6	1	0,14	0,18	0,035	0,42	0,18	0,20	0,017	0,20
7	1	0,14	0,18	0,034	0,41	0,18	0,19	0,017	0,20
Average		0,14	0,18	0,034	0,41	0,18	0,20	0,017	0,20
Standard deviation		0,002	0,002	0,001	0,007	0,002	0,002	0,000	0,004

From Table 15, it can be seen that the average loading for the cathode is 0.41 mgPt/cm^2 and 0.20 mgPt/cm^2 for the anode. This coincides with the previous section, whereby a loading of 0.40 mgPt/cm^2 should have a thickness of between 25-30 µm and the thickness was 27 µm for the cathode layer. A loading of 0.20 mgPt/cm^2 should have a thickness of between 15-20 µm and the thickness was 18 µm. This confirms that the thickness and the loading are in agreement with each other.

Furthermore, data collected during the coating calibration for the XRF method development (Section 5.3.1), was also used to demonstrate that the thickness has a fairly linear relationship to the PGM loading, this is depicted in Figure 71 below. However, the relationship between the two was seen to be affected by the RH which caused membrane swelling and increased/decreased rehydration rates.

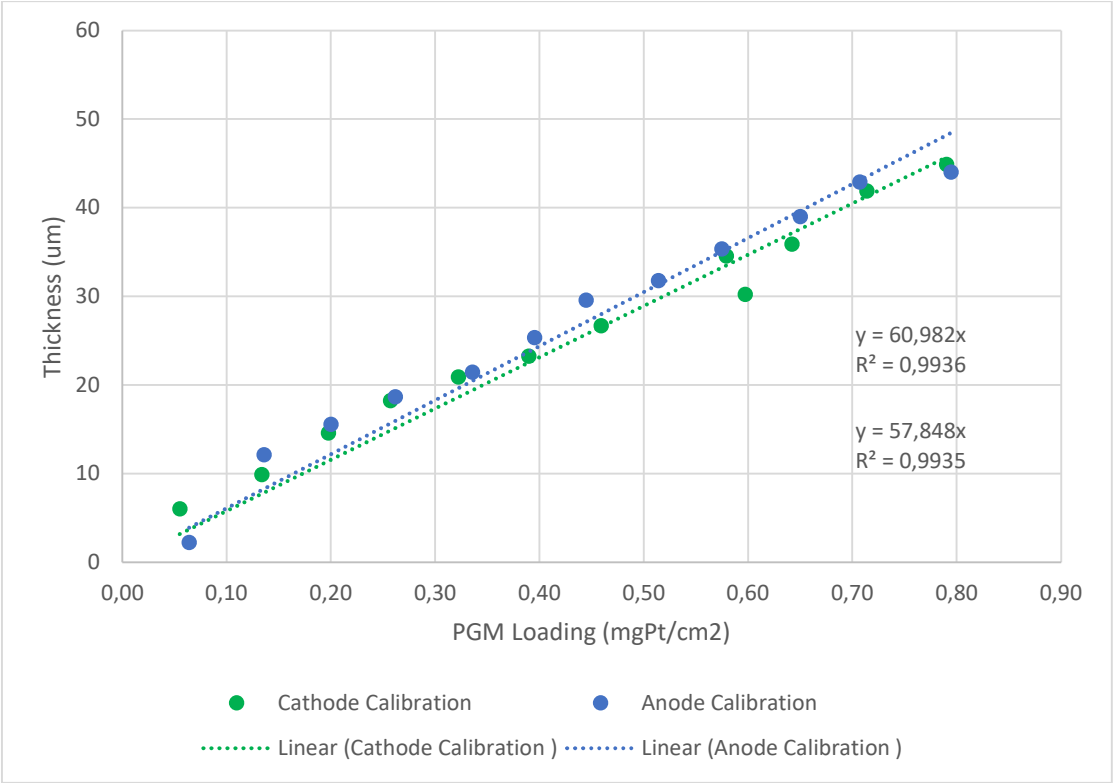

Figure 71: Graph depicting relationship between CL thickness and gravimetric PGM loading

6.3. Automated Visual Inspection

The visual inspection was carried out for the cathodes and anodes. An example of the results obtained are shown in Figure 72 and Figure 73. Figure 72A is an example of the good CLs that were seen during visual inspection – these layers show no light translucency , cracking or flaking of the CL. Figure 73 is an example of CL defects that were seen, which have minor light spots.

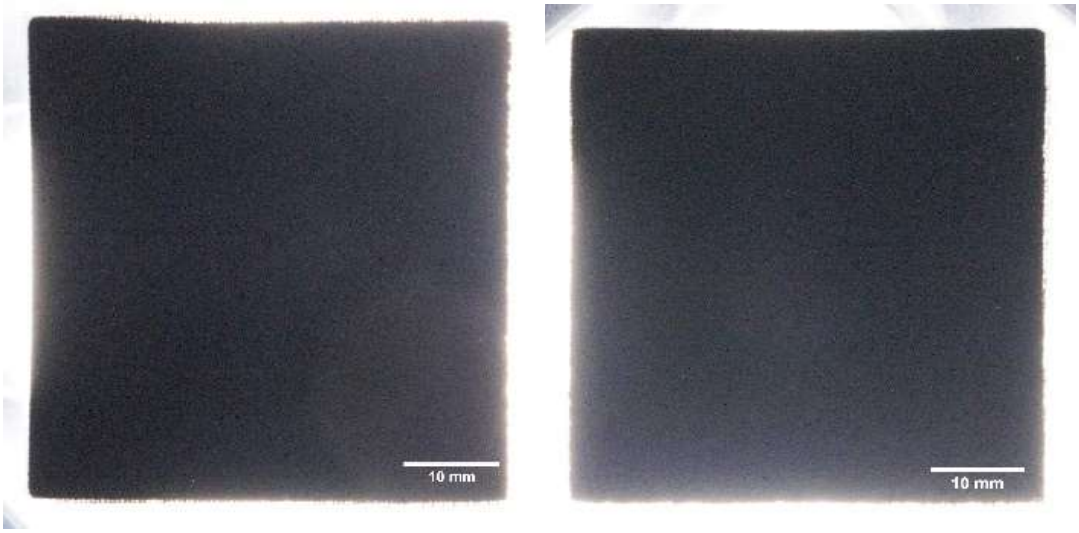

Figure 72: Left – Cathode on half CCM, Right – Anode of full CCM

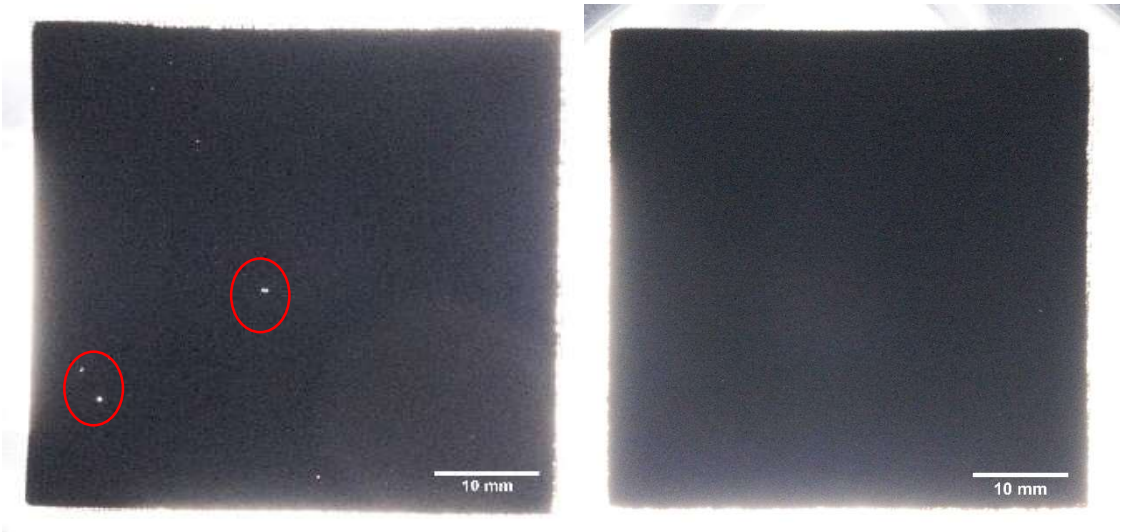

Figure 73: Left – Cathode on half CCM, Right – Anode of full CCM

On the anode layers, the light translucency becomes more difficult to spot visually due the presence of the cathode layer masking light spots in the anode layer. Figure 73 provides a good example of the effect of one electrode masking defects of another electrode – the defect zones previously highlighted on the cathode can no longer be seen once the anode was sprayed due to the overlapping / masking effect of the one electrode on the other.

Table 16 shows the results of the amount of light translucency seen from the visual inspection. The average amount of light translucency per sample set was between 0.0-0.1%, with an average of 0.006% for the cathode and 0.001% for the anode. This is below the commercially accepted standard

of 10.0%, which is the maximum amount of light translucency allowed for a good quality MEA according to information shared from HySA catalysis' commercial partner.

Table 16: Average Light translucency (%) per sample set for Visual Inspection

Sample set	Cathode Translucency (%)	Anode Translucency (%)
1	0,009	0,000
2	0,010	0,001
3	0,004	0,001
4	0,006	0,002
5	0,003	0,002
6	0,004	0,001
7	0,010	0,001
Overall Average	0,006	0,001

6.4. Optical microscopy inspection

The optical microscopy inspection was carried out for the cathodes and anodes. An example of the results that were obtained are shown in Figure 74. The images selected for discussion in this section of the report match the samples selected in the visual inspection to allow for comparison between the two methods.

From Figure 74A, it can be seen that optical microscopy inspection did not yield different results to the visual inspection and no light translucency could be seen at the highest magnification. Figure 74B shows that with optical microscopy inspection, more details can be seen around the defective zones – these details include the shape and size of the light spot. Figure 74C and Figure 74D focus on surface defects which could not be seen by visual inspection – these include debris, wrinkling and surface scratches.

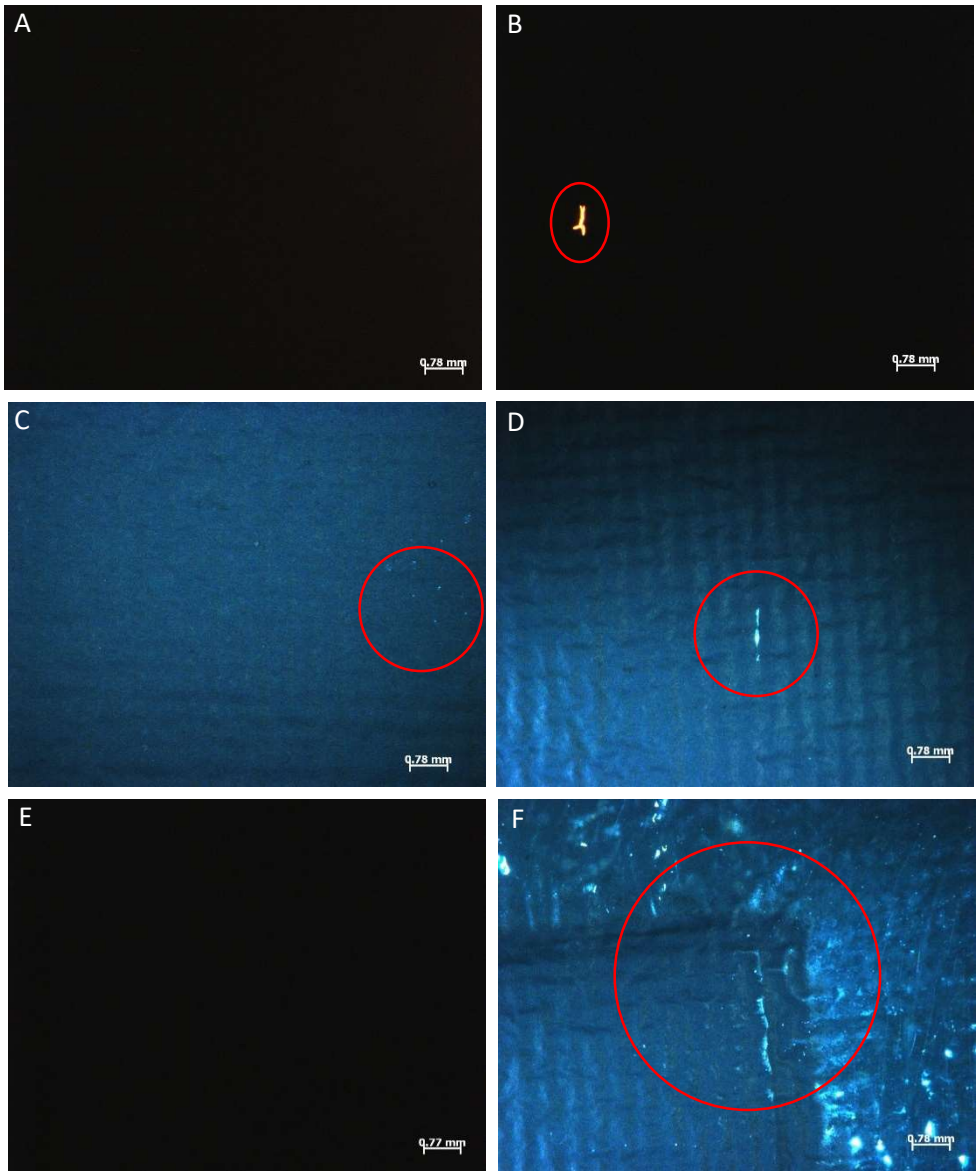

Figure 74: A -- Cathode on half CCM shown in Figure 72, B – Cathode on half CCM shown in Figure 73, C – Surface image showing debris on cathode CL, D – Surface image showing scratches on anode CL, E – Anode on half CCM shown in Figure 72, F – Electrode misalignment at the perimeter of the AA coated.

Comparing Figure 74B and Figure 74E shows the effect of an electrode masking another electrodes defects as discussed previously in the visual inspection chapter. Figure 74F shows misalignment of the two electrodes, which occurs along the perimeter of the AA during the CL deposition in fabrication.

Table 17 shows the results for the amount of the light translucency seen in the microscopic images. The amount of light translucency was between 0.0-2.0%, with an average light translucency of 0.61% for the cathode. This is below the commercial quality standard of 10.0%, which is the maximum amount of light translucency allowed for a good quality MEA. The assessment could not be done for the anode as no light translucency was seen and the microscope was unable to capture the full black images.

Table 17: Average Light translucency (%) per sample set for Optical microscopy inspection

Sample set	Cathode Translucency (%)
1	0,57
2	1,28
3	0,35
4	0,63
5	0,16
6	0,19
7	0,41
Overall Average	0,61

6.5. Infrared Thermography

The MEAs from sample set 5 and 6 were analysed using the IRT method developed and an example of the results obtained are depicted in Figure 75. All 6 samples displayed good quality MEAs with regards to pinholes and gas crossover as there are no IR signatures displaying temperature spikes for defects.

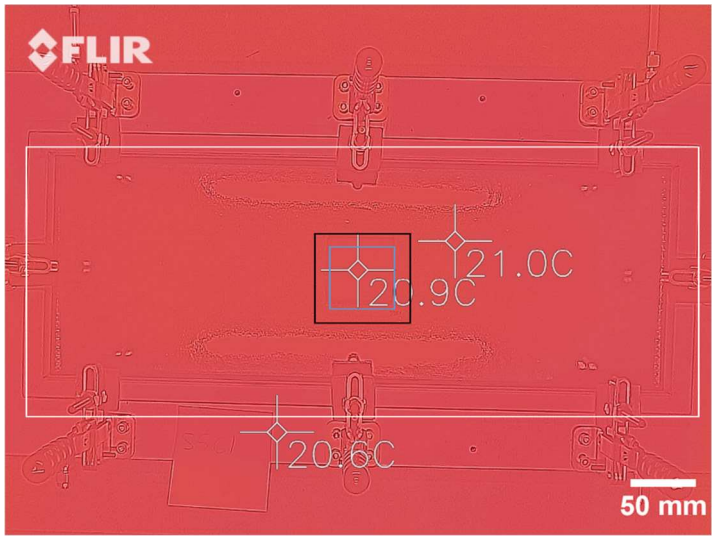

Figure 75: IRT result for Sample 1 of Sample Set 5

6.6. X-Ray Fluorescence

The MEAs from sample set 2 and 3 were analysed using the XRF method developed and the results are shown in Table 18. From the results, it can be seen that the XRF loadings are 0.08 mg/cm^2 higher than the gravimetric loading for both the cathodes and the anodes. This indicates that either the gravimetric analysis is incorrect, which is possible due to the gravimetric analysis being sensitive to humidity or the XRF results are incorrect due to errors in the calibration.

Table 18: Gravimetric and XRF Loading Analysis for test MEAs (Error in the measurements is 0.01 mg/cm^2 for loadings)

Sample set	Sample	Gravimetric Loading (mg Pt /cm2)	XRF Reading (%)	XRF Loading (mg Pt /cm2)	Gravimetric Loading (mg Pt /cm2)	XRF Reading (%)	XRF Loading (mg Pt /cm2)
2	1	0,40	6,2	0,49	0,20	3,1	0,30
	2	0,40	6,0	0,48	0,20	2,9	0,28
	3	0,40	5,8	0,46	0,22	2,9	0,28
3	1	0,41	6,2	0,50	0,20	2,9	0,29
	2	0,40	6,6	0,53	0,20	2,3	0,22
	3	0,41	6,0	0,48	0,20	3,2	0,31
Average		0,41	6,1	0,49	0,20	2,9	0,28
Standard deviation		0,01	0,24	0,01	0,00	0,27	0,03

A membrane sample was then sprayed on the high-volume line and analysed using the XRF and the data tabulated below was obtained. The results show that the gravimetric loading is on par with the target loading. The target loading was obtained from a mylar coupon that was used to track the loading on the system. However, the XRF loading appears to be 0.1 $mg.cm^{-2}$ less than the gravimetric and target loading whereas the XRF loadings obtained for the loading analysis done on the test MEAs were 0.1 $mg.cm^{-2}$ more than the gravimetric loading.

Table 19: Results for XRF Test on the High-Volume Line

Sample	XRF on Copper Plate	XRF on Stainless Steel Belt (Stationary)	XRF on Stainless Steel Belt (Moving)
Target Loading ($mg.cm^{-2}$)	0.51	0.51	0.51
Gravimetric Loading ($mg.cm^{-2}$)	0.50 ± 0.01	0.50 ± 0.01	0.50 ± 0.01
XRF Loading ($mg.cm^{-2}$)	0.40 ± 0.01	0.42 ± 0.01	0.42 ± 0.01

Further work was conducted to assess the discrepancy between the XRF result obtained compared to the gravimetric result obtained. Conducting an XRF analysis at very low loadings (< 0.1 mg/cm^2) verified that the XRF was perhaps more sensitive to the loadings than the gravimetric analysis. The results displayed in Figure 76, confirm that the gravimetric analysis does not provide sufficient resolution in discrepancies under 0.1 mg/cm^2 as the gravimetric loadings begin to plateau between 0.02 – 0.05 mg/cm^2 and thereafter start to increase but not in proportion to the theoretical loading. Furthermore, the XRF loading has a linear relationship to the theoretical loading, however, the data obtained for the XRF readings have loadings that are approximately double relative to the theoretical loading.

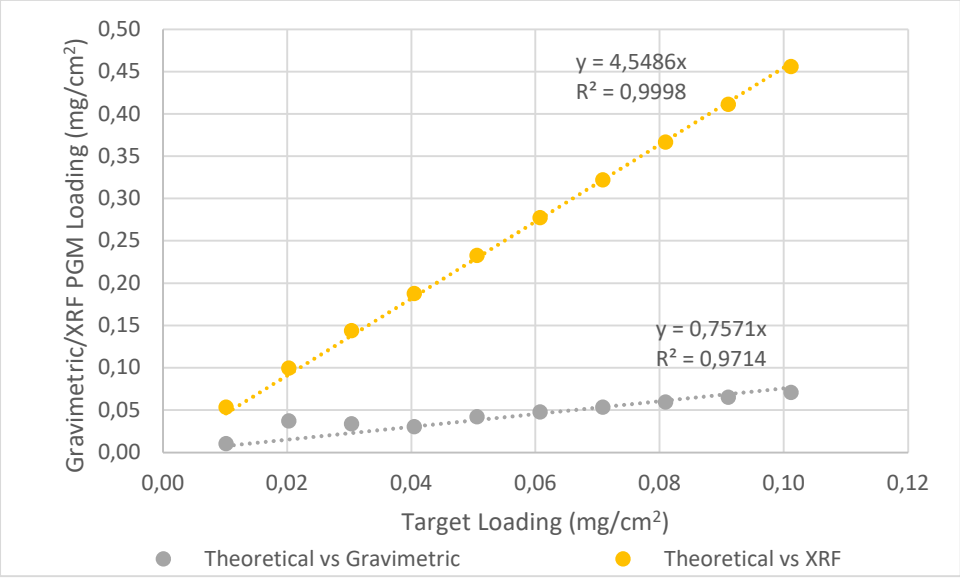

Figure 76: XRF analysis at PGM loadings below 0.1 mg/cm^2

If the gravimetric system is needed to calibrate the XRF system initially, the errors in the gravimetric system are propagated due to the XRF being sensitive to the minor changes in the loading and the gravimetric system being unable to detect these. This explains the offset in the data obtained in Table 18 and Table 19 Due to the time and budget constraints on this study, the accuracy pertaining to low loadings or smaller changes in loadings could not be investigated further but requires further work.

6.7. Single Cell Performance Characterisation

Single cell performance testing was carried out on 4 of the sample sets – the results of which are discussed in Section 6.7.1, 6.7.2, 6.7.3 and 6.7.4.

6.7.1. Activation / Conditioning

Figure 77 and Figure 78 depicts the cell performance during conditioning and provides information about the break-in of the MEAs in the different data sets. From Figure 77, which displays the OCV, it can be seen that all 3 sample sets had a similar break-in to the benchmark samples during the first two cycles. After which, the XRF tested samples performed on par with the benchmark samples. The samples that had gone through IRT plateaued at 0.955 V compared to the benchmark at 0.950 V. Lastly the samples that underwent intensive XRF testing also plateaued at a similar OCV to the IRT samples but then experienced a spike in the OCV between the third and sixth cycle, plateauing out at 0.01 V more than the benchmark. Therefore, according to the OCV data, neither the XRF nor IRT negatively affected the MEAs.

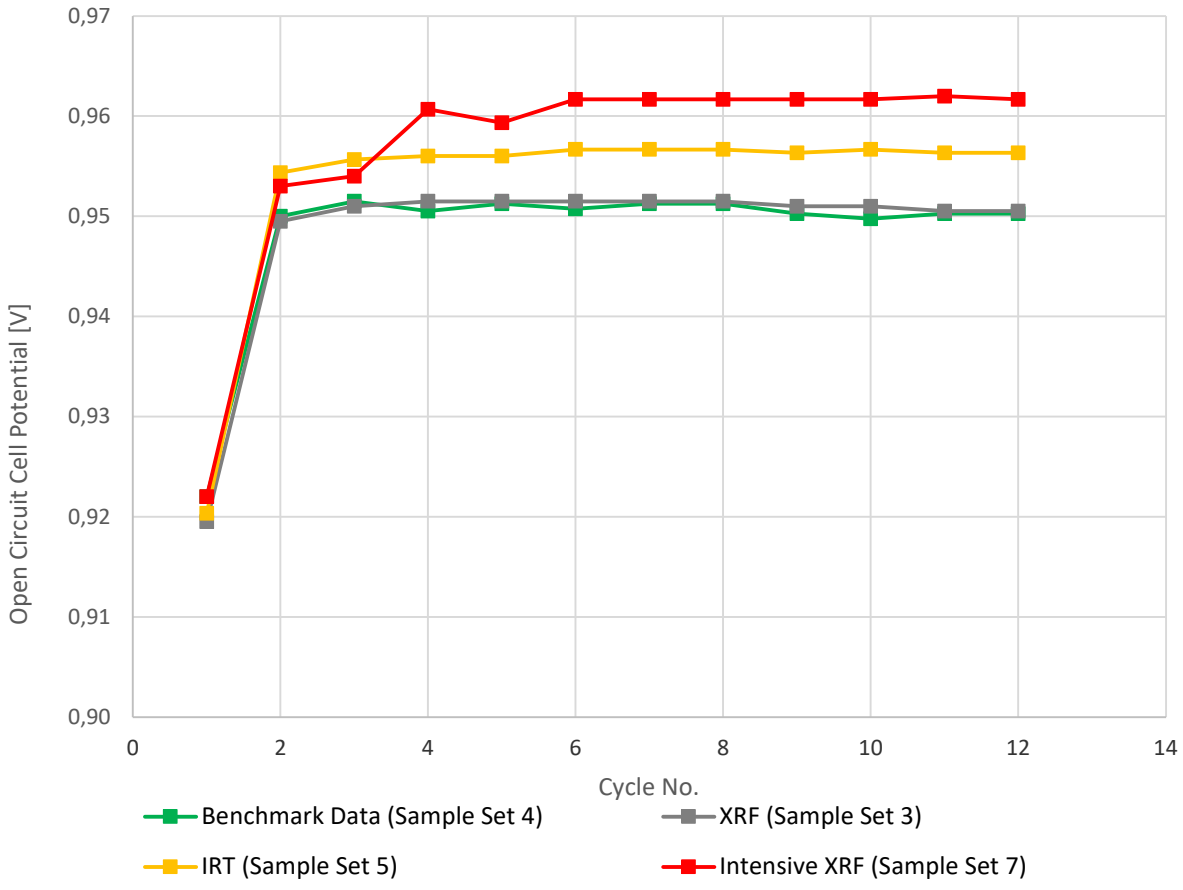

Figure 77: OCV Performance Data (Displayed as averages of each sample set)

Figure 78, which displays the current density at 0.30 V during conditioning, further confirms the trends seen in the OCV curve. All the samples oscillate around the same current density as the benchmark samples, i.e. 2000 mA.cm^{-2}.

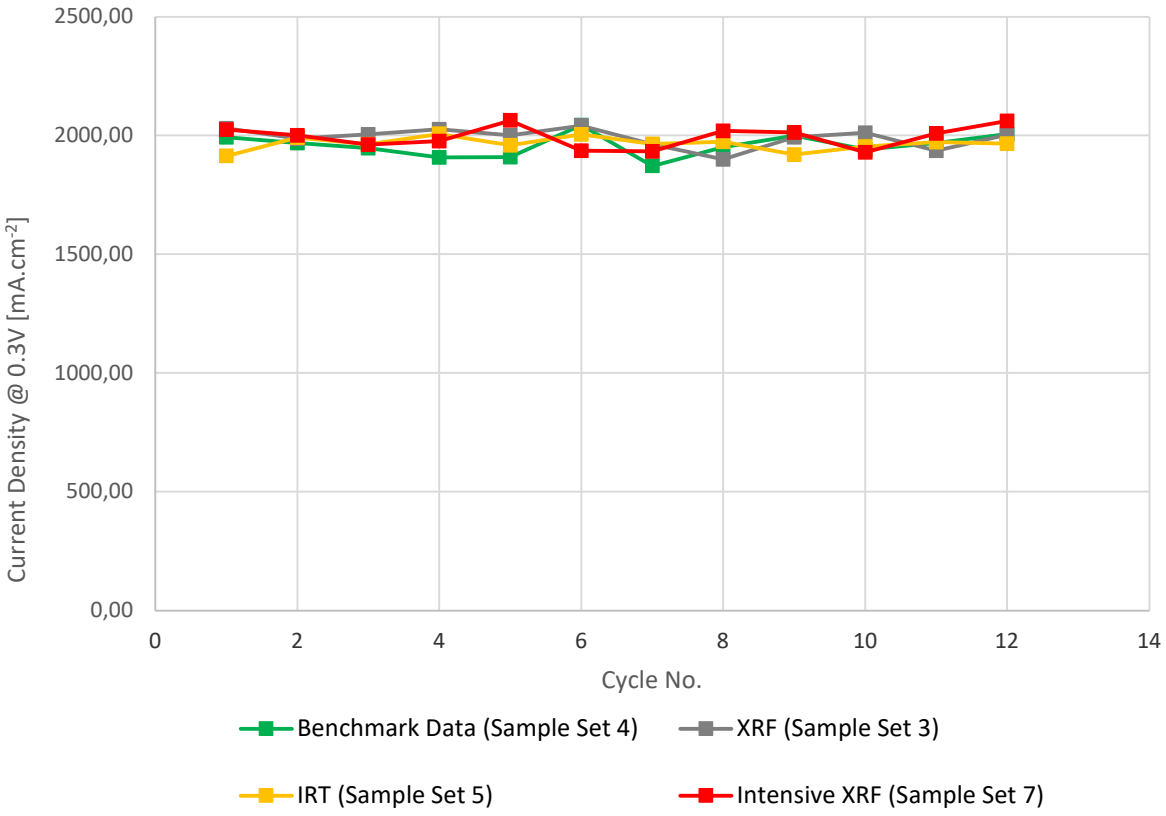

Figure 78: Current Density (at 0.3V) Performance Data (Displayed as averages of each sample set)

6.7.2. Open Circuit Voltage

The OCVs that were seen at the beginning of the polarisation curves are depicted in the graph below. Figure 79 shows that the samples within each data set as well as between data sets performed similarly. The average OCV seen across the sample sets was 0.93, 0.92, 0.94 and 0.94 V for the benchmark, XRF, IRT and intensive XRF sample sets, respectively.

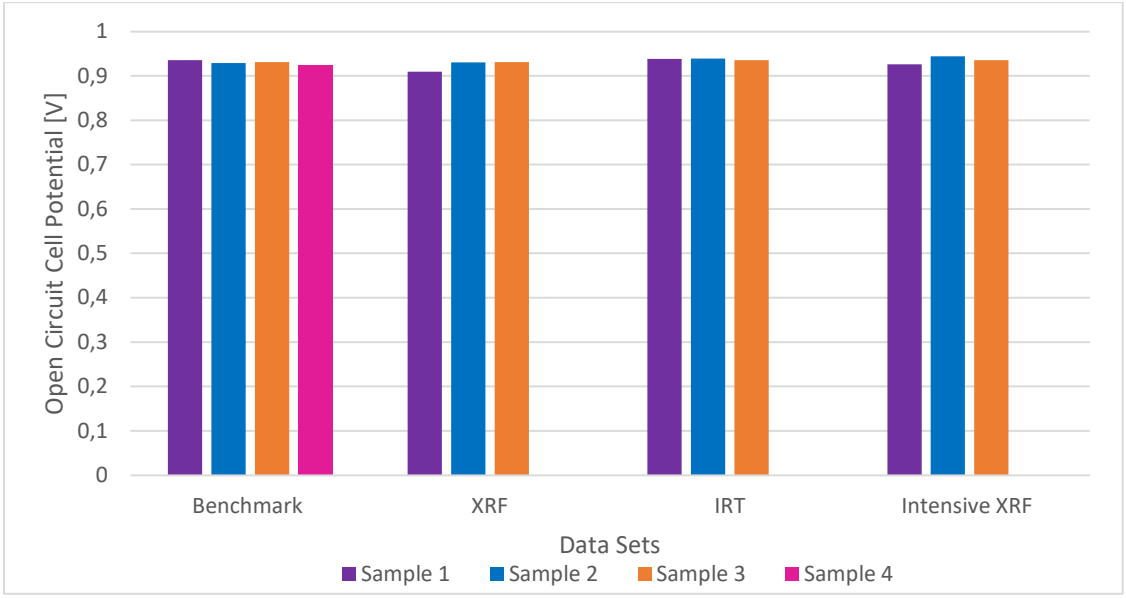

Figure 79: Open Circuit Voltage at the beginning of the polarisation curves

6.7.3. Polarisation Curves

According to the U.S Department of Energy (2016) the technical targets for 2020 were a performance of 300 mA/cm^2 at 0.8V in the low current density region. Internal performance benchmarks from HySA Catalysis depict single cell MEA performance at 1200 mA/cm^2 at 0.6V in the high current density region (APPENDIX G: Single Cell Performance Testing, Figure 94). These performance targets were both met during testing. Figure 80, Figure 81 and Figure 82 depict the polarisation curves obtained for this study. Figure 80 depicts the polarisation curves obtained for the different samples in sample set 4, i.e., the benchmark samples. This graph was plotted to demonstrate the performance repeatability between samples within a set and shows the close overlap in data between the samples. Therefore, successfully showing that repeatability within the sample sets was achieved.

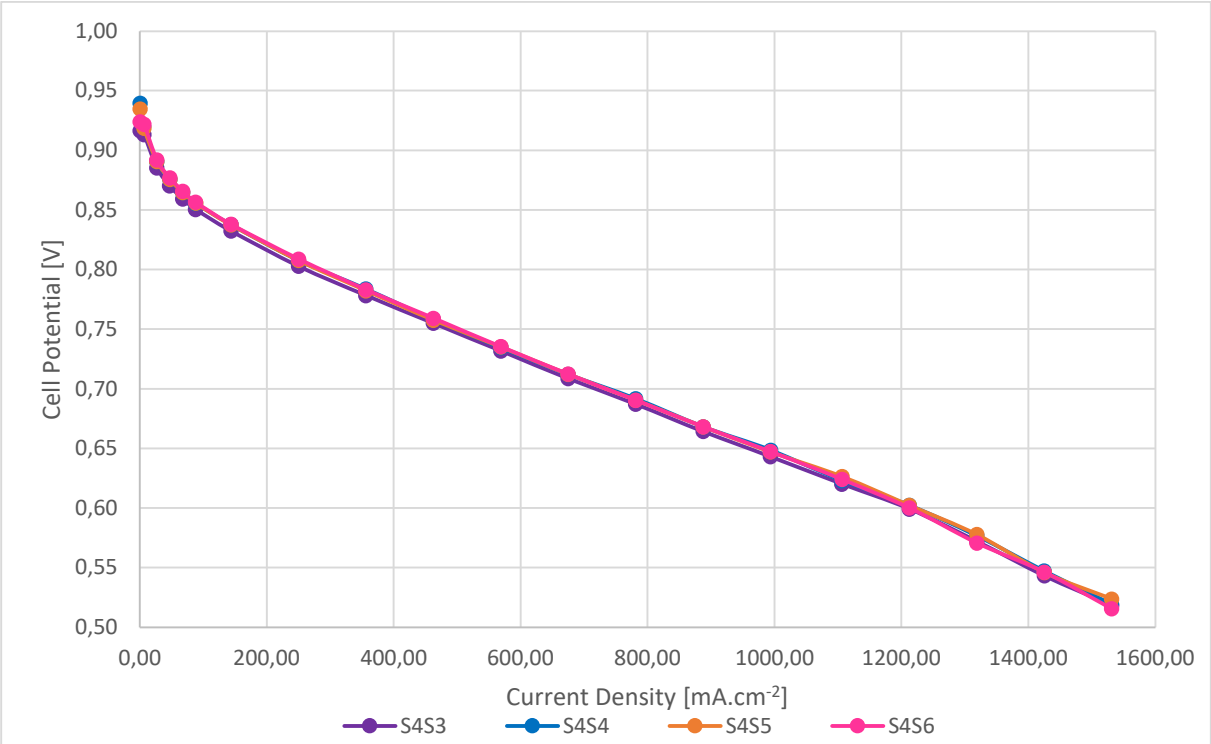

Figure 80: Polarisation Curves for the Benchmark Samples

Figure 81 depicts the polarisation curves obtained for the samples in set 3, i.e., the XRF tested samples. It can be seen that sample 1 had a poor performance compared to its counterparts and pulls the average of the sample set down. This was a result of fuel starvation during testing, which causes cell reversal and reduces the power output. Fuel starvation also causes severe and irreversible damage due to carbon corrosion and dehydration thus the sample could not be retested and was omitted from any further results so that it would not skew the average data of that set.

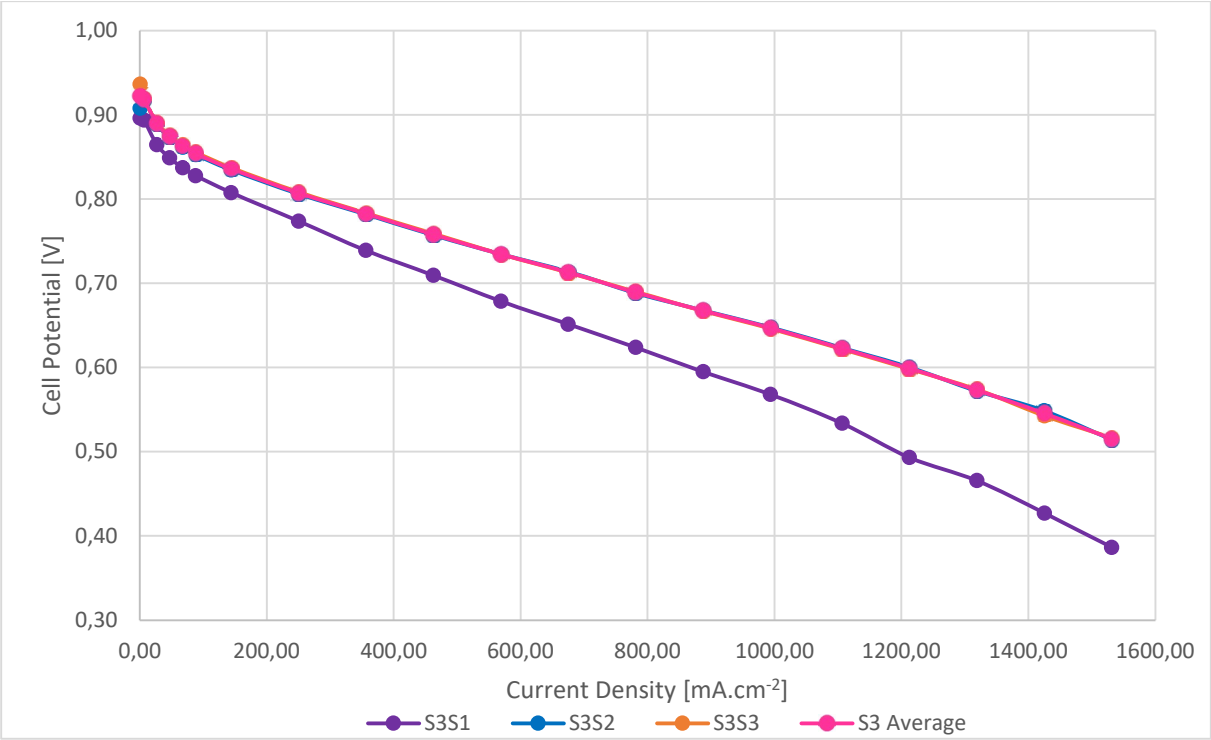

Figure 81: Polarisation Curves for the XRF Samples

Figure 82 depicts the averaged polarisation curves of each sample set. The internal benchmark for HySA Catalysis has a minimum of 0.90 V at open circuit, 0.70 V at 700 mA/cm^2 and 1000 mA/cm^2 at 0.60 V – the benchmark data from the tests conducted in this study were on par with the institutions internal benchmarks. From the cell potential, it can be seen that all 4 sample sets perform similarly at lower current density and only start to deviate as we reach current densities above 800 mA.cm^{-2}, showing a maximum difference of 0.01 V at 1500 mA.cm^{-2} between samples. The polarisation curves further strengthen the argument that neither XRF or IRT have a negative impact on the MEAs performance.

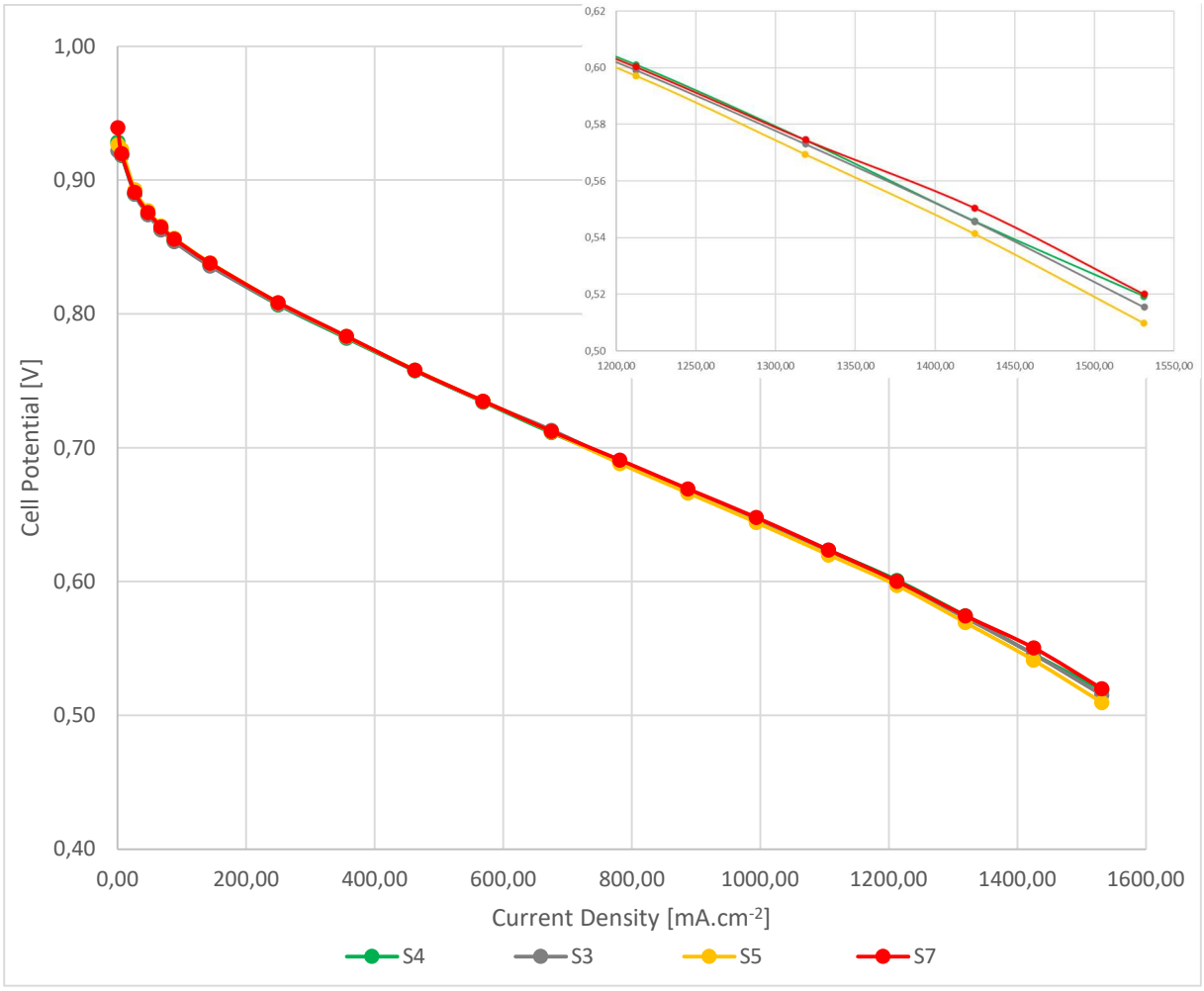

Figure 82: Averaged Polarisation Curves for each sample set

6.7.4. Electrochemical Impedance Spectroscopy

Figure 83 and Figure 84 depict the electrochemical impedance spectra obtained during performance testing. Figure 83 specifically looks at the impedance obtained for the different samples in sample set 4, i.e. the benchmark samples. This graph was plotted to demonstrate the repeatability between samples within a set. The graph shows the close overlap in data between the samples, therefore, successfully showing that repeatability within the sample sets was achieved.

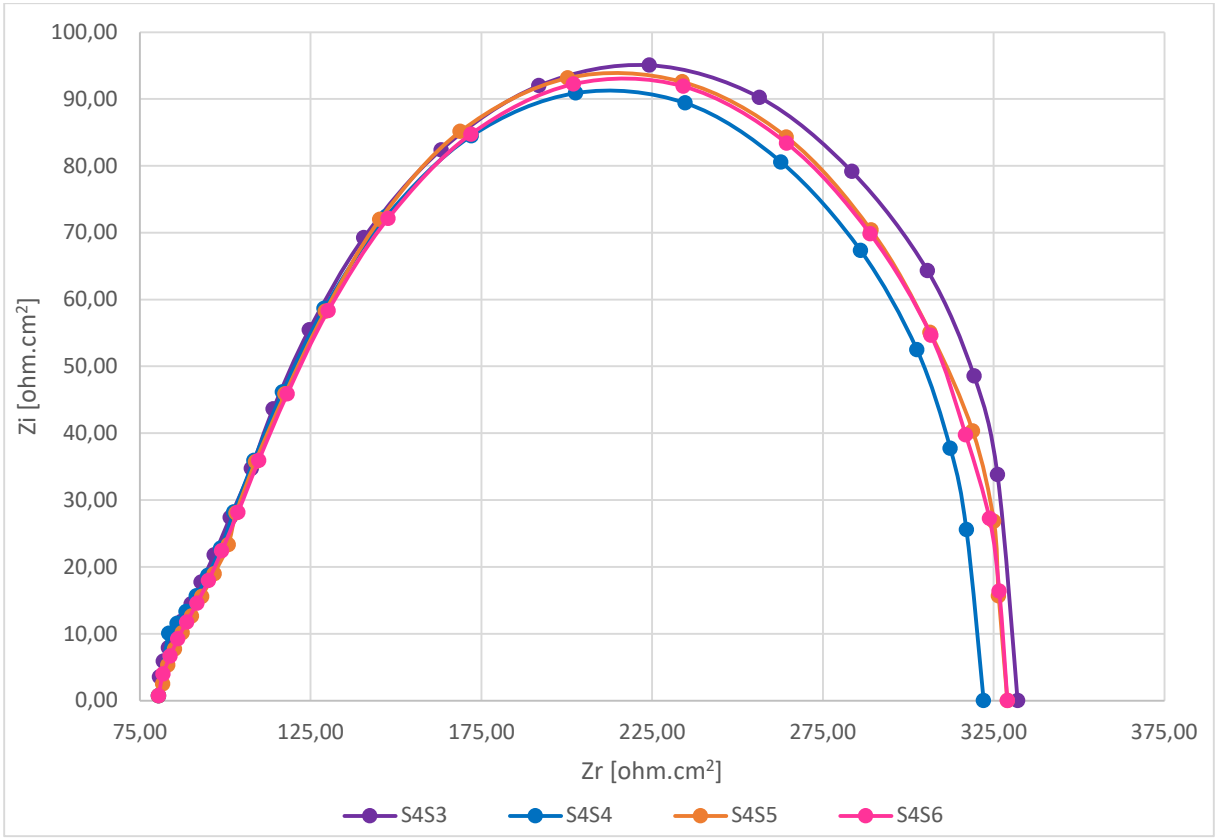

Figure 83: EIS Curve for Benchmark Samples

Figure 84 depicts the averaged impedance curves of each sample set. It can be seen that similar to the performance observed on the polarisation curves, the samples are on par with the benchmark.

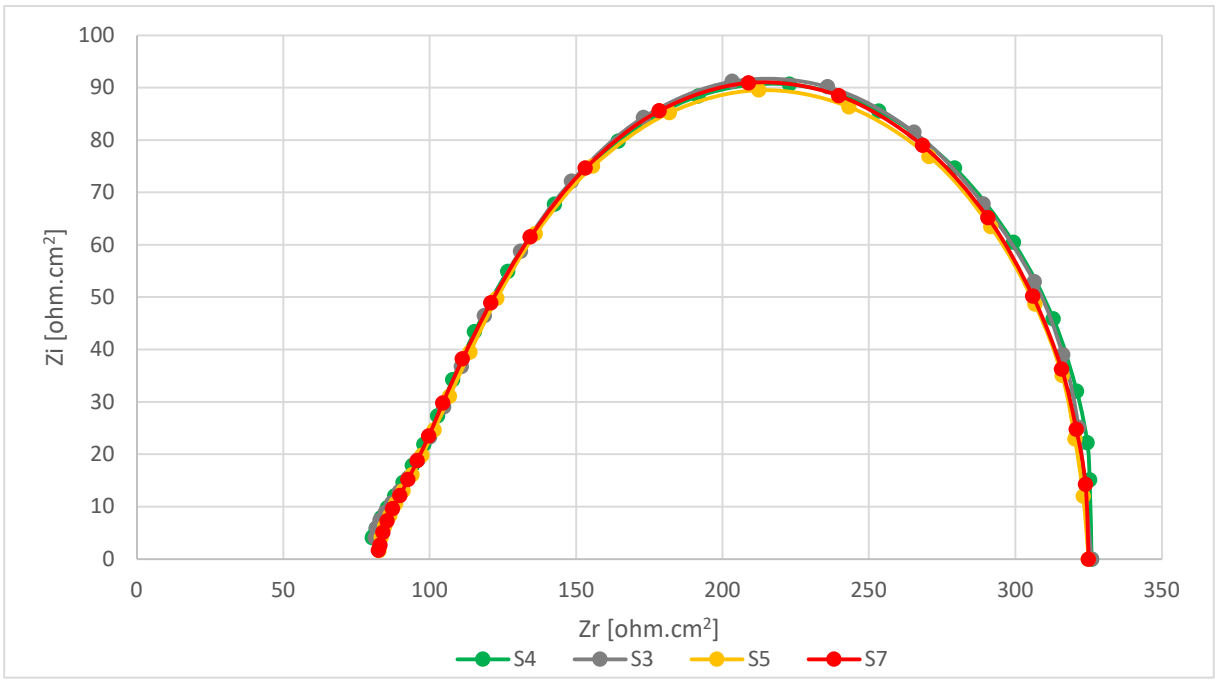

Figure 84: Average EIS curve for each sample set

From Figure 84, the resistance relating to ohmic and activation losses was calculated and are shown in Table 20. However, the resistance relating to mass transfer losses cannot be seen on the graph as a result of EIS being done in the low current density region where activation losses are dominant.

Table 20: Resistance for Sample Sets based on EIS data

Sample Set	Ohmic Resistance (Ω)	Activation Resistance (Ω)
4 (Benchmark)	80,6	245
3 (XRF Tested)	81,4	245
5 (IRT Tested)	82,7	242
7 (Intensive XRF Tested)	82,5	242

6.8. SEM Analysis

The cross sectional and surface image results for CL thickness and defect identification are discussed in the Section 6.8.1 and 6.8.2.

6.8.1. Thickness Analysis from Cross Sectional Imaging

Using cross-sectional imagining, thickness was analysed at 3 magnifications for each sample and averaged, the average of each sample set was then taken and is shown in Table 21. From the table, it can be seen that the average thickness for the cathode is 15.42 um at a loading of 0.4 mgPt/cm^2 and 5.68 um for the anode at a loading of 0.2 mgPt/cm^2. The thickness measurements obtained here are after the 7 layer assembly and cannot be compared to the thickness measurements in Section 6.1. However, the effect of the assembly on the layer compression can be seen as the average cathode thickness was 27.24 um and the average anode thickness was 18.68 um before assembly.

Furthermore, the data can be used to check whether the single-cell testing had an effect on the thickness due to compression, exposure to moisture and prolonged heating – according to the data there is no evident change in the CL thickness between the samples that had undergone single-cell testing (sample set 3, 4, 5 and 7) and those that did not (sample set 1, 2 and 6).

Table 21: Results obtained for the SEM thickness analysis for the batch of test MEAs

Electrode	Cathode	Anode
Sample Set	Thickness (um)	Thickness (um)
1	15,6	5,43
2	14,5	5,64
3	14,8	5,36
4	15,8	6,06
4 - repeat	15,6	7,11
5	14,2	5,11
6	15,9	5,79
7	15,8	4,91
Average	15,4	5,68
Standard Deviation	1,7	0,95

The cross-sectional imaging further allowed for defect identification as described by *Prasad (2019)* in Figure 10, which include microcracks within the CL, catalyst clusters / agglomerations and non-uniformities in the CL as shown in Figure 85, Figure 86, Figure 87, Figure 88 and Figure 89.

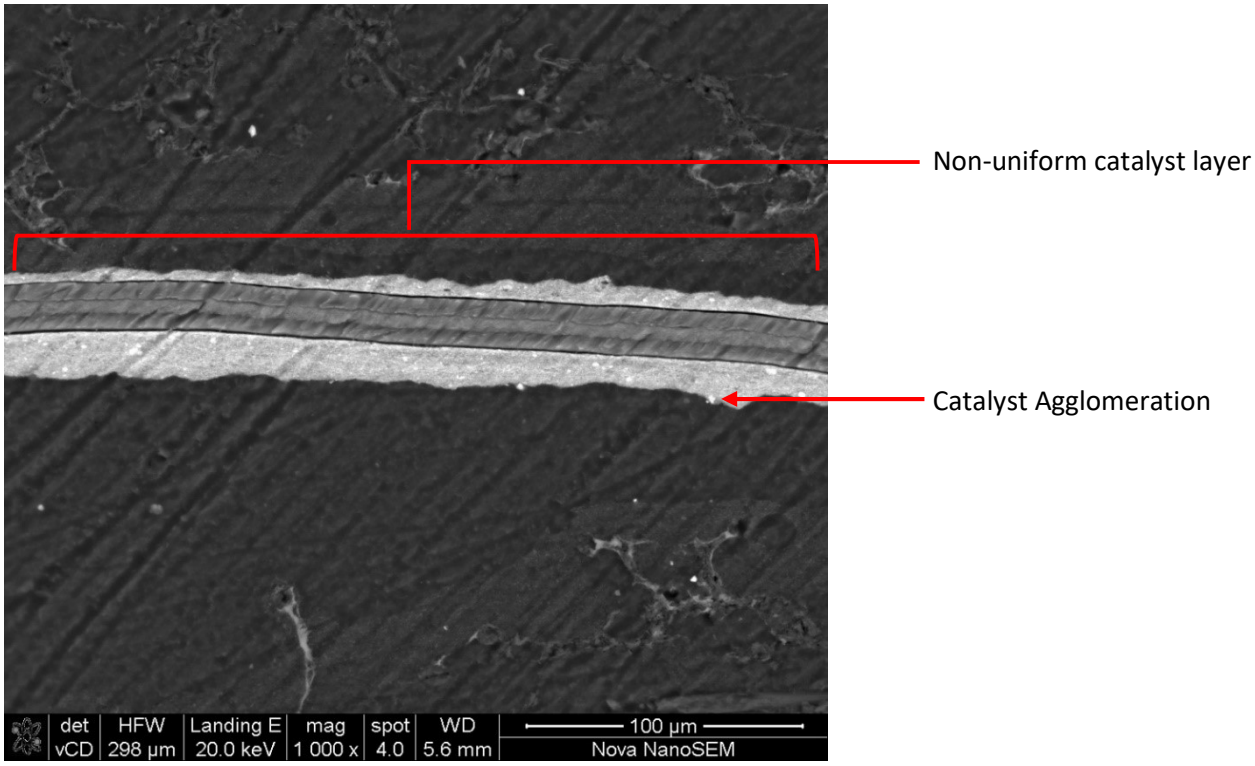

Figure 85: SEM Cross-sectional Image - S1C1

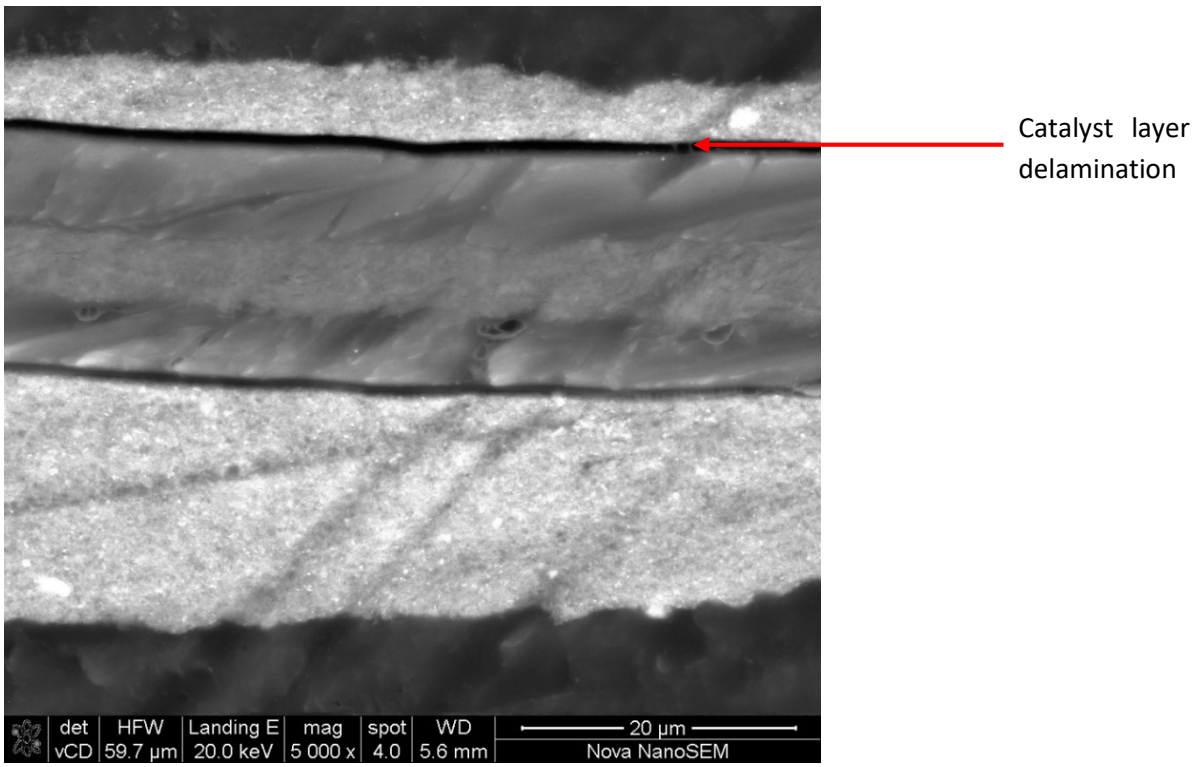

Figure 86: SEM Cross-sectional Image - S1C2

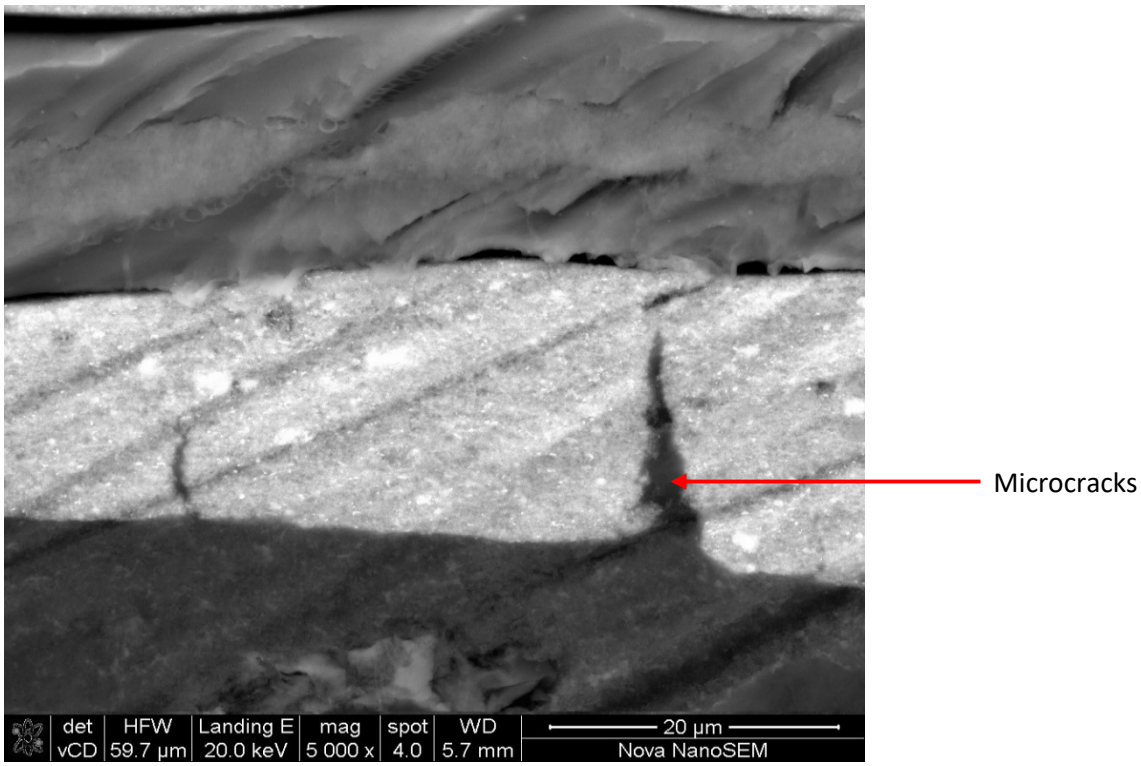

Figure 87: SEM Cross-sectional Image – S2C3

Furthermore, Figure 85 depicts a sample that had not undergone single cell performance characterisation (*Sample S1C2*) whereas Figure 88 depicts a sample that had undergone single cell performance characterisation (*Sample S3C3)* – likewise with Figure 87 (Sample S2C3) and Figure 89 (*Sample S3C2*). Both these comparisons show the negative/destructive effect that the testing had on the CLs by propagating crack formation and delamination.

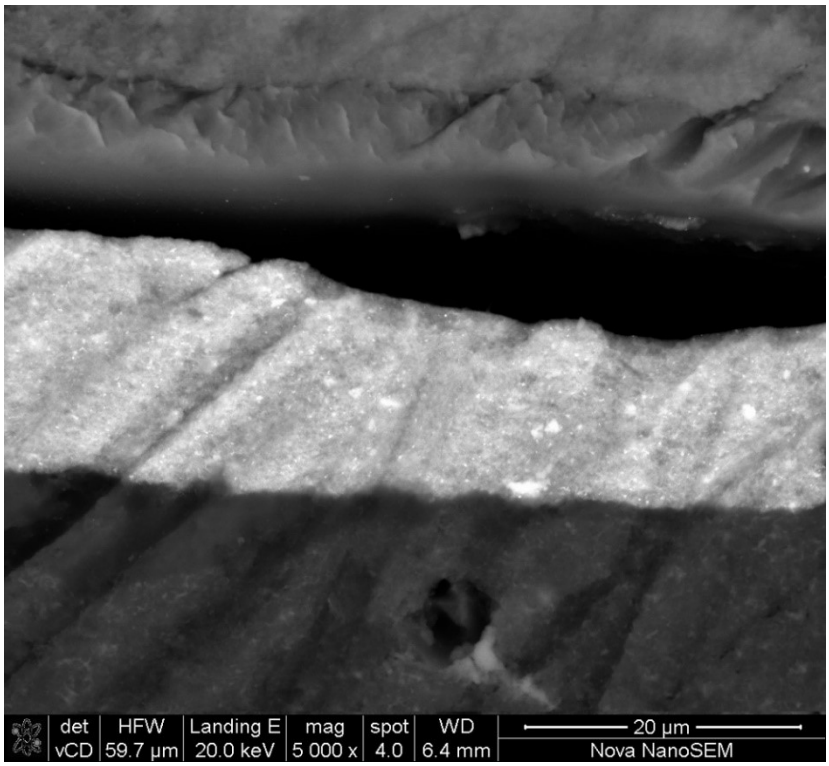

Figure 88: SEM cross-sectional image - S3C3

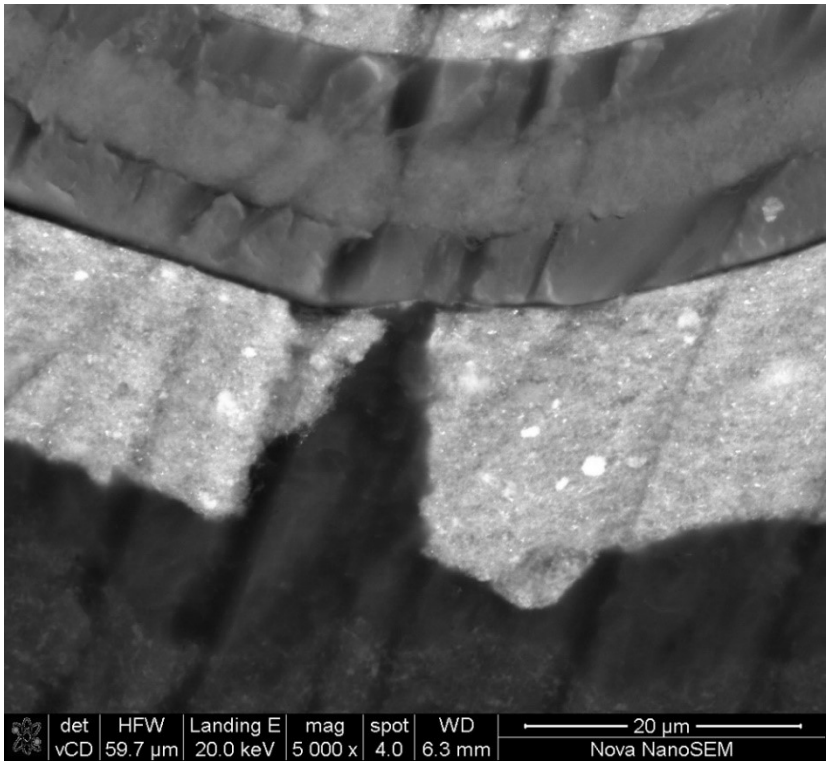

Figure 89: SEM cross-sectional image - S3C2

From the defects identified above, cracks are seen as high priority but low severity defects as they lead to defect propagation, inhomogeneous current distribution, radical attack, increased resistance and pinhole growth. Delamination are low priority but high severity defects as they lead to increased probability of water flooding, partitioning of CL and membrane across micro-cracks and pinhole areas

and increased activation loss. Coating irregularities in the CL resulting in non-uniform layers are both high priority and high severity defects as they lead to improper catalyst transfer and adhesion onto the membrane, increased surface resistance, increased probability of water flooding and can lead to other defects due to breaking of the CL.

6.8.2. Surface Imaging

The surface imaging allowed us to identify defects as described by *Prasad (2019)* in *Figure 10*, which include microcracks on the surface of the CL, catalyst clusters / agglomerates, ionomer agglomerates, embedded debris, fibres and scratches on the CLs as seen in Figure 90, Figure 91 and Figure 92.

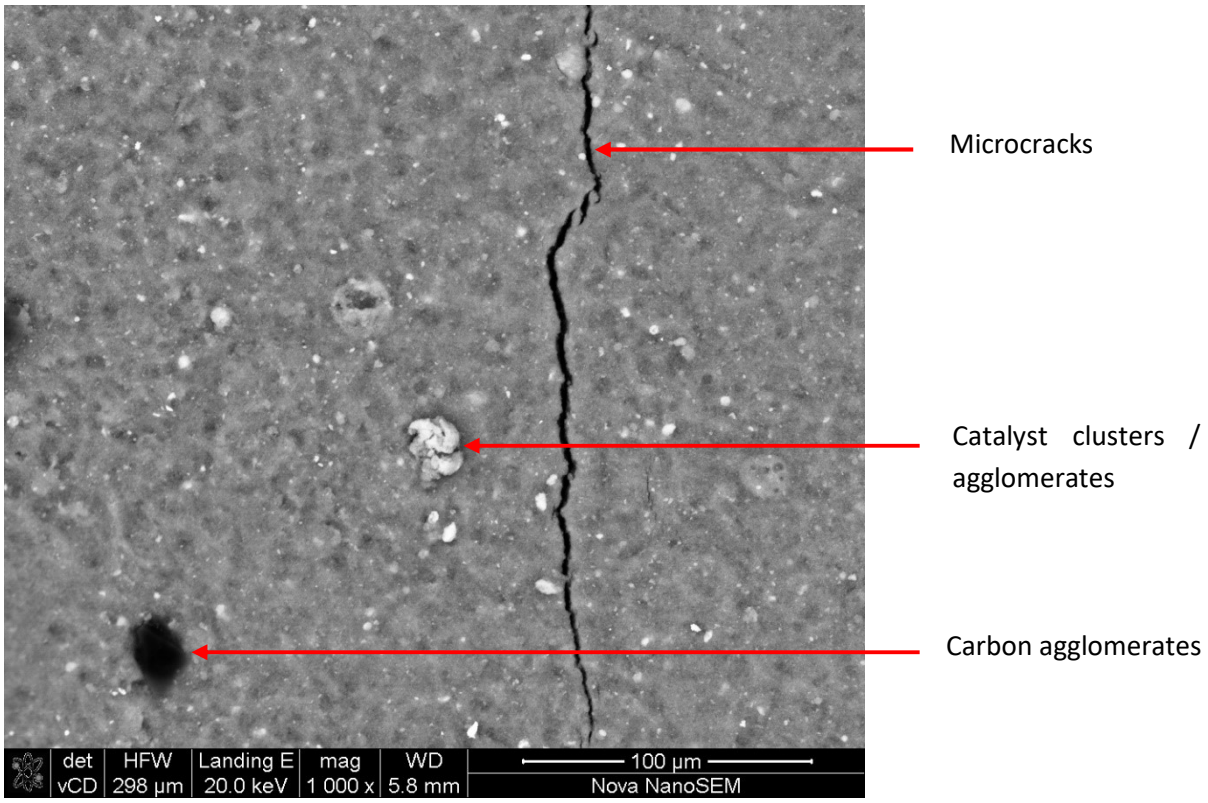

Figure 90: SEM Surface Image - S1C1

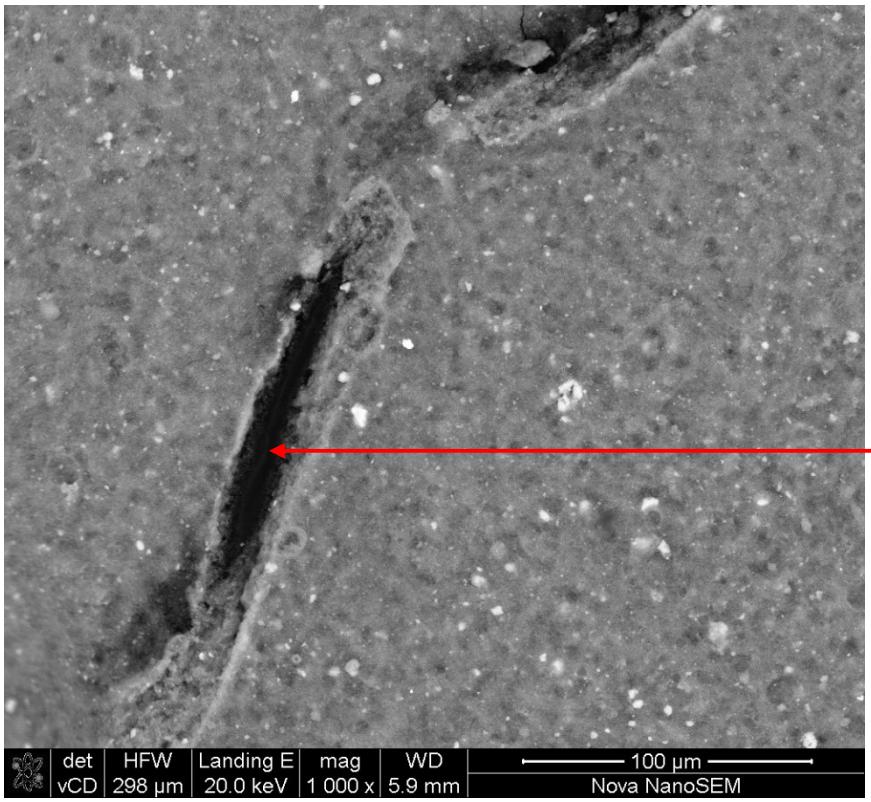

Figure 91: SEM Surface Image - S1C2

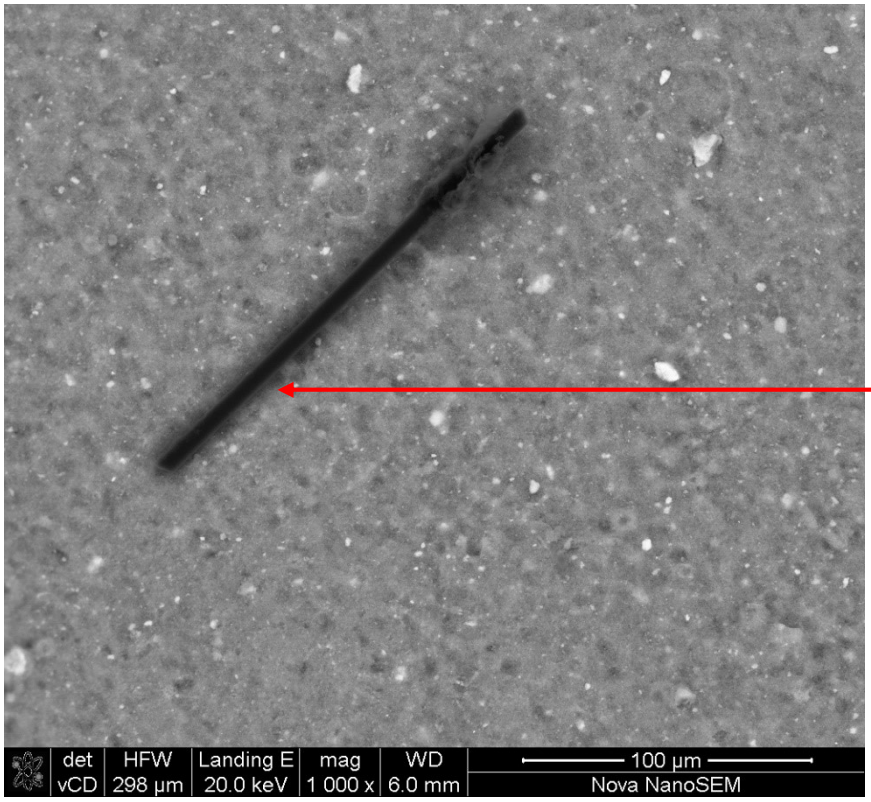

Figure 92: SEM Surface Image - S1C2

6.9. Summary of Results & Discussion

The results from the thickness and gravimetric analysis in section 5.1 and 5.2 showed that the two measures were in agreement with each other and yielded values that were on par with the experimental targets and commercial standards. A linear relationship was also demonstrated in Figure 71, showing the link between thickness and gravimetric loading whereby the thickness increases as the gravimetric loading increases or vice versa. However, even though the relationship is linear the equation which describes the relationship between the two can vary as both tests are sensitive to changes in relative humidity. Changes in the relative humidity cause the membrane and the ionomer in the CL to either absorb moisture faster or slower and to potentially swell. The former will result in false gravimetric loadings and the latter will result in false thickness measurements. Within the scope of this study, a thin membrane was used to negate the effect of relative humidity as much as possible and it was observed that the thickness test was more reliable than the gravimetric test when the relative humidity did fluctuate. If the relative humidity is well controlled, one of the two quality control methods could be omitted during manufacturing to decrease manufacturing time. To overcome the downfall associated with relative humidity for both these test methods, a newer technology, XRF spectrometry, was investigated which determines the PGM loading and is independent of changes in the relative humidity. The PGM loading can then be used to calculate the approximate thickness of the electrode layers if needed and is less labour intensive and time consuming. It was discovered that the XRF needs to be specifically programmed for each matrix that it is to be used on – where the matrix includes the substrate thickness, type of substrate, type of catalyst in the ink, ionomer content and sample orientation (cathode or anode facing XRF eye). It is assumed that the matrix expands to other parameter changes as well, such as type of ionomer, ink solids content and presence of backers or covers film. However, these parameters were not tested within this study due to time and resource constraints.

To assess the aesthetic and physical quality of the CLs produced, visual and optical microscopy inspection were done. Visual inspection involves human observation of the layer under light, therefore, methods were developed in this study to improve the test procedure and omit human error by digitising the test procedure. The results yielded from the visual and optical microscopy inspection were compared and were found to be almost identical, with the exception of the shape of pinholes being more defined and debris or surface defects being easier to identify with the microscope. However, for the purpose of commercial manufacturing to identify light translucency above 10%, it would be less labour intensive and time consuming to use the automated visual inspection method developed. Using optical microscopy inspection would be better suited to laboratory scale production, product development and root cause analysis. The downfall of either method arises when coating the anode layer (in this study) or when coating the second electrode (in general) due to the masking effect of first layer on the second, which prevents inconsistencies in the second layer being identified. The other downfall of either method is the inability to determine if a defect is a light spot or if it is a pinhole through the MEA. This is where IRT comes in as it was successful in identify pinholes.

Assessing the performance of an MEA can only be done by means of single cell performance characterisation, which is a destructive measure from which the MEA cannot be recovered. Within the scope of this study, single cell performance characterisation was used to test whether the methods developed for visual inspection, XRF analysis and/or IR thermography had a negative or destructive effect on the MEAs tested – the results proved that there was no effect. A non-destructive method to

obtain the data generated from single cell performance characterisation does not currently exist and this quality method would still be necessary in MEA manufacturing. However, by implementing XRF analysis, visual inspection and IRT into a manufacturing line, the sampling rate for MEAs going through single cell performance characterisation can be decreased significantly.

SEM is another destructive measure which was used within the scope of this study to observe whether the methods developed for visual inspection, XRF analysis and/or IR thermography had a negative or destructive effect on the MEAs tested. The results proved that there was no effect, however, a strange phenomenon was observed, whereby the CLs had detached from the membrane for all the MEAs irrespective of the quality tests conducted on them. This could have been due swelling and shrinkage of the membrane during the SEM sample prep or could have been due to incompatibility of the ionomer and membrane used in the study. SEM analysis would not typically be implemented as a manufacturing quality control unless being used for product development or root cause analysis.

CHAPTER VII: CONCLUSIONS AND FUTURE WORK

This chapter includes a summary of the main conclusions of this study and contributions to research for PEMFC literature The chapter further discusses the possible directions for future research associated with the work done in this thesis.

The automated visual inspection technique was successful in capturing a human process in a digital form and yielded comparative results to optical microscopy inspection. The study was successful in developing a method for the use of XRF to determine PGM loadings and in investigating key parameters associated with its calibration procedures and sensitivity. The value of XRF over gravimetric analysis was shown and the XRF was successfully incorporated into a simulated high-volume line. A method for the use of IRT for defect detection was also successfully developed. All three of these techniques were proven to be key control measures for the manufacturing of MEAs and were shown to be advantageous in comparison to the current methods but cannot completely replace the current methods.

All three techniques were successfully developed for local use in laboratory and small-medium scale manufacturing. The automated visual inspection technique proved to be a key quality control technique and further work into its next generation and incorporation into a high-volume manufacturing line is needed as this could not be investigated due to time and budget constraints. The study was successful in developing a method for the use of XRF to determine PGM loadings and in investigating key parameters associated with its calibration procedures. The value of XRF over gravimetric analysis was shown and the XRF was successfully incorporated into a simulated high-volume line, however, further work is needed for its next generation in a high-volume line. A method for the use of IRT for defect detection was also successfully developed and an attempt to create a defect catalogue was started, however, cataloguing the appearance of defects in IRT still requires more work and due to the time and budget constraints of this project, only a select amount of defects could be catalogued. Furthermore, the constraints of the project did not allow for IRT to be implemented on a high-volume line as this would require a more advanced rig build that mitigates the safety concerns associated with having H_2 exposed to a high-volume manufacturing line.

REFERENCES

Aieta, N., Das, P., Perdue, A., Bender, G., Herring, A., Weber, A., & Ulsh, M. (2012). Applying infrared thermography as a quality-control tool for the rapid detection of polymer-electrolyte-membrane-fuel-cell catalyst-layer-thickness variations. *Journal of Power Sources 211*, 4-11.

Barbir, F. (2005). *PEM Fuel Cells* . San Diego: Elseview Academic Press .

Baricci, A., Bisello , A., Serov, A., Odgaard, M., Atanassov , P., & Casalegno, A. (2019). Analysis of the effect of catalyst layer thickness on the performance and durability of platinum group metal-free catalysts for polymer electrolyte membrane fuel cells. *Sustainable Enegry & Fuels , 3*(12), 3375-3386.

Bender, G., Felt, W., & Ulsh, M. (2014). Detecting and localizing failure points in proton exchange membrane fuel cells using IR thermography. *Journal of Power Sources 253*, 224-229.

Birol, F. (2019). *The Future of Hydrogen* . IEA.

Bowers, C. (2019). Matrix Effect Corrections in X-ray Fluorescence Spectrometry. *Journal of Chemical Education* , 2597-2599.

Brouwer, P. (2003). *Theory of XRF* . Netherlands: PANalytical BV.

Bruijn, A., & Janssen, G. (2012). PEM Fuel Cell Materials: Costs, Performance and Durability. In *Encyclopedia of Sustainability Science and Technology* (pp. 7694-7730). New York : Springer.

Cambridge in Colour . (n.d.). *CAMERAS VS. THE HUMAN EYE*. Retrieved from Cambridge in Colour : https://www.cambridgeincolour.com/tutorials/cameras-vs-human-eye.htm

Cheney , B. (2007). *Introduction to scanning electron microscopy.*

Chourashiya, M., Sharma, R., & Andersen, S. (2018). Accurate determination of catalyst loading on classy carbon disk and its impact on thin film rotating disk electrode for oxygen reduction reaction. *Analytical Chemistry* , 14181-14187.

Cigolotti , V., Genovese, M., & Fragiacomo, P. (2021). Comprehensive Review on Fuel Cell Technology for Stationary Applications as Sustainable and Efficient Poly-Generation Energy Systems. *Energies, 14*, 4963.

Ebrahimi, M., Kujawski, W., Fatyeyeva, K., & Kujawa, J. (2021). A Review on Ionic Liquids-Based Membranes for Middle and High Temperature Polymer Electrolyte Membrane Fuel Cells (PEM FCs). *Internation Journal of Molecular Science, 22*(11). doi:https://doi.org/10.3390/ijms22115430

Erickson, S. (2007). Updates in nozzle-less ultrasonic coating technology for fuel cell manufacturing . *Fuel Cells* , 24-29.

FLIR. (2021). *FLIR ONE PRO*. Retrieved from TELEDYNE FLIR: https://www.flir.eu/products/flir-one-pro/

Haynes, W. (2011). *CRC Handbook of Chemistry and Physics* . CRC Press.

Holbrook, J., Arthurs, D., & Cassidy, E. (2010). Understanding the Vancouver Hydrogen and Fuel Cells Cluster: A Case Study of Public Laboratories and Private Research. *European Planning Studies* , 317-328.

Hossen, M., Artyushkova, K., Atanassov, P., & Serov, A. (2018). Synthesis and characterization of high performing Fe-N-C catalyst for oxygen reduction reaction (ORR) in Alkaline Exchange Membrane Fuel Cells. *Journal of Power Sources*, 214-221.

Kalamaras, C., & Efstathiou, A. (2013). Hydrogen Production Technologies: Current State and Future Developments. *Hindawi* . doi:https://doi.org/10.1155/2013/690627

Laabidi, S. (2015). *Test methods for the quality assurance during the production of PEM fuel cells.* Munich: GRIN Verlag. Retrieved from https://www.grin.com/document/299917

Labi , T. (2019). *IRIDIUM OXIDE SUPPORTED ON GRAPHITIZED CARBON FOR USE AS REVERSAL TOLERANT ANODES IN PEM FUEL CELLS.* Cape Town: University of Cape Town.

Lynch, P. (2005, February 01). *The Hydrogen Economy And Fuel Cells*. Retrieved from Alt Energy Mag: https://www.altenergymag.com/article/2005/02/the-hydrogen-economy-and-fuel-cells/158/#:~:text=will%20be%20everywhere-,Fuel%20cells%20will%20be%20one%20of%20the%20key%20components%20in,power%20when%20it%20is%20needed.

Mawungwe, N. (Submitted in February 2023). *Fabrication of Catalyst Coated Membranes by Ultrasonic Spray for Proton Exchange Membrane Water Electrolysers.* Cape Town: University of Cape Town.

Mettler Toledo. (n.d.). *Balance XS104*. Retrieved from Mettler Toledo : https://www.mt.com/es/en/home/phased_out_products/Laboratory_Weighing_Solutions/Analytical/Excellence/XS_Analytical_Balance/XS104.html

Migliardini, F., & Corbo, P. (2013). CV and EIS Study of Hydrogen Fuel Cell Durability in Automotive Applications. *Internation Journal of Electrochemical Science* , 11033-11047.

Mitchell, N. (n.d.). *What Camera Lens is Closest to the Human Eye?* Retrieved from Photodoto: https://www.photodoto.com/camera-lens-closest-to-human-eye/#:~:text=The%2050%20mm%20lens%20is,focal%20length%20of%20the%20eye

Mitutoyo. (2022). *Indicators* . Retrieved from RS Components : https://docs.rs-online.com/3012/0900766b81075068.pdf

Mitzel, J., Gulzow, E., Kabza, A., Hunger, J., Araya, S., Piela, P., . . . Tsotridis, G. (2016). Identification of Critical Parameters for PEMFC Stack Performace Characterisation and Control Strategies for Reliable and Comparable Stack Benchmarking. *Internation Journal of Hydrogen and Energy* , 21415-21426.

Moskovitz, K. (2013). *Development of a spray coating method for the development of a spray coating method for the catalyst coated membranes.* Cape Town: University of Cape Town.

NanoScience Instruments . (n.d.). *Scanning Electron Microscopy*. Retrieved from Nano Science : https://www.nanoscience.com/techniques/scanning-electron-microscopy/

Nicita, A., Maggio, G., Andaloro, A., & Squadrito, G. (2020). Green hydrogen as feedstock: Financial analysis of a photovoltaic-powered electrolysis plant. *Internation Journal of Hydrogen Energy* , 11395-11408.

Niemantsverdriet, J. (n.d.). *Spectroscopy in catalysis: An Introduction.* . John Wiley & Sons.

Nixon, W. (1971). The general principles of scanning electron microscopy. *Biological Sciences, 261*(837), 45-50.

Nondudule, Z. (2020). *Stratification of Cathode Catalyst Layers for Low-temperature Proton Exchange Membrane Fuel Cells (PEMFC).* Cape Town : Cape Peninsula University of Technology .

Olympus. (2018, March). Vanta Family X-Ray Fluorescence Analyzer User Manual. USA.

Olympus Industrial Solutions. (2021). *Handheld XRF Analysers*. Retrieved from Olympus: https://www.olympus-ims.com/en/xrf-xrd/xrf-handheld/?gclid=Cj0KCQjw--GFBhDeARIsACH_kdY_ihT8c4tH-kEwa3IAnEUvA4RCcQbqBH5OEl1-9eptdJeJR2M6X8AaAtTQEALw_wcB

Ozden, A., Alaefour, I., Shahgaldi, S., Li, X., Colpan, C., & Hamadullahpur, F. (2018). Chapter 2.28 - Gas Diffusion Layers for PEM Fuel Cells: Ex- and In-Situ Characterization. In I. Dincer , C. Colpan, & O. Kizilkan, *Exergetic, Energetic and Environmental Dimensions* (pp. 695-727). Elsevier.

Pak , C., You , D., Choi, K., & Chang, H. (2012). *Hydrogen Energy - Challenges and Perspectives .* (D. Minic , Ed.) InTech. doi:DOI: 10.5772/2824

Peter, S. (2018). Reduction of CO2 to Chemicals and Fuels: A Solution to Global Warming and Energy Crisis. *ACS Energy Letters*, 1557-1561. doi:10.1021/acsenergylett.8b00878

Phillips, A., Ulsh , M., Neyerlin, K., Porter, J., & Bender, G. (2018). Impacts of electrode coating irregularities on polymer electrolyte membrane fuel cell lifetime using quasi in-situ infrared thermography and accelerated stress testing. *International Journal of Hydrogen Energy* , 6390-6399.

Pollet , B. (2010). The use of ultrasound for the fabrication of fuel cell materials. *International Journal of Hydrogen Energy, 35*(21), 11986-12004.

Prasad, A. (2019). *Investigation and Propagation of Defects in the Membrane Electrode Assembly of Polymer Electrolyte Membrane Fuel Cells: Quality Control Analysis.* Canada: University of Waterloo.

Ritchie, H. (2020, September 18). *Sector by sector: where do global greenhouse gas emissions come from?* Retrieved from Our World in Data: https://ourworldindata.org/ghg-emissions-by-sector

SASOL. (2021, April 14). *SASOL AND TOYOTA SOUTH AFRICA MOTORS FORM GREEN HYDROGEN MOBILITY PARTNERSHIP*. Retrieved from SASOL: https://www.sasol.com/media-centre/media-releases/sasol-and-toyota-south-africa-motors-form-green-hydrogen-mobility?gclid=Cj0KCQjwktKFBhCkARIsAJeDT0h3H4QbPrZNaIZ0fqsbYc1eulxnjo6rRQvkD9mvIMhN7EVQnMRshSUaAlDpEALw_wcB&gclsrc=aw.ds

Shutter Release World . (n.d.). *What Camera Lens is Closest to the Human Eye*. Retrieved from Shutter Release: https://www.shutterreleaseworld.com/what-camera-lens-is-closest-to-the-human-eye/

Song, C., & Park, J. (2019). Effect of Dispersion Solvents in Catalyst Inks on the Performance and Durability of Catalyst Layers in Proton Exchange Membrane Fuel Cells. *Energies Journal* , 549.

ThermoFisher Scientific. (2020, January 28). *What is XRF (X-ray Fluorescence) and How Does it Work?* Retrieved from ThermoFisher: https://www.thermofisher.com/blog/ask-a-scientist/what-is-xrf-x-ray-fluorescence-and-how-does-it-work/

U.S. Department of Energy . (2011, February). *Energy Efficiency & Renewable Energy.* Retrieved from Energy: https://upload.wikimedia.org/wikipedia/commons/3/36/EERE_Fuel_Cell_Comparison_Chart.pdf

Ul-Hamid, A. (2018). *A beginners' guide to scanning electron microscopy.* Springer.

Ulsh, M. (n.d.). *Fuel Cell Manufacturing Research and Development*. Retrieved from NREL: https://www.nrel.gov/hydrogen/manufacturing.html

Ultrasonic Systems Inc. . (n.d.). *USI – PRISM Series Datasheet (122217).* Retrieved from Ultraspray: http://www.ultraspray.com/uniform-precise-coatings/library/literature/

US Department of Energy. (n.d.). *Parts of a Fuel Cell*. Retrieved from Energy.gov: https://www.energy.gov/eere/fuelcells/parts-fuel-cell

Vernon-Parry, K.-V. (2000). Scanning electron microscopy: An introduction. *13*(4), 40-44.

Wang , Y., Chen, K., Mishler, J., Cho, S., & Adroher, X. (2011). A review of polymer electrolyte membrane fuel cells: Technology, applications, and needs on fundamental research. *Applied Energy, 88*(4), 981-1007. doi:http://dx.doi.org/10.1016/j.apenergy.2010.09.030

Wang, H., Yuan, X., & Li, H. (2012). *PEM FUEL CELL DIAGNOSTIC TOOLS.* New York : CRC Press.

Weber , A. (2008). Gas-Crossover and Membrane-Pinhole Effects in Polymer-Electrolyte Fuel Cells. *Journal of The Electrochemical Society* .

Wu, J., Yuan, X., Wang , H., Blanco, M., Martin, J., & Zhang , J. (2008). Diagnostic tools in PEM fuel cell research: Part I Electrochemical techniques. *Internation Journal of Hydrogen Energy* , 1735-1746.

Wulf, C., Zapp, P., & Schreiber, A. (2020). Review of Power-to-X Demonstration Projects in Europe. *Frontiers in Energy Research* . doi:https://doi.org/10.3389/fenrg.2020.00191

Yuan, X., Coynel, C., Shaigan, N., Fisher, D., Zhao, N., Zamel, N., . . . Groos, U. (2021). A review of functions, attributes, properties and measurements for the quality control of proton exchange membrane fuel cell components. *Journal of Power Sources*.

Yuan, X., Sun, J., & Zhang, J. (2007). AC impedance technique in PEM fuel cell diagnosis—A review. *International Journal of Hydrogen Energy, 32*, 4365-4380.

Zhu , W., Payne, R., & Tatarchuk , B. (2007). PEM stack test and analysis in a power system at operational load via ac impedance. *Journal of Power Sources* , 211-217.

APPENDIX A: Thickness Analysis

Table 22: Thickness Analysis Data for Test MEAs (Error in the measurements is ±1 µm)

Sample set	Sample	Initial Thickness (um)	Final Thickness (um)	Net Thickness (um)	Initial Thickness (um)	Final Thickness (um)	Net Thickness (um)
1	1	15,0	43,7	28,7	43,7	64,0	20,3
	2	15,0	43,7	28,7	43,7	65,0	21,3
	3	15,0	42,7	27,7	42,7	63,0	20,3
2	1	15,0	42,3	27,3	42,3	60,0	17,7
	2	15,0	41,0	26,0	41,0	60,0	19,0
	3	15,0	41,7	26,7	41,7	61,0	19,3
3	1	15,0	41,7	26,7	41,7	59,0	17,3
	2	15,0	41,0	26,0	41,0	61,0	20,0
	3	15,0	43,7	28,7	43,7	61,0	17,3
4	1	15,0	43,7	28,7	43,7	63,0	19,3
	2	15,0	42,0	27,0	42,0	60,0	18,0
	3	15,0	45,0	30,0	45,0	61,0	16,0
4 - repeat	4	15,0	41,3	26,3	41,3	57,0	15,7
	5	15,0	39,7	24,7	39,7	57,0	17,3
	6	15,0	42,3	27,3	42,3	58,0	15,7
5	1	15,0	40,0	25,0	40,0	62,0	22,0
	2	15,0	42,3	27,3	42,3	63,0	20,7
	3	15,0	40,0	25,0	40,0	60,0	20,0
6	1	15,0	44,0	29,0	44,0	62,0	18,0
	2	15,0	43,3	28,3	43,3	58,0	14,7
	3	15,0	43,0	28,0	43,0	58,0	15,0
7	1	15,0	44,3	29,3	44,3	65,0	20,7
	2	15,0	40,7	25,7	40,7	64,0	23,3
	3	15,0	40,7	25,7	40,7	60,0	19,3
Average		15	15,0	42,2	27,2	42,2	60,9
Standard deviation		0	0,0	1,5	1,5	1,5	2,3

APPENDIX B: Gravimetric Analysis

Table 23: Gravimetric Analysis Data for test MEAs(Error in the measurements is ±0.1 mg for weights and 0.01 mg/cm² for loadings)

Sample set	Sample	Initial Weight (g)	Final Weight (g)	Net Weight (g)	Loading (mg Pt /cm2)	Initial Weight (g)	Final Weight (g)	Net Weight (g)	Loading (mg Pt /cm2)
1	1	0,1436	0,1774	0,0338	0,4097	0,1774	0,1938	0,0164	0,1988
	2	0,1451	0,1785	0,0334	0,4048	0,1785	0,1956	0,0171	0,2073
	3	0,1439	0,1775	0,0336	0,4072	0,1775	0,1938	0,0163	0,1976
2	1	0,1443	0,1775	0,0332	0,4024	0,1775	0,1944	0,0169	0,2048
	2	0,1432	0,1764	0,0332	0,4024	0,1764	0,1931	0,0167	0,2024
	3	0,1416	0,1749	0,0333	0,4036	0,1749	0,1920	0,0171	0,2073
3	1	0,1481	0,1817	0,0336	0,4072	0,1817	0,1986	0,0169	0,2048
	2	0,1447	0,1780	0,0333	0,4036	0,1780	0,1948	0,0168	0,2036
	3	0,1434	0,1769	0,0335	0,4060	0,1769	0,1936	0,0167	0,2024
4	1	0,1425	0,1756	0,0331	0,4012	0,1756	0,1923	0,0167	0,2024
	2	0,1425	0,1762	0,0337	0,4084	0,1762	0,1934	0,0172	0,2085
	3	0,1459	0,1806	0,0347	0,4206	0,1806	0,1978	0,0172	0,2085
4 - repeat	4	0,146	0,179	0,0330	0,4000	0,1834	0,1999	0,0165	0,2000
	5	0,1444	0,178	0,0336	0,4072	0,1824	0,1986	0,0162	0,1963
	6	0,1462	0,1792	0,0330	0,4000	0,183	0,1989	0,0159	0,1927
5	1	0,1448	0,1788	0,0340	0,4121	0,1788	0,1960	0,0172	0,2085
	2	0,1447	0,1780	0,0333	0,4036	0,1780	0,1950	0,0170	0,2060
	3	0,1425	0,176	0,0335	0,4060	0,176	0,1925	0,0165	0,2000
6	1	0,1442	0,1791	0,0349	0,4230	0,1791	0,196	0,0169	0,2048
	2	0,1428	0,1778	0,0350	0,4242	0,1778	0,1949	0,0171	0,2073
	3	0,1453	0,1796	0,0343	0,4157	0,1796	0,1962	0,0166	0,2012
7	1	0,1473	0,1816	0,0343	0,4157	0,1816	0,1983	0,0167	0,2024
	2	0,1429	0,1772	0,0343	0,4157	0,1772	0,1942	0,0170	0,2060
	3	0,1415	0,1746	0,0331	0,4012	0,1746	0,1916	0,0170	0,2060
Average		15	0,1442	0,1779	0,0337	0,4084	0,1784	0,1952	0,0168
Standard deviation		0	0,0017	0,0018	0,0006	0,0071	0,0025	0,0024	0,0003

APPENDIX C: Visual Inspection

Table 24: Visual Inspection Images and Light Transparency for Cathode Electrode of Test MEAs

Sample Set	Description	1	2	3
1	Light Transparency (%) per sample	0,01	0,005	0,012
	Average Light Transparency (%) for sample set	0,009		
2	Light Transparency (%) per sample	0,024	0,003	0,001
	Average Light Transparency (%) for sample set	0,01		
3	Light Transparency (%) per sample	0,004	0,006	0,003
	Average Light Transparency (%) for sample set	0,004		
4	Light Transparency (%) per sample	0,003	0,003	0,012
	Average Light Transparency (%) for sample set	0,006		
4-repeat	Light Transparency (%) per sample	0,001	0	0,001
	Average Light Transparency (%) for sample set	0,001		
5	Light Transparency (%) per sample	0,004	0,002	0,004
	Average Light Transparency (%) for sample set	0,003		
6	Light Transparency (%) per sample	0,002	0,003	0,006
	Average Light Transparency (%) for sample set	0,004		
7	Light Transparency (%) per sample	0,011	0,008	0,011
	Average Light Transparency (%) for sample set	0,01		

Table 25: Visual Inspection Images and Light Transparency for Anode Electrode of Test MEAs

Sample Set	Description	1	2	3
1	Light Transparency (%) per sample	0,000	0,000	0,001
	Average Light Transparency (%) for sample set	0,000		
2	Light Transparency (%) per sample	0,001	0,000	0,000
	Average Light Transparency (%) for sample set	0,001		
3	Light Transparency (%) per sample	0,000	0,001	0,000
	Average Light Transparency (%) for sample set	0,000		
4	Light Transparency (%) per sample	0,000	0,000	0,000
	Average Light Transparency (%) for sample set	0,000		
4-repeat	Light Transparency (%) per sample	0,002	0,002	0,002
	Average Light Transparency (%) for sample set	0,002		
5	Light Transparency (%) per sample	0,002	0,002	0,002
	Average Light Transparency (%) for sample set	0,002		
6	Light Transparency (%) per sample	0,001	0,001	0,001
	Average Light Transparency (%) for sample set	0,001		
7	Light Transparency (%) per sample	0,001	0,001	0,001
	Average Light Transparency (%) for sample set	0,001		

APPENDIX D: Optical microscopy inspection

Table 26: Optical microscopy inspection Images and Light Transparency for Cathode Electrode of Test MEAs

Sample Set	Description	1	2	3
1	Light Transparency (%) per sample	0,22	1,49	0,00
	Average Light Transparency (%) for sample set		0,57	
2	Light Transparency (%) per sample	2,96	0,78	0,09
	Average Light Transparency (%) for sample set		1,28	
3	Light Transparency (%) per sample	0,18	0,37	0,51
	Average Light Transparency (%) for sample set		0,35	
4	Light Transparency (%) per sample	2,08	1,21	0,00
	Average Light Transparency (%) for sample set		1,10	
4-repeat	Light Transparency (%) per sample	0,16	0,00	0,00
	Average Light Transparency (%) for sample set		0,16	
5	Light Transparency (%) per sample	0,00	0,32	0,26
	Average Light Transparency (%) for sample set		0,19	
6	Light Transparency (%) per sample	0,00	0,80	0,44
	Average Light Transparency (%) for sample set		0,41	
7	Light Transparency (%) per sample	0,65	1,23	0,58
	Average Light Transparency (%) for sample set		0,82	

APPENDIX E: XRF Spectroscopy

Table 27: Data for Final Calibration Curve in Figure 56 (Sample 1)

Part #	1	2	3	4	5	6	7	8	9	10	11	12
RH	52,5											
Anode CL												
Net Th (um)	1,00	9,33	0,67	3,33	2,33	5,33	-0,67	4,00	6,00	3,00	2,33	1,00
Compounded Th (um)	1,00	10,33	11,00	14,33	16,67	22,00	21,33	25,33	31,33	34,33	36,67	37,67
PGM Loading (mg_{Pt}/cm^2)	0,06	0,07	0,07	0,05	0,08	0,06	0,03	0,07	0,07	0,08	0,05	0,09
Compounded PGM Loading (mg_{Pt}/cm^2)	0,06	0,13	0,20	0,25	0,34	0,39	0,42	0,50	0,57	0,64	0,70	0,79
XRF Compounded PGM Loading (%)	10,05	11,02	11,30	12,12	12,88	13,51	14,25	14,90	15,34	15,74	16,28	17,85
Cathode CL												
Net Th (um)	7,67	3,00	7,33	4,33	2,33	2,67	3,00	3,67	2,67	1,67	4,00	4,33
Compounded Th (um)	7,67	10,67	18,00	22,33	24,67	27,33	30,33	34,00	36,67	38,33	42,33	46,67
PGM Loading (mg_{Pt}/cm^2)	0,07	0,08	0,07	0,06	0,05	0,07	0,09	0,05	0,08	0,04	0,09	0,05
Compounded PGM Loading (mg_{Pt}/cm^2)	0,07	0,15	0,22	0,28	0,33	0,40	0,49	0,55	0,62	0,66	0,76	0,81
XRF Compounded PGM Loading (%)	1,07	2,07	2,90	3,62	4,35	5,12	5,97	6,67	7,58	7,97	8,51	9,43

Table 28: Data for Final Calibration Curve in Figure 56 (Sample 2)

Part #	1	2	3	4	5	6	7	8	9	10	11	12
RH	52,5											
Anode CL												
Net Th (um)	3,33	7,67	6,33	2,33	1,00	2,00	7,00	4,33	0,00	-0,67	6,00	1,67
Compounded Th (um)	3,33	11,00	17,33	19,67	20,67	22,67	29,67	34,00	34,00	33,33	39,33	41,00
PGM Loading (mg_{Pt}/cm^2)	0,06	0,08	0,05	0,07	0,08	0,06	0,05	0,06	0,05	0,08	0,05	0,08
Compounded PGM Loading (mg_{Pt}/cm^2)	0,06	0,14	0,20	0,26	0,34	0,40	0,45	0,52	0,57	0,65	0,70	0,78
XRF Compounded PGM Loading (%)	10,54	11,31	11,96	12,24	13,25	13,58	14,64	14,94	15,77	16,65	17,16	18,39
Cathode CL												
Net Th (um)	6,67	5,00	4,67	1,67	1,67	3,67	1,67	5,00	6,00	0,33	4,67	2,00
Compounded Th (um)	6,67	11,67	16,33	18,00	19,67	23,33	25,00	30,00	36,00	36,33	41,00	43,00
PGM Loading (mg_{Pt}/cm^2)	0,06	0,07	0,06	0,07	0,07	0,06	0,07	0,31	-0,18	0,06	0,08	0,08
Compounded PGM Loading (mg_{Pt}/cm^2)	0,06	0,13	0,19	0,26	0,33	0,38	0,46	0,77	0,58	0,64	0,73	0,81
XRF Compounded PGM Loading (%)	1,10	2,01	2,94	3,77	4,52	5,46	6,31	6,62	7,30	8,01	8,67	10,01

Table 29: Data for Final Calibration Curve in Figure 56 (Sample 3)

Part #	1	2	3	4	5	6	7	8	9	10	11	12
RH	52,5											
Anode CL												
Net Th (um)	2,33	12,67	3,33	3,67	5,00	4,33	6,33	-1,67	4,67	8,67	3,33	0,67
Compounded Th (um)	2,33	15,00	18,33	22,00	27,00	31,33	37,67	36,00	40,67	49,33	52,67	53,33
PGM Loading (mg_{Pt}/cm^2)	0,07	0,07	0,07	0,07	0,06	0,06	0,07	0,07	0,06	0,06	0,07	0,10
Compounded PGM Loading (mg_{Pt}/cm^2)	0,07	0,13	0,20	0,27	0,33	0,39	0,46	0,53	0,59	0,65	0,72	0,82
XRF Compounded PGM Loading (%)	9,96	10,66	11,45	12,14	12,79	13,74	14,46	15,28	15,96	16,75	17,22	17,54
Cathode CL												
Net Th (um)	3,67	3,67	2,00	5,00	4,00	0,67	5,67	2,00	4,33	2,00	9,33	2,67
Compounded Th (um)	3,67	7,33	9,33	14,33	18,33	19,00	24,67	26,67	31,00	33,00	42,33	45,00
PGM Loading (mg_{Pt}/cm^2)	0,04	0,08	0,06	0,05	0,07	0,07	0,05	0,05	0,05	0,09	0,04	0,09
Compounded PGM Loading (mg_{Pt}/cm^2)	0,04	0,12	0,18	0,24	0,31	0,38	0,43	0,48	0,53	0,62	0,66	0,76
XRF Compounded PGM Loading (%)	1,04	1,96	2,84	3,64	4,39	5,20	5,87	6,32	7,04	7,82	8,66	9,60

APPENDIX F: IRT

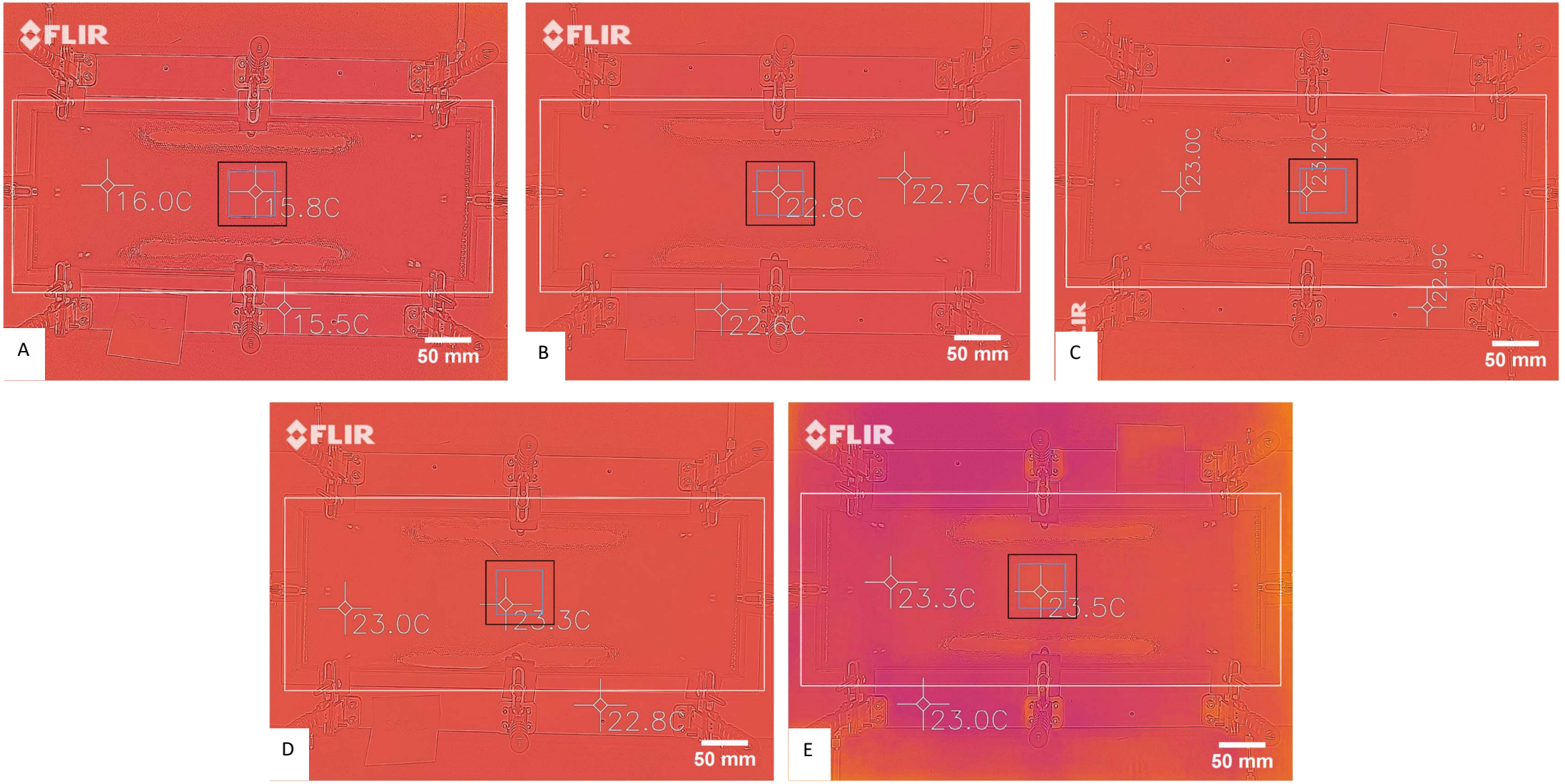

Figure 93: IRT result for A - Sample 2 of Sample Set 5, B - Sample 3 of Sample Set 5, C - Sample 1 of Sample Set 6, D - Sample 2 of Sample Set 6 and E - Sample 3 of Sample Set 6

APPENDIX G: Single Cell Performance Testing

Table 30: Test Conditions linked to internal performance data (Figure 92 below) for HySA Catalysis MEAs fabricated with HySA K40 catalyst, Avcarb MB30 GDLs, 32 um PET gaskets and a PGM loading of 0.1/0.4 mgPt/cm2 anode/cathode

Test Parameter		Units
Active Area	25.00	cm^2
Anode Bubbler Temperature	80.00	°C
Cathode Bubbler Temperature	75.00	°C
Anode Line Temperature	90.00	°C
Cathode Line Temperature	90.00	°C
Anode Back Pressure	2.00	Bar
Cathode Back Pressure	2.00	Bar
Cell Temperature	80.00	°C
Anode Stoichiometry	1.50	-
Cathode Stoichiometry	2.00	-
Anode minimum flowrate	0.15	NL/min
Cathode minimum flowrate	0.53	NL/min
Cell Fixture	Baltic	-

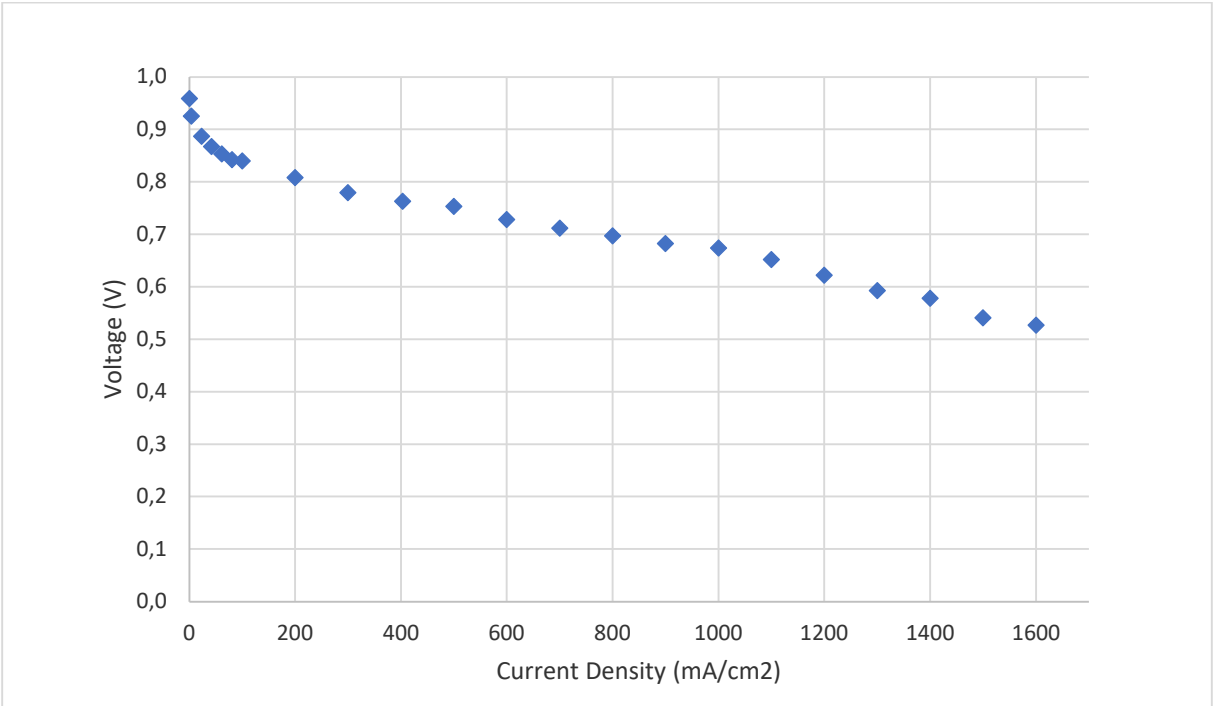

Figure 94: Performance Data Benchmark supplied by HySA Catalysis

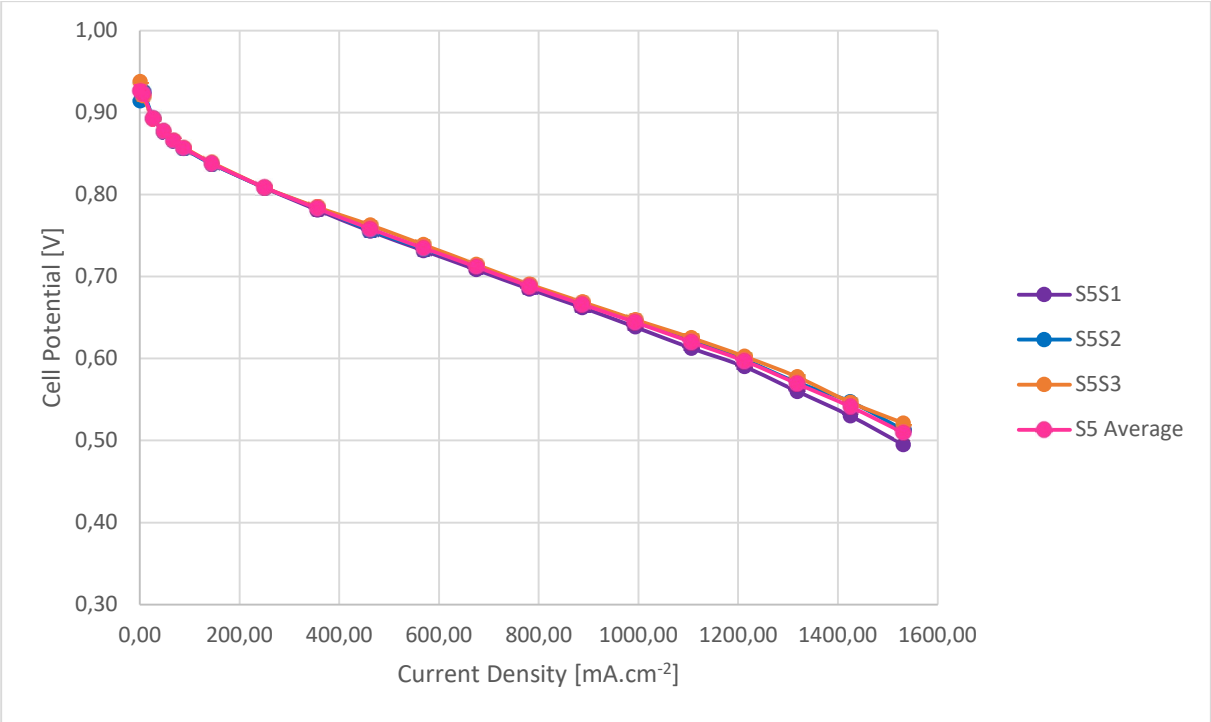

Figure 95: Polarisation Curves for the IRT Samples

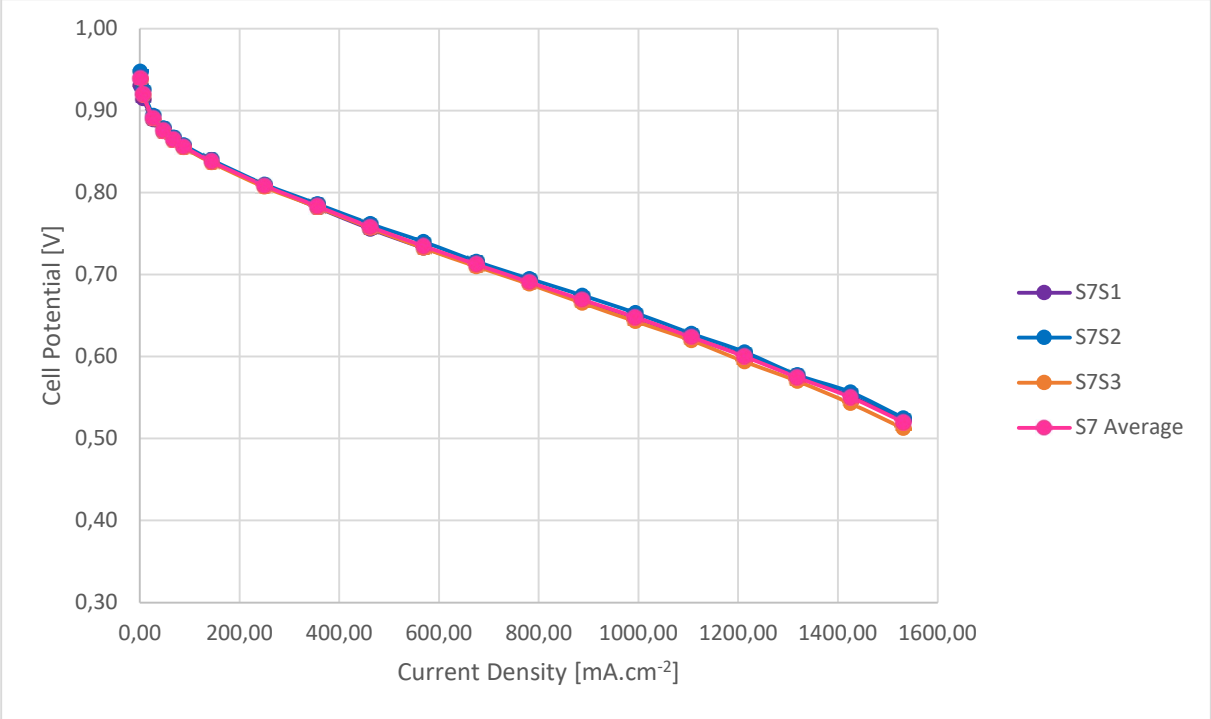

Figure 96: Polarisation Curves for the Intensive XRF Samples

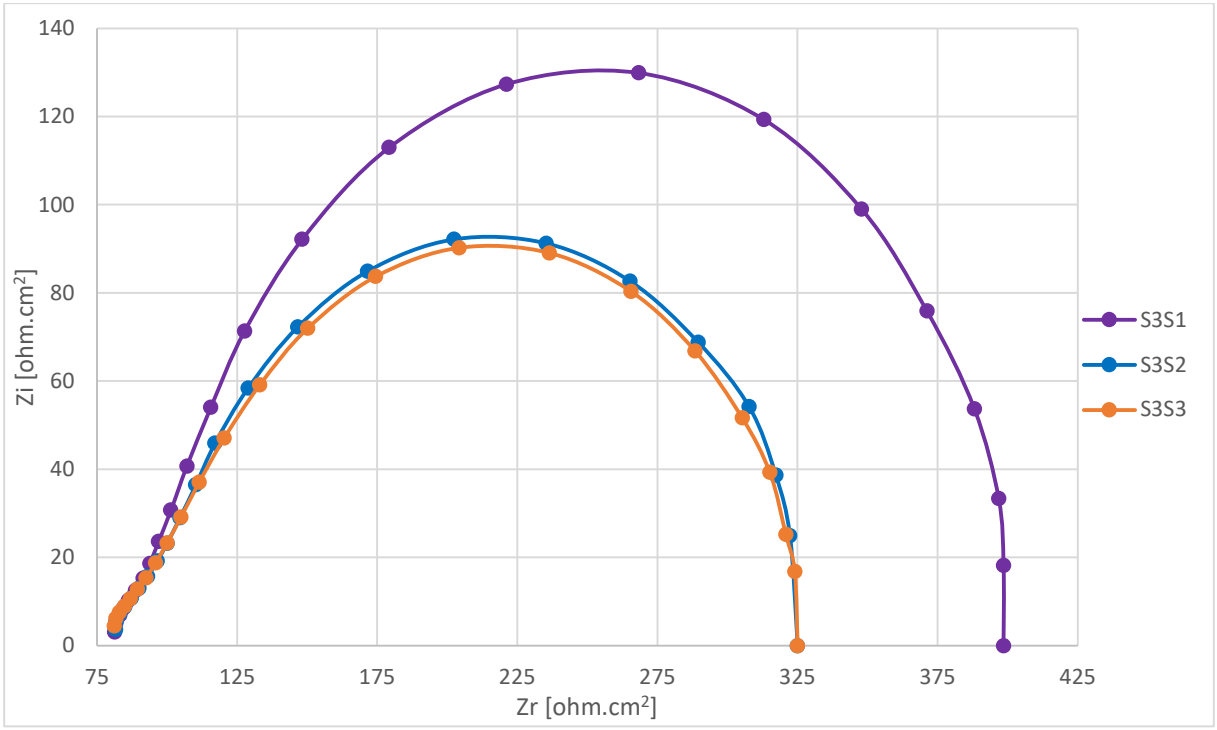

Figure 97: EIS Curve for XRF Samples

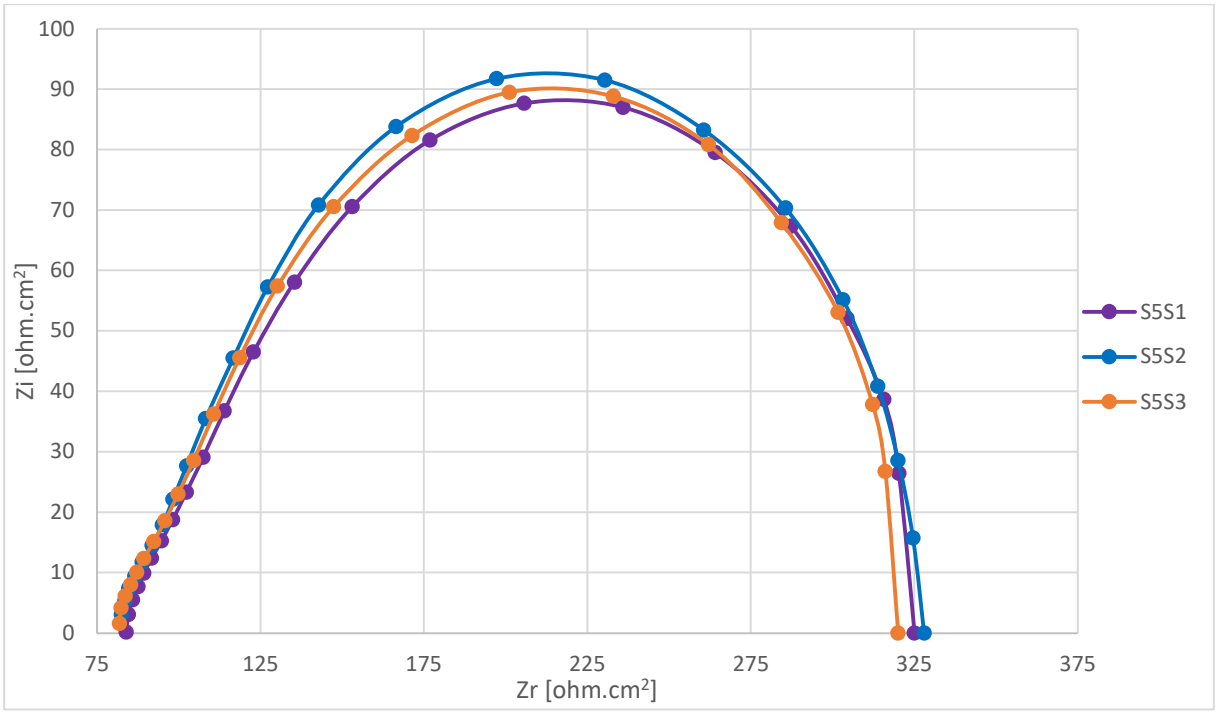

Figure 98: EIS Curve for IRT Samples

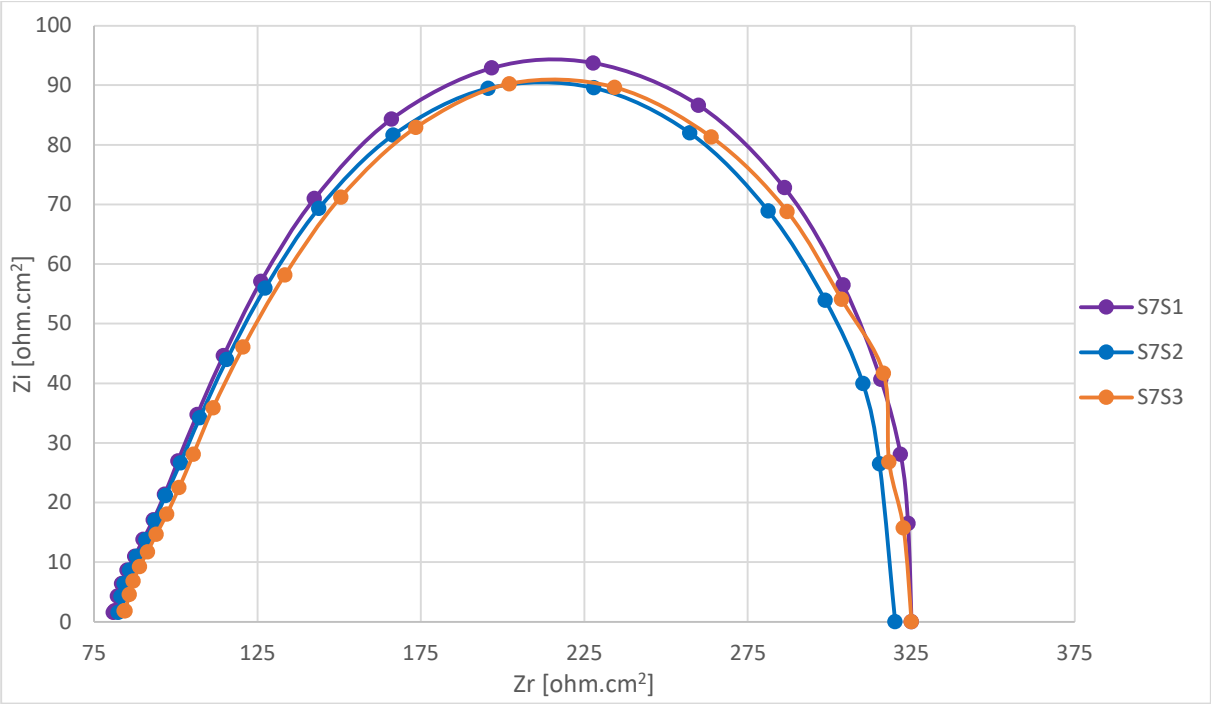

Figure 99: EIS Curve for Intensive XRF Samples

APPENDIX H: SEM

Table 31: SEM Thickness Data

Sample	Average Cathode Thickness per set (um)	Average Anode Thickness per set (um)
S1C1	14,43	5,37
S1C2	16,03	5,58
S1C3	16,59	5,33
S2C1	16,05	5,29
S2C2	14,98	5,77
S2C3	12,60	5,87
S3C1	14,68	4,29
S3C2	14,90	6,10
S3C3	14,72	5,71
S4C3	15,80	6,06
S4C4	15,14	7,30
S4C5	16,23	7,14
S4C6	15,29	6,88
S5C1	14,23	4,85
S5C2	14,29	5,03
S5C3	14,17	5,46
S6C1	14,60	5,69
S6C2	17,23	5,43
S6C3	15,98	6,24
S7C1	15,19	5,29
S7C2	16,45	4,54